EFIMOV-LIKE STATES AND CONFORMATIONAL TRANSITIONS OF DNA

By

Jaya Maji

PHYS07200804001

Institute of Physics
Bhubaneswar

A thesis submitted to the
Board of Studies in Physical Science Discipline

In partial fulfillment of the requirements
For the Degree of

DOCTOR OF PHILOSOPHY
of
HOMI BHABHA NATIONAL INSTITUTE

June 2013

Homi Bhabha National Institute

Recommendations of the Viva Voce Board

As members of the Viva Voce Board, we certify that the dissertation prepared by **Jaya Maji** entitled "Efimov-like States and Conformational Transitions of DNA" and recommend that it may be accepted as fulfilling the dissertation requirement for the Degree of Doctor of Philosophy.

\- **Date:**
Chairman : Chair of committee

\- **Date:**
Convener : Conv of Committee

\- **Date:**
Member : Member 1 of committee

\- **Date:**
Member : Member 2 of committee

Final approval and acceptance of this dissertation is contingent upon the candidate's submission of the final copies of the dissertation to HBNI.

I hereby certify that I have read this dissertation prepared under my direction and recommend that it may be accepted as fulfilling the dissertation requirement.

\- **Date:**
Guide : S. M. Bhattacharjee

DECLARATION

I, hereby declare that the investigation presented in the thesis has been carried out by me. The work is original and the work has not been submitted earlier as a whole or in part for a degree/diploma at this or any other Institution/University.

Jaya Maji

STATEMENT BY AUTHOR

This dissertation has been submitted in partial fulfillment of requirements for an advanced degree at Homi Bhabha National Institute (HBNI) and is deposited in the Library to be made available to borrowers under rules of the HBNI.

Brief quotations from this dissertation are allowable without special permission, provided that accurate acknowledgment of source is made. Requests for permission for extended quotation from or reproduction of this manuscript in whole or in part may be granted by the Competent Authority of HBNI when in his or her judgment proposed use of the material is in the interests of scholarship. In all other instances, however, permission must be obtained from the author.

Jaya Maji

ACKNOWLEDGEMENTS

First and foremost I want to express my heartfelt gratitude to him who introduced me to a different world (I believe) and happened to be my thesis advisor Prof. S. M. Bhattacharjee. I am grateful for his patience, guidance and constant support throughout my PhD. I would like to thank Prof. Flavio Seno, Prof. Antonio Trovato and P. Sadhukhan for their collaboration. I would like to thank Prof. A. M. Jayannavar, Prof. A. Khare, Prof. K. Kundu and Prof. G. Tripathy for helpful discussions and encouragement. I wish to express my heartfelt gratitude to Prof. S. G. Mishra and Prof. A. M. Srivastava. I specially would like to thank Prof. S. Mukherji and Prof. B. R. Sekhar for their help and the friendly environment. I thank Tanmoy for taking interest in proofreading of this thesis. I thank all the staff of IOP.

I convey my sincere thanks to Sarama di. My time at IOP was made enjoyable in large part due to many friends. Abhishek, Rupali, Saumia and Souvik to name a few. I am grateful for the time spent with friends and teachers with music and plays. My sojourn at IOP was also enriched by the lessons from the music teachers.

I would like to thank my teachers Prabir Banerjee and Pankaj Sarkar. I offer my regards to Sanjay da, Haimanti and my best friend Naran. I would like to thank each and everyone who belongs to “Atul Bhaban” and my in laws for their support. Finally, I would like to thank my husband Arup R. Kundu for his love, constant support and encouragement, and my parents and grandparents who respected my freedom throughout.

Contents

Synopsis

The aim of this thesis is to study the melting of a triple-stranded DNA (tsDNA) and the conformational transition of a double-stranded DNA (dsDNA) in particular from the B form to the Z form of DNA.

Certain sequences of Watson-Crick-dsDNA allow a third strand DNA to bind via Hoogsteen or reverse-Hoogsteen base paring to form tsDNA. The formation of triple helical DNA is of great interest in current era. Owing to its enhanced stability in affecting the activities such as gene expression, DNA replication and others requiring DNA opening, the triple helix fostered new hopes in therapeutic applications. The third chain's ability in recognizing the base sequences of a dsDNA, not by opening the double helix but rather by forming a triple helix would be one of the major input in developing new types of antibiotic. There have been many physical, chemical and biological studies of this triple helix forming nucleotides (TFO). It is known that not only DNA, even RNA and PNA (polypeptide nucleic acid) are capable of forming triple helices with duplex DNA.

To study the phase diagram and the phase transition of a triple helix DNA we consider a few simplified polymer models and take a thermodynamic point of view, where the long chain limit is taken. Using the real-space Renormalization Group (RG) approach and an exact iteration method on a hierarchical lattice of dimensions $d > 2$ we show the possibility of a three-strand DNA bound state in conditions where a duplex DNA would be in the denatured state. Such a loosely bound state which occurs at or above the duplex melting point is a biological analogue of the nuclear or cold atom Efimov state and we call it an Efimov-DNA. From the RG flows and the thermodynamic phase diagram we find that the three chain bound state dissociates at a higher temperature than the duplex melting. All these transitions are induced by the bubble formations.

From the classical phase transition point of view, we further analyze the Efimov phenomena by looking at the zeros of the partition functions. The distribution of zeros comes out to have a very beautiful structure on the complex plane of the Boltzmann factor. Apart from this structure, the separator of two types of flows to the two different stable fixed points identifies the transition point as a limit point on the real axis in the thermodynamic limit. Here we study the partition function of the three chain system by combining the recursion relations and the RG transformations, and then finding the zeros. We also extend the model to the three chain repulsive interaction regime and a striking result that emerges is that in a higher dimension for example $d > 8.596$ a transition can be induced from the critical state to the Efimov-DNA. In addition, we discuss several other features of the zeros in the complex plane, for instance the detailed structure, and the connection to the Julia set.

We also study the melting of three directed polymers on a Sierpinski Gasket to observe the Efimov effect. Here the dimension of the fractal lattice is $d = 1.58$. We show that the Efimov effect occurs even in the lower dimensions provided some specific interactions are considered among the polymers. Based on the conditions for crossing and mutual interaction, we classify different polymer models. Furthermore we obtain a new state to be called a mixed or anti-Efimov state. The average energy calculations show that the mixed state is a separate state but the Efimov state, just a cross over.

B-DNA (right-handed helicity) is the most common form of DNA found under normal physiological conditions. Often Z-DNA (left-handed helicity) appears in presence of high salt concentration, cations or negative super-coiling. Although the Z form is transient in vivo due to the lack of a friendly environment, still the B-Z transition is relevant in several diseases. Many theoretical and experimental attempts of a detailed understanding of the transition mechanisms have been carried out for a long time. The transition via the base pair separation followed by the base pair flipping or the base pair flipping without any base pair separation are the two existing hypotheses on the B-Z transition mechanism. We consider a coarse-grained thermodynamic model based on chiral symmetry. We model a free energy like entity and restrict the geometry to the one dimension only, which may shed some light on the current controversies on the transition mechanism of the B-DNA to Z-DNA. Using the theory of wave front propagation we find that there is a dynamic phase transition in the conformational conversion of B-DNA to Z-DNA and obtain the dynamic phase diagram. The diagram shows that for the specific choices of the system parameters the dynamics allows the formation of the intermediate denatured state even though it is thermodynamically forbidden.

List of Publications

[1] **Jaya Maji** and S. M. Bhattacharjee, EuroPhys. Letts. **81**, 30005 (2008), *Nonequilibrium tricriticality in one dimension.*

*[2] **Jaya Maji**, S. M. Bhattacharjee, F. Seno, and A. Trovato, New J. Phys. **12**, 083057 (2010), *When a DNA triple helix melts: an analogue of the Efimov state.*

*[3] **Jaya Maji** and S. M. Bhattacharjee, EuroPhys. Letts. **92**, 58004 (2010), *Dynamic phase transition in the conversion of B-DNA to Z-DNA.*

[4] P. Sadhukhan, **Jaya Maji**, and S. M. Bhattacharjee, EuroPhys. Letts. **95**, 48009 (2011), *Type II DNA: When the interfacial energy becomes negative.*

*[5] **Jaya Maji** and S. M. Bhattacharjee, Phys. Rev. **E 86**, 041147 (2012), *Efimov effect of triple stranded DNA: Real Space Renormalization Group and Zeros of partition function .*

*[6] **Jaya Maji**, S. M. Bhattacharjee, F. Seno, and A. Trovato, arXiv:1306.4206, *Strange phases in three stranded DNA-models at low dimensionality.*

(*) indicates the papers on which this thesis is based.

1

Introduction

When there is life there is DNA. There is no way to begin life without it—a molecule contained in all organisms and cells. Essentially, DNA is *the* leading character for life's processes. Deoxy-ribo-Nucleic Acid, DNA in short is a long polymer made from repeating sub-units, *viz.*, nucleotides, connected by covalent bonds. A nucleotide consists of a 5-carbon sugar, a nitrogen containing base, and a phosphate group. The bases of DNA are adenine (A), cytosine (C), guanine (G) and thymine (T). A strand of DNA prefers base pairing via hydrogen bonds with the bases of a complementary polymer. As a matter of fact the two strands entwine around each other in antiparallel fashion in the shape of a double helix. The first correct double-helix model of DNA structure was proposed by James D. Watson and Francis Crick in the year of 1953, which laid the foundation stone for molecular biology [1]. The complementarity of the bases is an essential factor in making an identical copy of a parent DNA during DNA replication thereby maintaining inheritance. They do have interesting behavior and special physical properties because of their large size and equal sequence base pair interactions. DNA's are being studied for last few decades at various length scales for its immense biological implications [2, 3].

In recent times the formation of a triple-helical DNA has become a topic of considerable importance because of its possible implications in the field of molecular biology. In 1957, it was discovered that certain sequences of a Watson-Crick-double helical DNA allow a third strand to form a triple helix [4]. Felsenfeld, Davis and Rich first showed the formation of the triple helix in nucleic acids, which was later on confirmed by several other groups [5, 6]. To decode the genetic code, a double helical DNA has to be unzipped to reveal the bases. Quite strikingly, a third strand can identify the base sequences, not by opening the double helix but rather by forming a triple helix.

1.1 Triple helix

Oligonucleotides of three strands of DNA wind around each other to form a triple helix DNA as shown in Fig. 1.1. Watson-Crick DNA duplex has the room in its major groove for an additional strand. At ambient temperatures, the double helix is formed with

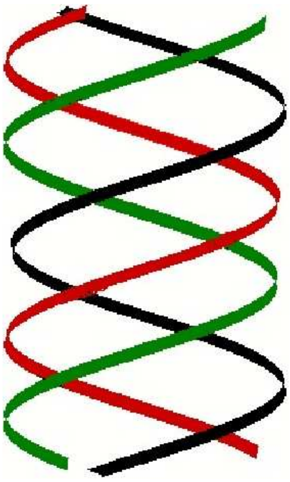

Figure 1.1: Schematic diagram of triple stranded DNA.

classical Watson-Crick base pairing (see Fig. 1.2(a)) while the third strand forms non-classical Hoogsteen (see Fig. 1.2(b)) or reverse Hoogsteen base pairing with one of the other two [1, 7, 2]. The known structures suggests that the central strand of a triple helix has to be purine rich (G or A), so that the third strand can provide the two hydrogen bonding surfaces to form two different types of base parings. The pyrimidine rich third strand forms non-classical Hoogsteen base pairing when it binds to a purine rich strand of the duplex in a parallel fashion while reverse Hoogsteen when a Purine rich strand binds to another purine rich strand of the duplex in an anti-parallel fashion. Triple helices can also be formed with DNA-RNA [8] and DNA-PNA (peptide nucleic acid), whose uncharged peptide backbone helps in the stabilization of the triplet structure [9, 10]. PNA is an artificially created biologically relevant molecule and might offer intriguing possibilities in the therapeutic applications. Some of the triple helix forming triplet structures of bases *e. g.*, T-A-T and A-A-T are shown in Figs. 1.2(c) and 1.2(d).

The 1957-discovery of a three-stranded DNA remained a curiosity till the recognition in 1987 that a third strand DNA can actually recognize the base sequence of the double helix even without opening it. Owing to its enhanced stability that can affect activities like gene expression, transcriptional inhibition, DNA replication and others requiring DNA opening, triple helix kindled new hopes in therapeutic applications [11]. Till date it has been possible to make and study triple helices in vitro, amidst high hopes of their relevance in vivo [12, 13]. The structure of a triple helix is surprisingly resistant to thermal dissociation compared to the double helical DNA. The Oligonucleotides forming triplex DNA dissociate at higher temperatures than the duplex melting [14].

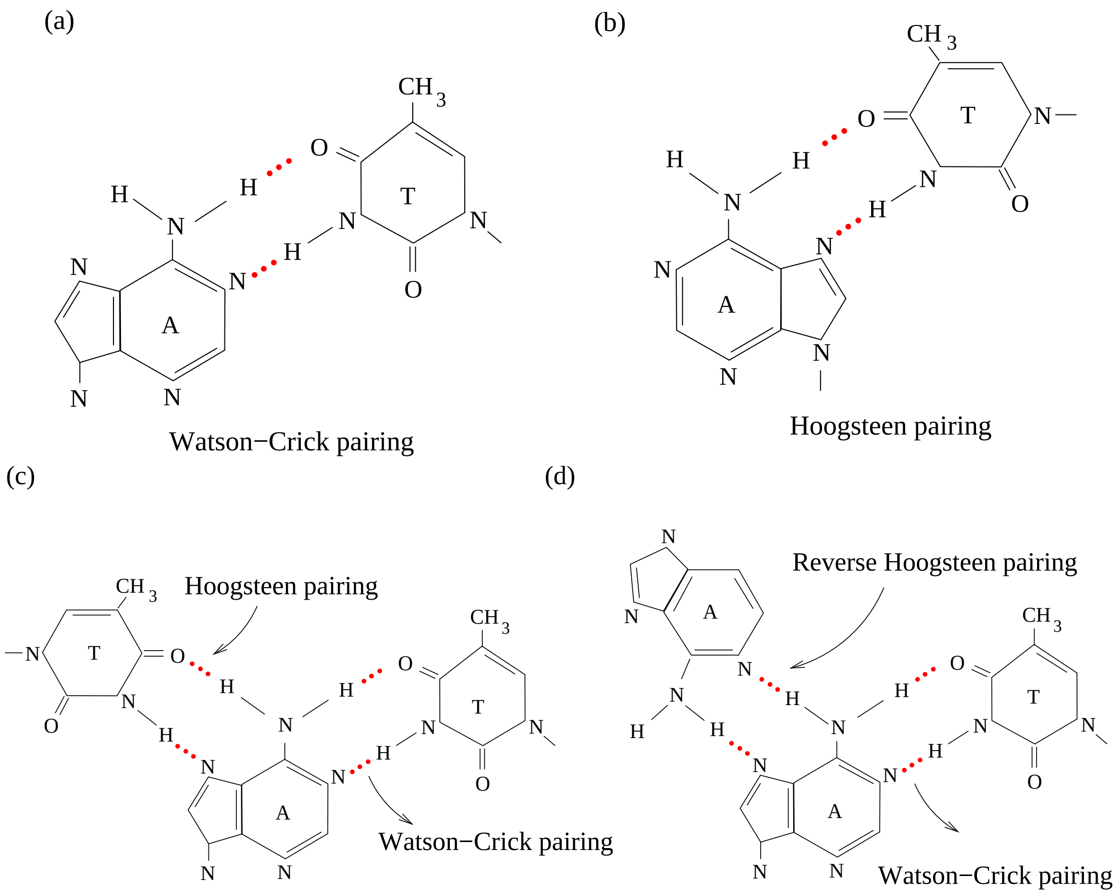

Figure 1.2: Red dotted lines are the Hydrogen bonds. (a) Watson-crick basepairing between A and T bases. (b) Hoogsteen basepairing between A and T bases. (c) Triple helix forming base triplet T-A-T. (d) Triple helix forming base triplet A-A-T.

1.2 Efimov effect

An unexpected phenomenon to turn up in the quantum three-body problem was first pointed out by V. Efimov in 1970 and now bearing his name in three-body non-relativistic quantum mechanics [17, 18]. It is such an unusual effect that even after 40 years of its discovery it is still of great interest. He predicted from his studies on nucleons that the three particles can have an infinite number of bound states eventhough no pairs are being bound. If the three particles are subjected to a short range pair interaction such that a pair would have a zero energy state, an effective long range interaction emerges due to quantum fluctuations. Thus infinitely many bound states appear at the critical threshold of the two-body binding. As one moves away from the critical point, the number of bound states decreases and vanishes at a point of unzipping of the three particles. Surprisingly, this effective three-body interaction is universal in nature and is actually independent of the detailed form of the pair potentials as well as the range of the potential. The origin of the quantum Efimov effect is the scale free quantum fluctuation near the zero-energy threshold of the two-body binding. The overall size of the effective three-body bound state is much larger than the range of pair potentials [18, 19, 20, 21]. There are several theoretical and experimental investigations using different models and methods that show this effect. Many years since its discovery, it is now seen in systems over various length scales ranging from nucleons (halo nucleus) to atomic physics and ultra-cold atoms under Feshbach resonance [22, 23, 24].

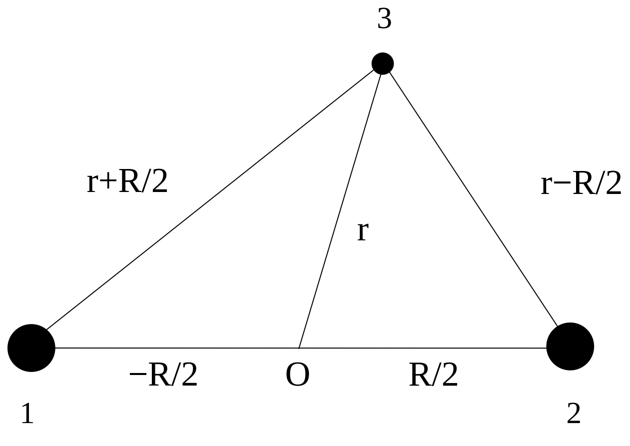

Figure 1.3: Two heavy (M) and one light (m) particles are shown with the position vectors. 1 and 2 are at a distance R and 3 is at a distance r from the center of mass O of 1 and 2.

There are many complex analytical and numerical methods to show the Efimov effect. For example, Efimov obtained the effective potential by studying the three-body system in hyperspherical coordinates. Fonseca *et al.*, used the Born-Oppenheimer approximation to study the Efimov effect in a model consisting of one light and two heavy particles of mass m and M, respectively, as shown in Fig. 1.3, interacting by means of a short-range pair potential. If the interaction between the heavy-light particles has nearly zero energy bound state, the large size of this bound state induces a long range attractive potential of $1/R^2$ type between the two heavy masses as if the small particle is shared by the two heavy masses. Thus an effective potential between the heavy masses emerges in the form of

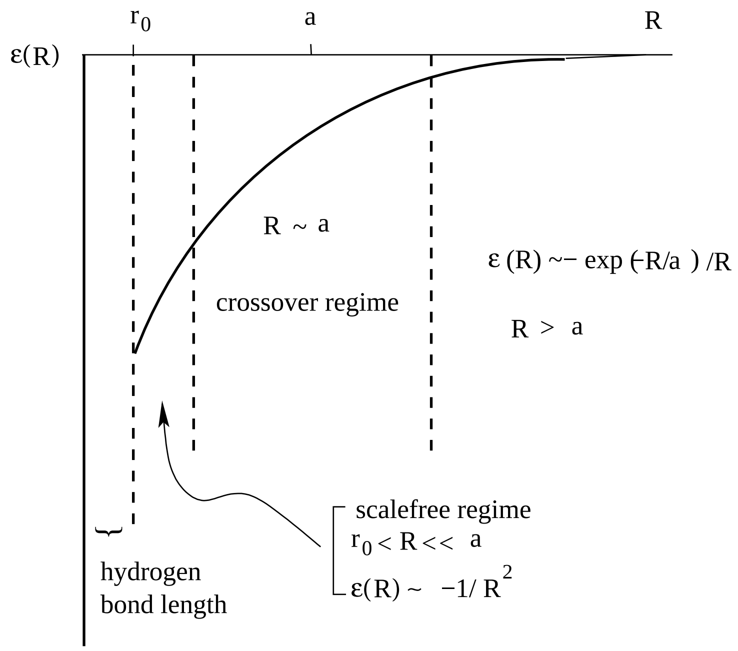

Figure 1.4: The effective interaction $\epsilon(R)$ between 1 and 2 from Fig. 1.3. An effective three-body bound state (Efimov effect) occurs in the region $r_0 < R << a$ and extends over the whole range for $a \to \infty$.

$$\epsilon(R) - \epsilon_0 \sim \frac{1}{R^2}\left(\frac{2}{a}Re^{-R/a} + e^{-2R/a}\right), \tag{1.1}$$

where a is the width of the pair wave function or the scattering length of the heavy-light particles and ϵ_0 is the heavy-light binding energy. For $a \to \infty$, Eq. (1.1) should be independent of a, so that in this limit, the effective potential emerges as $-\frac{1}{R^2}$, which is a 'universal' interaction for a region $r_0 < R << a$, where r_0 is the range of pair interaction. Moreover one sees a cross-over from $-\frac{1}{R^2}$ for $\frac{R}{a} << 1$ to the Yukawa form $\frac{e^{-R/a}}{R}$ for $\frac{R}{a} \sim O(1)$ as shown in Fig. 1.4. Here $\epsilon(R)$, comes as the separation constant when the composite Schrodinger equation of the three-particle model is treated in the Born-Oppenheimer approximation.

The Schrodinger equation for the three-particle system shown in Fig. 1.3 is written in the center of mass frame as

$$H\ \Psi(\mathbf{r},\ \mathbf{R}) = E\ \Psi(\mathbf{r},\mathbf{R}), \tag{1.2}$$

where H is the Hamiltonian and E, the eigenvalue. The wave function $\Psi(\mathbf{r},\mathbf{R})$ is associated with the boundary condition that it vanishes as either r or R becomes infinity. The separable ansatz is of the form

$$\Psi(\mathbf{r},\mathbf{R}) = \psi(\mathbf{r},\mathbf{R})\Phi(\mathbf{R}), \tag{1.3}$$

where the wave function $\psi(\mathbf{r},\mathbf{R})$ describes the motion of the light particle when the heavy masses are at a fixed distance $\mathbf{R}$, and $\Phi(\mathbf{R})$ describes the motion of the heavy particles. With the Born-Oppenheimer approximation Eq. (1.2) separates into a pair of equations. Thus the heavy and the light particle equations become

$$\begin{aligned} H_M\Phi(\mathbf{R}) &= E\Phi(\mathbf{R}), && (1.4)\\ H_m\psi(\mathbf{r},\mathbf{R}) &= \epsilon(R)\psi(\mathbf{r},\mathbf{R}), && (1.5) \end{aligned}$$

with appropriate Hamiltonians H_M and H_m of the heavy and the light particles, respectively. The eigen value $\epsilon(R)$ of Eq. (1.5) appears as the extra interaction potential in the Hamiltonian for the two heavy particles.

1.3 Quantum Analogy

Due to the sequential base pairing of DNA, there is a direct analogy between DNA and quantum mechanics [25]. There is an exact mapping of the partition function of two ideal polymers with DNA base-pairing type short range interaction to the Green function of the two-particle quantum mechanics in a potential under a transformation of the length of the polymers to the imaginary time. This in turn maps the ground state energy of the particle to the free energy of the polymer per unit length.

Following this analogy, the universality of the Efimov phenomenon encompasses the analogous classical model, namely the melting of three-stranded DNA. Here, for the occurrence of such phenomena, the critical thermal fluctuations from the classical domain play a role analogous to that of quantum fluctuations. A scaling argument has been used in [26] for three ideal polymers, which justifies the occurrence of the effective two-chain attractive potential $\frac{1}{r^2}$ as a source of the Efimov effect. Such a long range interaction leads to a broad three-strand DNA bound state at or beyond the melting point of a duplex DNA. This is a state where no two are bound but the three are bound together.

Such a loosely bound state is called the Efimov DNA [26].

1.4 Random Walk

The ideal chain is the most simplified model to describe a polymer as a random walk by excluding any kind of monomer interactions. If a polymer consists of N number of monomer-monomer links of unit length, keeping one end fixed at the origin, the average position of the other end will be zero, but the size of the polymer (see Fig. 1.5) will be given by the root mean square of the end to end vector $\mathbf{r}$ as

$$R \sim < r^2 >^{1/2} \sim N^{\nu}. \tag{1.6}$$

The size exponent $\nu = 1/2$ is for the ideal polymer but not in general. The random walk is closely related to a model of a directed walk. A walk is called directed when it advances in a preferred direction and does not go in the opposite direction. For a directed walk the transverse and the longitudinal sizes of the polymer are given by

$$R_{\perp} \sim < r^2 >^{1/2} \sim N^{\nu_{\perp}}, \quad \text{with} \quad \nu_{\perp} = 1/2, \tag{1.7}$$

$$R_{\parallel} \sim < r^2 >^{1/2} \sim N^{\nu_{\parallel}}, \quad \text{with} \quad \nu_{\parallel} = 1. \tag{1.8}$$

These exponents are independent of the dimensionality. Real polymers are studied by the self avoiding walk models, where excluded volume effects are crucial [28, 29]. As we deal with the ideal chain in this thesis, we will not go into the other random walk models. Fig. 1.5(a) shows a polymer in a continuum limit while Fig. 1.5(b) shows a discretized form of the polymer chain when placed on a square lattice.

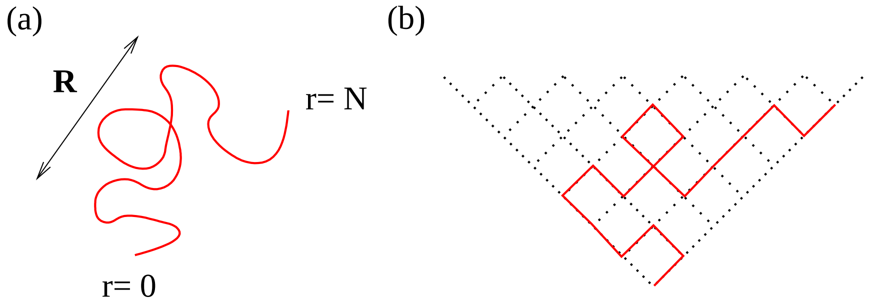

Figure 1.5: (a) A polymer as a random walk (not directed walk) is shown. One end of the polymer is fixed at $r = 0$. The other end is at $r = N$. Here N is the number of monomer-monomer links of unit bond length and $\mathbf{R}$ is the size of the polymer. (b) The discrete form of the polymer walk on a square lattice of $1 + 1$ dimension is shown.

When polymers are on a lattice as random walks, a single monomer essentially represents several base pairs. Often simplified directed polymers are useful for studying global properties that depend on the large length of polymer, temperature, etc. Various physical properties of the polymeric systems including melting, unzipping and other thermodynamic quantities have been studied on real lattices *e. g.*, square, cubic, honeycomb etc. and on pseudo lattices *e. g.*, hierarchical, fractal etc. using directed polymer chain [30].

1.5 Hierarchical lattice

A hierarchical lattice provides one of the most convenient media to study many critical phenomena and other physical problems. Hierarchical lattices are constructed by a recursive replacement of a motif. The geometric construction of such a lattice looks similar at a different scale no matter what size it is viewed at [31]. These special lattices do not have any proper Euclidean coordinates. Consequently the metric is not defined in such lattices. Such pseudo lattices were introduced as simplified structures to study various statistical mechanical problems. Their simplicity has motivated a lot of work. Although these lattice models are relatively easy to handle, they provide a very detailed results. Several models, such as the Ising, Potts and polymer systems are exactly solvable on these lattices [32, 33, 34, 35]. Diamond structured lattice, Honeycomb structured lattice etc. are the examples of hierarchical lattices. Such lattices have a much lower symmetry compare to the Bravais lattices, which in turn may provide insights into other lower symmetry problems. Essentially all these features have led hierarchical lattice models as a testing ground for many new concepts. Directed polymers on hierarchical lattices were studied as model of random system in Ref. [32, 36, 37, 38]. The case of random interaction was studied by Derrida *et al.*, Cao and by Mukherji *et al.*,. More recently, the hierarchical lattice models were exploited in the study the dynamics of glassy materials, spin glasses, percolation cluster etc. [39, 40, 41, 42]. Chakrabarti *et al.*, have studied the electronic properties on such lattices [43].

1.5.1 Diamond hierarchical lattice

To construct a diamond hierarchical lattice one starts with a single bond and then in the next generation that single bond is replaced by a motif of λb bonds, where b is the branching factor and λ is the bond length scale factor. Again in the next generation each bond is replaced by a motif of λb bonds. A construction of the lattice is shown in Fig. 1.6. Thus by an infinite iteration ($n \rightarrow \infty$) one obtains an infinite lattice whose

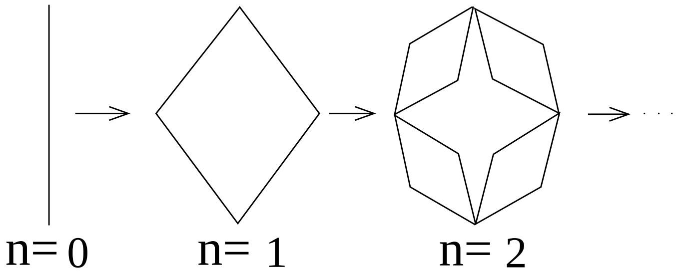

Figure 1.6: The recursive construction of the hierarchical lattice is shown for $n = 0, 1, 2, ...$ generations. The diamond motif is for $b = 2$ and length scale factor $\lambda = 2$.

dimensionality is given by

$$\lambda^d = \frac{v_{n+1}}{v_n} \quad i.e. \quad d = \frac{\ln \frac{v_{n+1}}{v_n}}{\ln \lambda}, \tag{1.9}$$

where λ, d, v_{n+1}, v_n are associated with length rescaling factor, dimension, and number of bonds of the hierarchical lattice at $(n+1)^{\text{th}}$ and n^{th} generation, respectively. For this particular lattice model with $b = 2$ and $\lambda = 2$

$$\lambda^d = \frac{(\lambda b)^{n+1}}{(\lambda b)^n} \quad i.e., \quad d = \frac{\ln \lambda b}{\ln \lambda} = \frac{\ln 4}{\ln 2} = 2. \tag{1.10}$$

The branching factor b controls the dimensionality of the lattice, *e. g.,* for $b = 3$, $d = 2.58496$, for $b = 4$, $d = 3$ and so on. Two other examples of the hierarchical lattices are shown in Fig. 1.7. These lead to structures with dimensions $d \geq 2$.

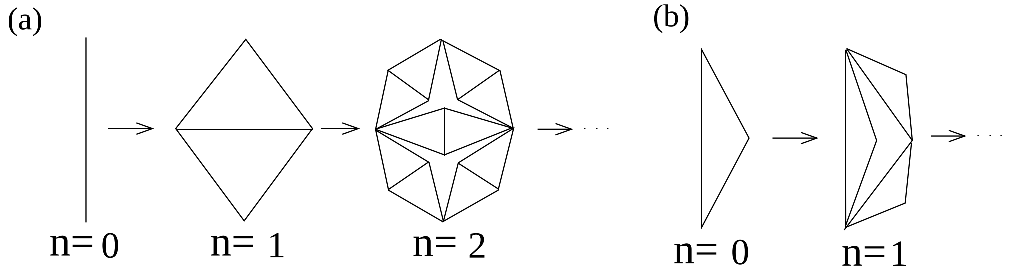

Figure 1.7: The recursive constructions of the hierarchical lattices.

1.5.2 Fractal lattice: Sierpinski gasket

There is a different class of lattice, called fractals with lower dimensions. Sierpinski carpet, Sierpinski gasket are examples of regular fractals which are extensively exploited to study critical phenomena. The scale invariance of such lattices allows one to apply the real-space renormalization group (RG) methodology. The results are also amenable to exact solutions. Some of the constructions of the fractal lattices are depicted in Fig. 1.8.

Sierpinski gasket was invented in 1916 by Polish mathematician Waclaw Sierpinski. This is embedded in a Euclidean space. See Fig. 1.8(a). In this case the scaling factor of each line is 2. In the first generation of the construction a single triangular motif is divided into four self similar structures of the triangular shape. Out of the four triangles, the middle triangle is removed from the space. Subsequently in the next generation the rest of the three follow the same procedure. Thus a Sierpinski graph is constructed in an iterative manner. For this particular structure the number of bonds is 3^{n+1} and the number of sites is $\frac{3(3^n+1)}{2}$. The effective dimensionality is given by

$$d = \frac{\ln N_n}{\ln s_n}, \tag{1.11}$$

where $s_n = \lambda^n$ with the bond length scaling factor $\lambda = 2$ and N_n is the number of the self similar structures at n^{th} generation. This is a general definition of finding the dimensionality of any structure. The Sierpinski gasket is the most common regular fractal used in studying different statistical models, for instance the Ising model, the directed or the self avoiding polymer models, Potts model etc. Furthermore the sandpile model, self avoiding walk and directed polymer models have also been studied on Sierpinski gasket

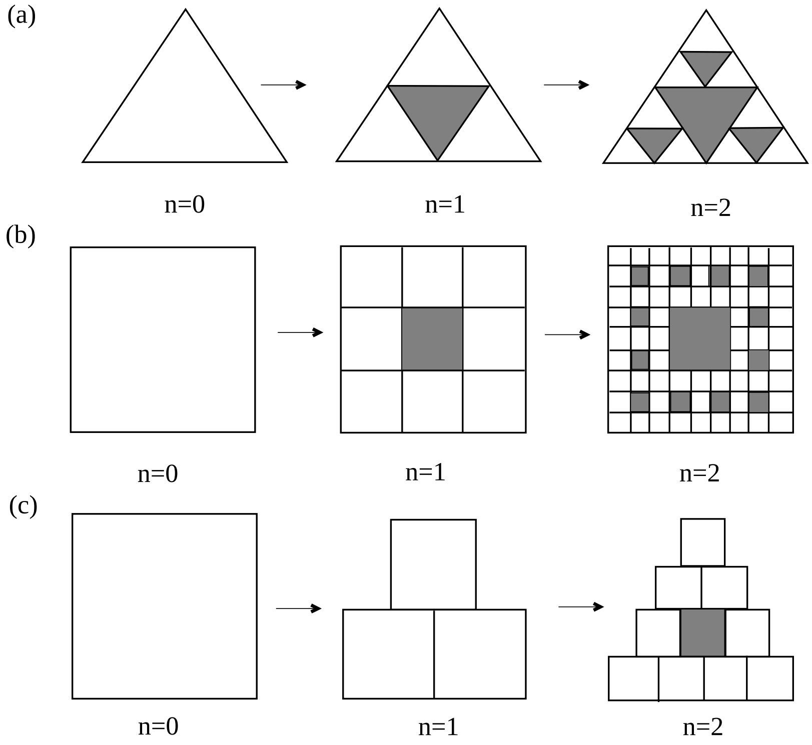

Figure 1.8: Constructions of the fractal lattices.

fractals of different dimensions using the real-space RG approach [44, 45, 46, 47].

1.5.3 Real-space Renormalization Group

RG is well discussed in many text books [48, 49]. Here we give a brief description about RG. RG is a standard technique in condensed matter physics and already has been used in many other branches of physics. It is a tool to investigate a physical system at a different length scale without any change of the underlying physics. Many real-space RG methods have been developed in obtaining approximate RG transformation. The speciality of the hierarchical lattice is the scale invariance property. This is what enables one to implement the real-space RG technique to study many models [31, 32, 34, 35]. To implement RG one starts from a large lattice and removes short scale fluctuations by renormalizing the parameters such as the coupling constant etc., by rescaling the lattice to the original size. This procedure of thinning out of the degrees of freedom and rescaling is followed in each step of the RG decimation. The RG relation of the coupling constant emerges from this repeated procedure. The fixed points obtained from the RG relation, describe the phase transition.

1.6 Zeros of the partition function

Finding zeros of the partition function in the complex plane of any physical variable is a mathematical way to understand the phase transition phenomenon. However finding zeros is possible only for small lattice sizes or when a partition function reduces to a polynomial form, but not in general. The zeros of the partition function are the complex values of the Boltzmann factor or other parameters at which the partition function vanishes.

Yang and Lee first studied the Ising ferromagnetic system in a complex magnetic field to show that for a properly chosen variable the zeros lie on a unit circle, known as the Yang-Lee circle [50, 51]. Later the zeros were studied in the complex temperature plane and other variables [52]. Since there cannot be any real zero, the zeros may accumulate and pinch the real axis as a limit point in the thermodynamic limit. This method can provide relevant information on phase transitions such as the critical field or temperature and the values of the associated critical exponents.

1.7 Julia set

The distribution of the zeros of the partition function on a complex plane may form many complicated structures other than a circle. These structures are nothing but the separatrices of the two types of flows, to the two different stable fixed points of the RG transformation and are similar to the Julia sets [53, 54]. The Julia set, named after French mathematician Gaston Julia, is a type of fractal generated by an iterative function over the complex numbers. The standard definition of a Julia set is the set of points on the complex plane which flow to a fixed point (no divergence) after a function, *e. g.*,

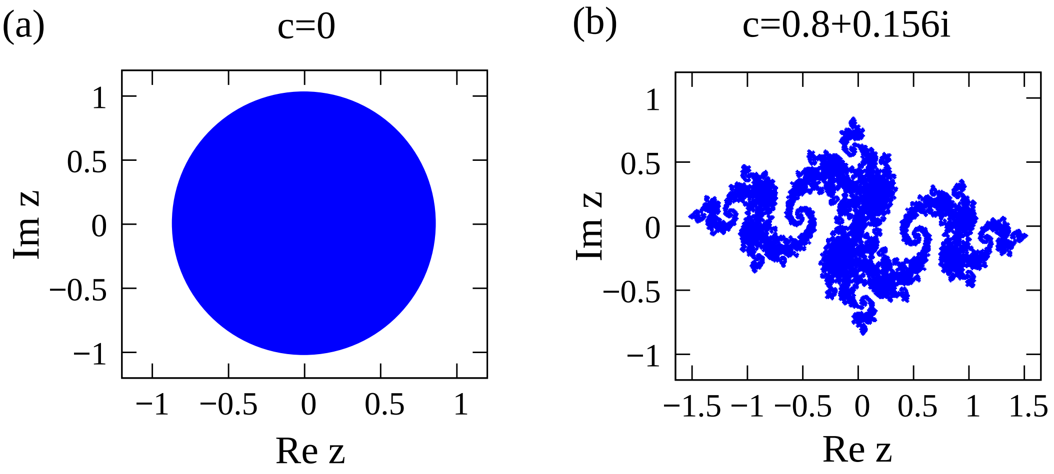

Figure 1.9: Julia sets in the complex z plane for (a) $c = 0$, which is an unit circle, (b) complex $c = 0.8 + 0.156i$. Except for $c = 0$, these sets exhibit self-similarity.

$$z_n = z_{n-1}^2 + c, \tag{1.12}$$

is repeatedly applied, where c is any arbitrary constant, real or complex. Let us choose $c = 0$.The fixed point solution for $c = 0$ are $z = 0, 1, \infty$, where $z = 1$ is the unstable fixed point. Here for $n \to \infty$, $z_{n+1} \to 0$, when started with $|z_0| < 1$ and $z_{n+1} \to \infty$, when started with $|z_0| > 1$. Therefore the unit circle $|z| = 1$ as shown in Fig. 1.9(a) is the boundary between the two stable fixed points $z = 0, \infty$. The unstable point lies on this boundary. For the different values of c (real or imaginary) different structures are obtained in the complex z plane as shown in Fig. 1.9(b). The study of such structures has applications in complex dynamics, partial differential equations, statistics etc. We will discuss several features of the zeros in the complex plane, and the connection to the Julia set in Chap. 3.

1.8 Studies on double-stranded DNA

Several lattice polymer models, have long been used for theoretical understanding of various aspects of DNA, especially its thermodynamics properties. Various analytical and numerical schemes such as generating functions, exact transfer matrix, RG and Monte Carlo simulations have been successfully applied in the studies of the melting and the unzipping of a double-stranded DNA [55, 56, 57, 32, 58]. The melting of DNA received a special attention as it the crucial step for DNA replication. The melting is the temperature induced separation of the two strands, which happens at a critical value of the temperature (T_c). This is also called the melting point or the denaturation point. The melting of a double helical DNA of large length, generally occurs in the range 80^oc–100^oc [59]. pH and chemical induced denaturation also have been studied. Depending on the model, melting could be continuous or discontinuous [56, 60, 61, 62]. For a review on melting of DNA see Ref. [63].

The critical behavior of two directed polymers has been studied by Mukherji *et al.*, on a hierarchical lattice by the real-space RG [32]. The two chain melting was shown. The critical exponents obtained from the RG found to describe the finite size scaling form of the energy derived from the exact iteration of the hierarchical lattice starting from a smaller lattice. The two chain model further was extended to the random or the disordered hierarchical lattice medium [36, 64, 65, 32]. The force induced unzipping of a dsDNA at a critical value of the force was first shown by Bhattacharjee in a continuum model of DNA [58]. The unzipping was reported as a first order phase transition. Further studies on the continuum and the discrete model were done by Sebastian and Marenduzzo *et al.*, [66, 56, 67]. The complete phase diagram in the force-temperature plane in this context was obtained by Kapri *et al.*, [68] by applying pulling force at any intermediate point of dsDNA. Various additional phases were obtained by Giri and Kumar for the direction dependent pulling forces [69]. Sadhukhan *et al.*, reported the existence of the typeII-DNA in a condition of negative zipped-unzipped interfacial energy [70]. Different single molecule experiments done with DNA are discussed in Ref. [59].

1.9 Studies on triple-stranded DNA

A lot of progress has been made recently in the structural understanding of the triple helix DNA [71, 72]. There have been a number of studies in vitro that have directly tested the formation of a triple-stranded DNA [5, 6, 73, 13]. So far most of the efforts were directed towards understanding the bound state of the triple-stranded DNA.

Triple helix is not a stable structure under normal physiological conditions and is highly specific. The sequence-specific recognition of the duplex DNA by a third-strand is of great use in targeting particular sites of the duplex DNA. It has been reported that the triple helix forming Oligonucleotides (TFO) might be a universal drug in recognizing the specific sequences of the duplex DNA [11, 71]. It has been shown that the peptide-or polyamide- nucleic acids (PNA) can bind to DNA and RNA with higher affinity than natural Oligonucleotides to form a triple helix [74, 75].

The stability of the triple helix DNA is of importance for possible biological applications. Several studies have been aimed towards stabilization of DNA triplexes at physiological conditions [76]. Its stability is a function of temperature, salt concentration and pH. The thermodynamical studies on the triple helix formation have been reviewed in Ref. [77, 72]. Plum has presented a state diagram on the complex behavior of the triple helix DNA. An Oligonucleotide hairpin, forming a triple helix with a single-strand was found more stable than a triple helix composed of the two Oligonucleotides and a single-stranded DNA [14, 15, 16]. The latter one underwent two distinct melting transitions. Furthermore many experimental results demonstrated that the denaturation temperature of the triplex DNA is much higher than the melting of the duplex DNA [78].

1.10 Conformational transition

The conformational transitions of various biomolecules are often related to their biological functions. For last few decades many experimental and theoretical models have been explored to study the interconversion of DNA. It is known that dsDNA exists in many possible conformations like B-DNA, A-DNA, Z-DNA etc. Although B-DNA is very common under normal physiological conditions, Z-DNA appears in functional organisms under certain circumstances. The B form also converts to A-DNA under dehydrated condition or C-DNA in certain solvents. However, the B-Z conversion is challenging because of the change in the helicity. Here we give a very brief review of the structural form of B- and Z-DNA, and the interface between B- and Z-DNA. We also discuss the different mechanisms proposed for the conformational transition.

1.10.1 B-DNA

The most common form of DNA found under normal physiological low salt conditions is the B-DNA [1, 79], the well known double helix with a right handed helicity as pictured in Fig. 1.10(a). The structure of B DNA was originally proposed in 1953 by Watson and Crick. It has 10.5 base pairs per helical turn and two distinct grooves, a major and a minor groove. The Watson-Crick base pairs are stacked at the center of the helix formed by the phosphate backbones.

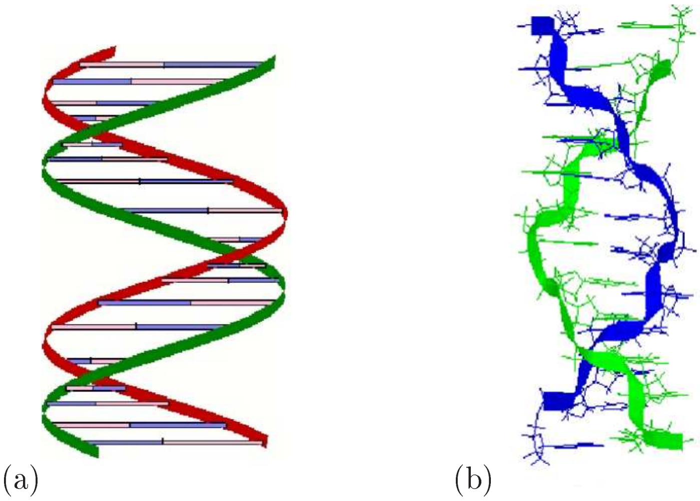

Figure 1.10: (a) Schematic structure of B DNA with right handed helicity. Two single strands paired by A-T and G-C type base pairs. Base pairs are shown by the horizontal lines. (b) Schematic structure of Z DNA (taken from Wikipedia) with left handed zigzag helical form.

1.10.2 Z-DNA

Quite surprisingly, the first DNA structure to be solved by X-ray crystallography turned out to be a left handed zig-zag form called Z-DNA [2, 80, 81, 82]. The structure of Z DNA is substantially different from B-DNA. It has 12 base pairs per helical turn and has a narrow groove nearly similar to the minor groove of B-DNA. The structure of Z-DNA is shown in Fig. 1.10(b). Such a non-Watson-Crick structure would have profound implications in DNA replication, recombination and transcription. The Z form of DNA is found to be transient in vivo due to the lack of a friendly environment. However it can be stabilized in vitro in presence of high salt concentration, cations and negative super-coiling. Z-DNA is found in a number of eukaryotic cells, animal cells, plant cells and in bacterial cells *e. g.*, *E-Coli*.

1.10.3 B-Z transition

The conformational transition from the B to the Z form of DNA was discovered in 1972 by Phol and Jovin [83]. As the fundamental difference between two forms is associated with the helicity, the transition goes through a dramatic conversion at the molecular level. This conformational transition requires the base pairs and a subset of backbone sugar rings to flip, followed by other changes. The transition can be induced by several schemes such as ionic concentration, negative super coiling etc. Inducing the conformational transition between two such chiral phases is tantamount to a lowering of the free energy of Z compared to B, making Z the most preferable state, or the other way around [84]. It has been argued that the B-Z conversion is relevant in poxviruses [85], and Alzheimer's disease [86]. The B-Z transition is reported to be first order in nature [80, 87, 88, 89, 90]. As the base pairs and a subset of the backbone sugar rings have to flip to convert B to Z, the dynamics offers intriguing possibilities [81]. Only recently methods have been developed to explore the dynamics in single DNA as opposed to earlier studies in solutions.

1.10.4 The B-Z interface

One can characterize the B-Z transformation by a growth of a suitable domain over the bulk of DNA. In any such scenario, the B-Z interface, the separator between the two chiral phases, plays an important role. The equilibrium interface has been characterized structurally and from other studies. The structure of a short oligomer in presence of a Z-DNA binding protein at 2.6A resolution indicates broken base pairs separating the B and the Z phases. The protein acting as an external source inducing the transition is expected to produce a sharp interface [91]. A very ingenious way of studying the interface is to use mirror DNA [92, 93], though it cannot be used for the chirality changing transition. Interfacial studies and melting of short B-B* oligomers, where B* is the enantiomer of B, show that the junction mimics the B-Z junction, and the interface broadens as the melting point is reached. In contrast to these equilibrium cases, the nature of the interface during the transition depends on the nature of the transition mechanism [88, 89]. Several such schemes are in vogue and discussed in detail in Ref. [81].

1.10.5 Contradictory hypotheses

The conformational conversion of B to Z has been studied by using different types of single molecular experiments. In an experiment by D. A. Heller *et al.*, [94], a conformational transition from the B form to the Z form of DNA was observed. The B-Z transformation for a short 15 base pair GT (non-Watson-Crick wobble base pair) DNA wrapped on the single walled carbon nanotube was monitored as a function of time by the addition of counter-ions. The nanotube helped in identifying the phases via accurate measurements of the band-gap in a simpler geometry. This transition is completely reversible and is thermodynamically identical to the transition seen in the absence of the nanotube. *The results seem to indicate the formation of a denatured* DNA *during the transformation*, eventhough a denatured state under the experimental conditions is not possible thermodynamically.

A different single molecule experiment studied the transition under a tension and negative super-helicity by combining FRET with magnetic tweezers [95]. This experiment on an effectively $(GC)_{11}$ DNA (i.e. 22 bases) *seems to favour a single interface between* B *and* Z *without any denatured bubble.*

The two main competing hypothesis for the B to Z transition mechanism are the following:

1. via base pair separation followed by base pair flipping [80],
2. via base pair flipping without any base pair separation [87].

In the first case there could be a denatured intermediate state while in the second there could be a Z type but following the standard Watson-Crick base pairing (ZWC-DNA).

1.11 Aim

The aim of this thesis:

- Our aim would be to look for the signature of an Efimov-like effect in triple-stranded DNA. We will study the melting of a three-stranded DNA, the possibility of other phases, and the phase diagrams. In order to study the thermodynamic behaviour we will take the large length limit. We will model three directed polymers on a hierarchical lattice and further on a Sierpinski gasket. We will apply the real-space renormalization group (RG), the exact iteration method, and then the procedure of finding the zeros of the partition functions. We will use the finite size scaling analysis for a further investigation on the nature of transitions and explore the model in different dimensions ($d < 2$ and $d > 2$) to see the dimensional effect on different possible states.

- In connection to the existing hypotheses on B-Z transition our aim would to establish a theoretical understanding towards this conformational transition. We will use a general form of the the Landau free energy describing three states B, Z and the denatured state as

  $$F(\phi) = \frac{\alpha\beta}{2}\phi^2 - \frac{\alpha-\beta}{3}\phi^3 - \frac{1+\alpha\beta}{4}\phi^4 + \frac{\alpha-\beta}{5}\phi^5 + \frac{1}{6}\phi^6,$$

  where $\alpha,\ \beta$ determine the free energy differences between the two states and $\phi(z,\ t)$ describes the state of the coarse-grained base-pair at index z along the DNA. Our emphasis will be on the underlying interface between the two relevant states. By the choice of the specific parameters we allow the fronts to propagate and study the dynamics of the transitions and draw the phase diagram in the α-β plane. We will use the wave front propagation methodology and the numerical approaches to determine the uniform velocity of these propagation. Furthermore, a perturbation technique will be used to justify the dynamic phase around the equilibrium point. We will also study the behavior of the width of the interface and the appropriate timescale.

1.12 Thesis organization

We study the melting of a three-stranded DNA and the conformational transition of B to Z DNA. The thesis is organized as follows:

In Chap. 2 we model three directed polymers on a hierarchical lattice. Polymers are placed from bottom to top, but they can wander at the intermediate step. The real-space RG approach and exact iteration method are used to show that, despite the tremendous simplicity of the model, the three-strand DNA exhibits an Efimov-like state. Such a state occurs at or above the duplex melting point, where three are bound but no two are bound. We show the feature of an enhanced stability of the triple-stranded DNA compared to the duplex-DNA by the numerical calculations for both the cases of symmetric and asymmetric pair interactions. We also show the nature of transitions of the two- and the three-chain systems.

In Chap. 3 we study the same model and follow the same approach as is discussed in Chap. 2. Here we study the partition function of the three-chain system by combining the recursion relations and the RG transformations and then finding the zeros. We show that the distribution of zeros gives Julia-set like structures in the complex plane of the partition function. We find that all the transition points obtained from RG flows, are in good agreement with the zeros of the partition function on the real axis. We also extend the model to the three-chain repulsive interaction region. We go to higher dimensions to show that a transition can be induced from the Efimov state of DNA to a critical repulsive state. We show that to be a continuous transition, obeying the finite size scaling law with the exponents obtained from RG.

In Chap. 4 we further model the three-chain system on a Sierpinski gasket fractal lattice. We show that the Efimov effect occurs even in lower dimensions if some specific interactions are assigned to the polymers. We study different models in detail and obtain a new state, to be called a mixed state.

In Chap. 5 we study the conformational transformation form B to the Z form by the theory of wave front propagation. The dynamics of B-Z interface is studied by writing down the nonlinear diffusion equation with a free energy like quantity. A dynamic phase diagram is obtained for the stability of the front separating B and Z. The instability in this front results in two split fronts moving with different velocities. We also show that a denatured state may develop dynamically eventhough it is thermodynamically forbidden if the system parameters are tuned accordingly.

2

When a DNA triple helix melts: an analogue of the Efimov state

In this chapter we study the melting of a three-stranded DNA on a hierarchical lattice. It is predicted here that a three-stranded DNA exhibits the unusual behaviour of the existence of a three-chain bound state in the absence of any two being bound. Such a state can occur at or above the duplex melting point. This phenomenon is analogous to the quantum Efimov state. In three particle quantum mechanics, such a state occurs via the development of an attractive $1/r^2$ interaction over a range beyond the short range potential. Here we have considered the classical coarse-grained model of a three-chain system in a discretized space. Real-space RG is used to show the Efimov-like three-chain phase. Further exact numerical calculations are used to validate the prediction of such a biological Efimov effect.

The chapter is organized as follows. We introduce a simplified polymer model on a hierarchical lattice in Sec. 2.1. In Sec. 2.2 the recursion relations from the RG decimation and for the exact iterations are written. Within this section, the subsequent subsections contain the results and the discussions from the RG and the exact iteration approaches. We draw our conclusions in Sec. 2.3.

2.1 Model

Let us consider three directed polymers on a hierarchical lattice, constructed recursively with a motif of λb bonds, as shown in Fig. 2.1(a), where λ and b represent the bond scaling factor and the branching factor, respectively. The lattice is generated iteratively by the replacement of each bond at the $(n-1)^{\text{th}}$ generation by a motif of λb bonds to get the n^{th} generation. In the thermodynamic limit $n \to \infty$, the effective dimensionality of the lattice is defined by

$$d = \frac{\ln \lambda b}{\ln \lambda}. \tag{2.1}$$

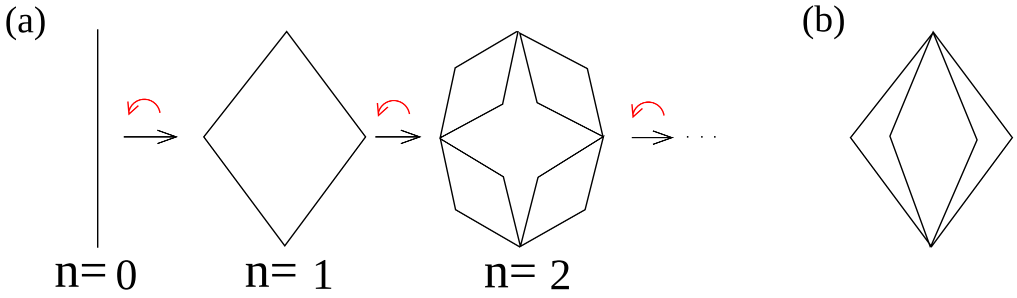

Figure 2.1: (a) The recursive construction of the hierarchical lattice with $b = 2$ for $n = 0, 1, 2, ...$ generations. At every stage, each line is replaced by a diamond of $2b$ lines. The right arrows represent the direction of iteration towards larger lattices. The left arrows represent the direction of decimation used in RG. (b) A motif of $2b$ bonds, where $b = 4$.

In this thesis we shall choose $\lambda = 2$. By changing the value of b, the dimensionality of the lattice can be tuned. For example the dimensionality of the lattice is $d = 2$ for $b = 2$ (see Fig. 2.1(a)) and $d = 3$ for $b = 4$ (see Fig. 2.1(b)). Since in lower dimensions a bound state always exists due to any shallow potential, a simple random walk[1] would not have the transition for $d \leq 2$. So we always choose $b > 2$ for a three chain model[2].

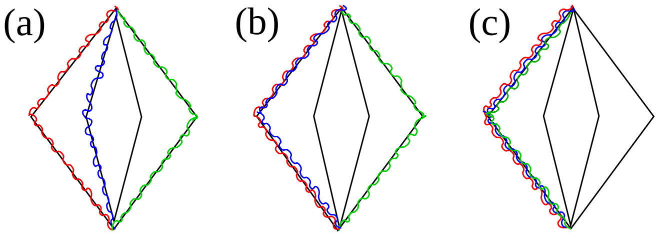

Figure 2.2: Examples of three-chain configurations on a diamond motif for $b = 4$. (a) Polymers do not share any single bond. The number of such configurations is $b(b-1)(b-2)$. (b) Two polymers share a bond and the number of such configurations is $b(b-1)$. (c) Three polymers share the same bond. The number of such configurations is b.

One major feature about hierarchical lattices is their unusual scale invariance property. They have a discrete scaling symmetry. That is why an exact implementation of the real-space RG technique is possible. The decimation of the n^{th} generation to arrive at the $(n-1)^{\text{th}}$ generation is precisely what is needed in an RG transformation. Once the partition function is known, it is possible to calculate the free energy, and the other thermodynamic quantities. One may even write down recursion relations for them.

Three chains on a hierarchical lattice are stretched from bottom to top, but they can wander at intermediate points. The contact energies are defined at the bonds only. The polymers are assigned attractive potentials $-\epsilon_{ij}$ and $-\epsilon_{ijk}$ $(\epsilon_{ij}, \epsilon_{ijk} > 0)$ if a single

---

[1] A simple random walk in d dimension, which is a directed walk along its length in $d+1$ dimension can be mapped to the path of a particle in quantum mechanics under imaginary time transformation.

[2] $d = 2$ with $b = 2$ is the lower critical dimension for a two chain system.

bond is shared by the two and the three polymers, respectively (see Fig. 2.2). At each generation, the length of each polymer increases by a factor $\lambda = 2$ so that the length of polymers at the n^{th} generation is

$$L_n = 2^n. \tag{2.2}$$

We have considered a coarse-grained model. What we call a monomer in fact represents several base-pairs. The interaction involves monomers with same sequence of different chains. The total energy for the two and the three strands for the $n = 1$ generation lattice as shown in Fig. 2.1(a), respectively, are given by

$$E_2 = -m_2\epsilon_{12}, \tag{2.3}$$

$$E_3 = -m_2\left(\epsilon_{12} + \epsilon_{23} + \epsilon_{31}\right) - m_3\epsilon_{123}, \tag{2.4}$$

where m_2 is the two-chain and m_3, the three-chain contacts.

For the Efimov effect, only pairwise interaction is enough. However in an RG procedure it is imperative to define the model with both ϵ_{ij} and ϵ_{123}, because the three-chain interaction gets generated on a longer scale.

We introduce the Boltzmann factors,

$$y_{ij} = \exp(\beta\epsilon_{ij}), \text{ and } \ w = \exp(\beta\epsilon_{123}), \tag{2.5}$$

where $\beta = 1/k_BT$, k_B being the Boltzmann constant, T the temperature.

2.2 Efimov-like phase in $d > 2$

We adopt a real-space RG approach for $d > 2$ to study the three-chain melting. In the RG approach, the effects of interaction is probed by summing over the configurations at a smaller scale (in the partition function) and redefining the effective interaction on a larger scale. This is done by preserving the form of partition function upto a scale factor. For a bound state, we should see an effective interaction among the chains, irrespective of the scale of coarse-graining. In contrast, for an unbound state, locally bound monomers lose their importance as we sum over configurations and therefore the effective interaction would vanish as the probing length scale increases. These effects are expressed by the RG flow equations or recursion relations, as flows of the interactions with length scale. A two-body bound state should therefore be possible if the two-body interaction does not vanish. In the same spirit, a three body bound state would occur if a three-body interaction becomes operative, even if there is none to start with. We express these RG relations in an exact form on specially constructed hierarchical lattices with discrete scaling symmetry and tunable dimensionality.

2.2.1 Efimov DNA: RG

The configurations of the two-chain system on a motif of the hierarchical lattice can be classified as

1. two independent chains,

2. inherently two-chain configurations *i. e.*, two chains sharing the same bond.

By summing over all configurations the partition functions for $n = 0$ and $n = 1$ generation lattices for general b will be written as [32]

$$Z_0(y) = y_{ij}, \tag{2.6}$$

$$Z_1(y) = b(b-1) + by_{ij}^2. \tag{2.7}$$

Since by RG decimation, a motif of $2b$ bonds of $n = 1$ generation is replaced by a single bond in $n = 0$ generation, the RG demands

$$Z_0({y'}_{ij}) \propto Z_1(y_{ij}), \tag{2.8}$$

where y' is the renormalized Boltzmann factor. With the free chain boundary conditions *i. e.*, $y_{ij} = 1$, implies ${y_{ij}}' = 1$, the proportionality constant of Eq. (2.8) can be determined. Therefore the RG transformation for the two-chain Boltzmann factor becomes

$${y'}_{ij} = \frac{b(b-1) + by_{ij}^2}{b^2}. \tag{2.9}$$

The RG transformation for the three-chain case can also be written in the same spirit as in two-chain case. The three-chain configurations (see Fig. 2.2) can be classified as

1. three independent chains,

2. a combination of a double- and a single-chain,

3. inherently three-chain configurations, *i. e.*, three chains sharing the same bond.

The free chain condition $y_{ij} = w = 1$ implies $y_{ij}^{'} = w' = 1$. Also to be noted that when three chains share the same bond the contribution is $y_{ij}^3 w$ (y_{ij}^3 for three pairs). The RG transformation for w is then

$$w' = \frac{b(b-1)(b-2) + b(b-1)\sum\limits_{i<j} y_{ij}^2 + bw^2 \prod\limits_{i<j} {y_{ij}}^2}{b^3 \prod\limits_{i<j} y_{ij}^{'}}, \tag{2.10}$$

where w' is the renormalized value of w. These recursion relations show that the three-body term is generated eventhough we start with $\epsilon_{123} = 0$, *i. e.*, $w = 1$. For given y_{ij} and w, the flows from successive use of Eqs. (2.9)-(2.10) would give us the phases and the nature of the transitions.

For the above analysis one needs the fixed points of the RG transformations. The three fixed points of y_{ij} correspond to

1. $y^* = 1$, stable infinite temperature fixed point representing an unbound state,
2. $y^* = y_c = (b-1)$, unstable fixed point representing the two-chain melting or critical point,
3. $y^* = \infty$ (zero temperature representing a bound duplex state) is the obvious stable fixed point, which does not come from the RG relation but comes from the RG flow.

In case there is no pairwise bound state (no pair interaction *i. e.*, $y_{ij} = 1$), w has three fixed points,

1. $w^* = 1$, stable infinite temperature, an unbound state,
2. $w^* = w_c = (b^2 - 1)$, unstable fixed point representing three-chain critical point.
3. $w^* = \infty$ (zero temperature), representing pure three-chain bound state, comes from the RG flow.

The stable fixed point $w^* = 1$ describes the high temperature fixed point or an absence of the three-body interaction and the unstable fixed point $w_c = b^2 - 1$ describes the critical state produced by a pure three-body interaction.

In case all pairs are in the critical state so far as the two-body interaction is concerned ($y_{ij}^* = b - 1$), the fixed points of w are found to be

$$w_{\pm} = \frac{b^2 \pm \sqrt{4 - 24b + 32b^2 - 12b^3 + b^4}}{2(b-1)^3}. \tag{2.11}$$

In the range $2.303 < b < 8.596$, no real roots are found for w from the three-chain RG relation (Eq. (2.10)) at the critical line $y = y_c$.

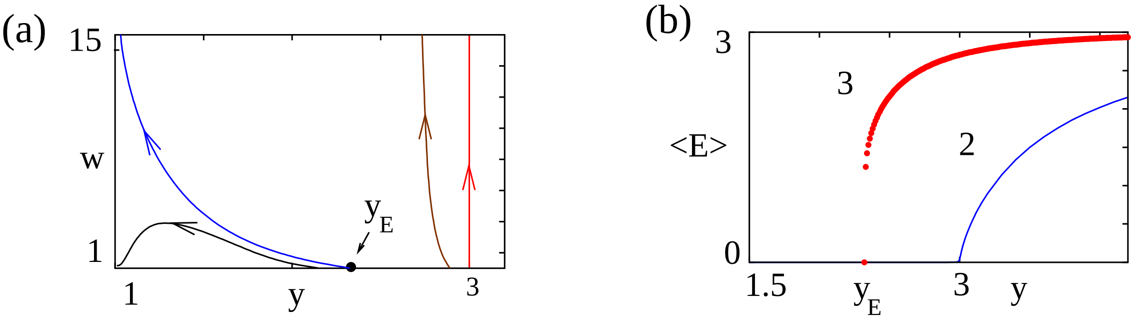

Figure 2.3: (a) RG Flow-diagram in the y-w plane for the symmetric case $y_{12} = y_{23} = y_{13}$, all starting with $w = 1$. Here $b = 4$. The flow of w goes to ∞ if the starting $y > y_E = 2.32402...$, otherwise to 1 (high temperature fixed point). The trajectories with starting $y < y_E$ end at $w = y = 1$. (b) Average energy per monomer *vs* temperature from direct computation (chain length=2^{25}). For two chains (marked 2) the average energy undergoes a continuous transition at $y = y_c$ while the average energy for three chains (marked 3) shows a jump at $y = y_E$. The region from y_E to y_c is the Efimov-like three chain bound state.

Symmetric pair interaction

Here we consider all three pairs identical (either Watson-Crick type or Hoogsteen type). The RG-flow diagram is shown in Fig. 2.3(a) for branching factor $b = 4$. The RG flows are shown in the different regions. The arrows are to denote the direction of RG flows. We considered only $b = 4$ as a representative of the range where there is no real fixed point along the two-chain critical line. Here $y_c = 3$ is the two-chain melting point. The RG flow of w depends on the initial value of y. The renormalization flow takes w to infinity with an initial value $y_{ij} = y_c = b-1$, as shown in Fig. 2.3(a) by the red curve. The three chains then form a bound state at the two-body critical point. For temperatures above the duplex melting, *i. e.*, with initial values $y = y_{12} = y_{23} = y_{31} < b - 1$ the three chains would be in the denatured state if the flow goes to $y = 1,\ w = 1$, but for $y \geq 2.32402$, the flow goes to infinity and reaches $w = \infty$ at $y = 1$. Hence an effective three-chain interaction develops when the pairs are unbound. Below $y < y_c$ the three-chain system is in the high temperature phase— note that, by choice, the flow starts from $w = 1$. Therefore for $b = 4$, the melting of an effective three-chain bound state is at $y = 2.32402...$. The region between $y = y_E$ to $y = y_c$ corresponding to $w = 1$, is for an effective triple stranded bound state when there should not be any duplex bound state. If a separatrix is imagined in the y-w plane between $(1, b^2 - 1)$ and $(y_E, 1)$, then in the region enclosed by this separatrix and the two-chain critical line $y = y_c$, a triplex state would exist eventhough no two are bound. Such a loosely bound state will be called the Efimov DNA.

2.2.2 Efimov DNA: Numerical evidence

A further confirmation of this triplex melting comes from an exact numerical calculation of the average energy by iterating the partition functions and their derivatives for large lattices. In exact iteration method the lattice is built generation by generation so that one may study the behaviour of any quantity of interest as a function of length of the polymers. The direction of iteration towards larger lattices are shown by the right arrows as shown in Fig. 2.1. With the trace over all configurations if C_n, Z_n and Q_n are the $n^{\rm th}$ generation partition functions for single-, double- and triple-chain systems, then these obey the recursion relations [32]

$$\begin{aligned} C_n &= bC_{n-1}^2, && (2.12)\\ Z_n &= b(b-1)C_{n-1}^4 + bZ_{n-1}^2, && (2.13)\\ Q_n &= b(b-1)(b-2)C_{n-1}^6 \\ &\quad + b(b-1)C_{n-1}^2 \sum_{\substack{i,j=1\\ i<j}}^{3} Z(ij)_{n-1}^2 + bQ_{n-1}^2, && (2.14) \end{aligned}$$

where the arguments of Z_{n-1} in Eq. (2.14) refer to the two chains involved. The initial conditions are taken as

$$C_0 = 1, Z_0 = y, Q_0 = y^3.$$

To write down the derivatives of the above partition functions (Eqs. 2.12-2.14) we have considered the symmetric situations, *i. e.*, the equal pair interactions. Therefore we write the average energy and the specific heat as

$$E_n = \frac{\partial \ln \mathrm{Q_n}}{\partial x}, \text{ and } \mathcal{C}_n = \frac{\partial \mathrm{E_n}}{\partial x}, \tag{2.15}$$

where x is the appropriate variable (y or w as the case may be). Though these definitions are different from the actual definitions, proportionality factors are not crucial here.

The recursion relations of the two-chain and the three-chain average energy $(\mathcal{E}_n, E_n)$ and the specific heat $(\breve{C}_n, \mathcal{C}_n)$, derived from the $n^{\rm th}$ generation partition function are as follows.

$$\mathcal{E}_n = 2b\frac{Z_{n-1}^2\mathcal{E}_{n-1}}{Z_n}, \tag{2.16}$$

$$\breve{C}_n = \mathcal{E}_n{}^2 + \frac{\breve{C}_{n-1}\mathcal{E}_n}{\mathcal{E}_{n-1}} - 2\mathcal{E}_n\mathcal{E}_{n-1}, \tag{2.17}$$

$$E_n = 2b\frac{3(b-1)C_{n-1}^2 Z_{n-1}^2\mathcal{E}_{n-1} + Q_{n-1}^2 E_{n-1}}{Q_n}, \tag{2.18}$$

$$\mathcal{C}_n = 2b\frac{3(b-1)C_{n-1}^2 Z_{n-1}^2(\breve{C}_{n-1} - 2E_{n-1}^2) + Q_{n-1}^2(\mathcal{C}_{n-1} - 2E_{n-1}^2)}{Q_n} + E_n^2. \tag{2.19}$$

For given y and w, Eqs. (2.12)-(2.14) give the partition functions for different L_n. The

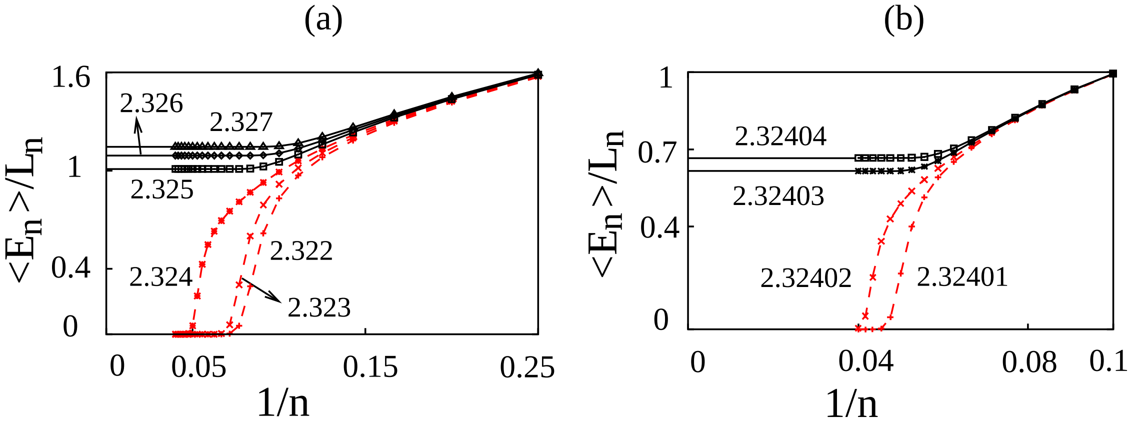

Figure 2.4: Plots of E_n/L_n *vs* $1/n$, E_n being the three-chain average energy, n the generation number. We went upto $n = 25$ for which the length of each polymer is $L_n = 2^{25}$. In (a) we show for $y = 2.322 + n$ x $10^{-3}, n =$0,...,5, while a finer grid result is shown in (b) with $y = 2.32400 + n$ x $10^{-5}, n =$1,...,4. The lines show the extrapolations to $n \to \infty$. The discontinuity at the transition is visible.

two- and the three-chain average energies per monomer are shown in Fig. 2.3(b). With $y \equiv y_{12} = y_{23} = y_{31}$, as in Fig. 2.3(b), the two-chain system melts through a second order transition at $y = y_c$ (energy going continuously to zero) [96, 97] whereas the three-chain system undergoes a first order transition at a temperature $y = y_E < y_c$ (energy showing a discontinuity).

The discontinuity in the three-strand average energy has been shown in Fig. 2.4. Since the length of the polymer at the n^{th} generation is $L_n = 2^n$, the thermodynamic limit of the energy per monomer E_n/L_n can be obtained by extrapolation to $1/n \to 0$. Fig. 2.4(a) shows the extrapolation in the range of $y = 2.323$ to 2.327 which brackets the transition in the range (2.324, 2.325). The discontinuity survives even on a finer scale in Fig. 2.4(b), which gives y_E in the range (2.32402, 2.32403) consistent with the RG result of Fig. 2.3(a). The numerical estimations of the effective three-chain melting temperatures for different b are given in the table below when there is no pure three-chain interaction (*i. e.*, $w = 1$).

b	3	4	5	6
y_E	1.8..	2.32402..	2.77..	3.179..

Table 2.1: The Efimov transition points (y_E's) for different values of b when $w = 1$.

Asymmetric pair interaction

The RG flows can be generalized for asymmetric pair binding energies too. This is the asymmetric case where we have considered $\epsilon_{12} = \epsilon_{23} \neq \epsilon_{31}$. For generalization we may consider all three pairs different (one pair Watson-Crick type and remaining Hoogsteen type). The phase diagram in the plane of y_{13}^{-1} *vs* y_{12}^{-1} with $y_{12} = y_{23}, w = 1$ is shown in Fig. 2.5. For $y_{13}^{-1} = 0$, chains 1 and 3 are bound for ever and therefore chain 2 melts off at $y_{12} = \sqrt{b-1}$. This point is indicated by a star in Fig. 2.5. Within the triangular shaded region bounded by $y_{13}^{-1} = 1/(b-1)$, $y_{12}^{-1} = 1/(b-1)$, and the curved line separating the unbound state, we have a triplex phase without pairing of any two — the desired Efimov effect. In y_{13}^{-1}-y_{12}^{-1} plane the diagonal direction (*i. e.*, $y_{13} = y_{12}$) gives the symmetric case (Fig. 2.3(a)) where all the pair interactions are same.

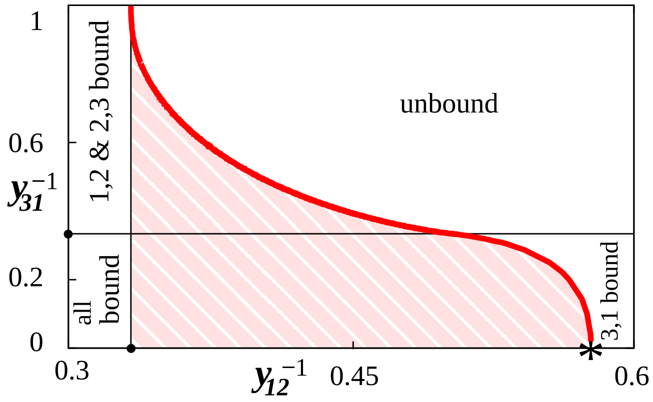

Figure 2.5: Phase Diagram: y_{31}^{-1} *vs* y_{12}^{-1} ($y_{12} = y_{23}$), for $b = 4$. The duplex melting point at $y_c^{\{ij\}} = b - 1$ is indicated by the horizontal and vertical lines. Three chains are bound in the shaded region with the thick curve representing the three-chain bound-unbound transition. Above the horizontal line at $y_{31} = b - 1$ in the shaded region, a triplex state exists even though no two should be bound. The bound states in other regions are as indicated. The star at $y_{12}^{-1} = 1/\sqrt{b-1}$ is the melting of chain 2 and composite 1,3.

2.3 Conclusions

Our emphasis is on the Efimov like state exhibited by the three-chain system at or beyond the two-chain melting, where no two are bound, and the nature of transitions. The RG relations and the exact numerical calculations are used for $d > 2$ to show the possibility of such three-strand DNA bound state at conditions where a duplex DNA would be in the denatured state. This is a biological analog of the nuclear or cold atom Efimov effect. The existence of such a bound state involving two otherwise denatured strands of DNA due to the presence of a third strand, with overall separation much larger than the hydrogen bond length would have important implications in biological processes. Nonetheless, we anticipate new experiments to look for signatures of our proposed Efimov DNA.

3

Efimov DNA and its transitions

In this chapter we study the melting of a three-stranded DNA by using real space renormalization group and exact recursion relations. The prediction of an unusual Efimov-analog three-chain bound state, that appears at the critical melting of a two-chain DNA, is corroborated from the zeros of the partition function. The distribution of the zeros have been studied in detail for various situations. We extend the model to the three-chain repulsive zone. We show that the Efimov DNA can occur even if the three-chain (*i. e.,* three monomer) interaction is repulsive in nature. In higher dimensions, a striking result that emerged in this repulsive zone is a continuous transition from the critical state to the Efimov DNA.

The chapter is organized as follows. In Sec. 3.2, the recursion relations from RG decimation and those for exact iterations are written. The method of finding the zeros of the partition function is discussed and we find the limit point of the zeros to locate the phase transition. Sec. 3.3 contains the results and discussions on the two- and the three-chain system under different situations. In particular we estimate the transition point for Efimov DNA. Sec. 3.4 extends the problem to three chains repulsive interaction. The existence of a transition between the Efimov DNA and the critical repulsive state in higher dimensions is established there.

3.1 Model

Based on the model discussed in Sec. 2.1, in this chapter we have considered the three-chain system on a recursively constructed hierarchical lattice as shown in Fig. 2.1 for symmetric pair interactions. The polymers are assigned attractive potentials $-\epsilon$ and $-\epsilon_{123}$ $(\epsilon, \epsilon_{123} > 0)$ if a single bond is shared by the two and the three polymers, respectively (see Fig. 2.2). Although $\epsilon_{123} = 0$, still this term will be needed for the RG transformation to probe the three-body bound state and is generated by renormalization.

3.2 Method

In this section we summarize the RG transformations and the exact recursion relations for the partition functions. The two ways of handling the problem are just two different ways to look at it. In the RG case, we start from a large lattice and remove short scale fluctuations by renormalizing the parameters, effectively reducing the size of the lattice. In contrast to this idea of thinning out the degrees of freedom, in the second method the lattice is built generation by generation so that one may study the behavior of any quantity of interest as a function of the length of the polymers. This is useful in studying phase transitions because finite size scaling can then be used to explore the nature of the transition.

3.2.1 Renormalization group

By defining the Boltzmann factors,

$$y = \exp(\beta\epsilon), \text{ and } \ w = \exp(\beta\epsilon_{123}), \tag{3.1}$$

the RG transformations of the two-chain and the three-chain Boltzmann factors can be written as (with $y_{12} = y_{23} = y_{31} = y$ from Eqs. (2.9) and (2.10))

$$\begin{aligned} y' &= \frac{(b-1)+y^2}{b}, && (3.2)\\ w' &= \frac{(b-1)(b-2)+3(b-1)y^2+y^6w^2}{b^2y'^3}, && (3.3)\end{aligned}$$

where the primed variables y' and w' on the left hand side represent the renormalized values of the Boltzmann factors.

To discuss the phases and the nature of the transitions, one needs the fixed points for this analysis. These are discussed in Sec. 2.2.1. The correlation lengths for successive generations are related by $\xi' = \frac{\xi}{\lambda}$. This is coupled with the deviation of temperature from the critical point. Thus, once the fixed points are known, transition exponents can be calculated from the RG relations by linear expansion around the critical points. The two-chain melting is critical with the diverging length scale with exponents

$$\nu = \frac{\ln\lambda}{\ln\left(\left.\frac{dy'}{dy}\right|_{y\to y_c}\right)} \tag{3.4}$$

and the specific heat exponent

$$\alpha = 2-\nu. \tag{3.5}$$

It is known from the Eq. (2.11) that at the two-chain critical point $y_c = b-1$, no real roots are found from the three-chain RG relation, Eq. (3.3), within the range $2.303 < b < 8.596$. These complex roots lead to a limit cycle behaviour, which is intimately related to the Efimov effect (see appendix B).

3.2.2 Exact recursion relations

With the trace over all configurations the n^{th} generation partition functions for single- (C_n), double- (Z_n), and triple- (Q_n) chain systems obey the recursion relations

$$\begin{aligned} C_n &= bC_{n-1}^2, && (3.6)\\ Z_n &= b(b-1)C_{n-1}^4 + bZ_{n-1}^2, && (3.7)\\ Q_n &= b(b-1)(b-2)C_{n-1}^6 \\ &\quad +3b(b-1)C_{n-1}^2 Z_{n-1}^2 + bQ_{n-1}^2. && (3.8) \end{aligned}$$

The initial conditions are taken as

$$C_0 = 1, \quad Z_0 = y, \quad Q_0 = y^3 w. \tag{3.9}$$

The two- and the three- chain average energy and the specific heat are given by Eqs. (2.16)-(2.19) [see Eq. (2.15)].

3.2.3 Zeros of the partition functions Z_n and Q_n

If we take $w = 1$, *i. e.*, no three-body interaction, then the partition functions are polynomials in y. In general, Z_n is a polynomial in y of order L_n while Q_n is a multinomial in y and w. These partition functions are then completely described by the zeros which are necessarily complex. A phase transition is signaled by a real limit point of the zeros. However, the rapid growth of the order of the polynomials makes it difficult to implement this program directly. A different representation is used to get the zeros [54].

For $n = 1$, the two-chain partition function is written as

$$Z_1 = b(b-1)C_0^4 + bZ_0^2. \tag{3.10}$$

With the initial conditions $C_0 = 1, Z_0 = y$, Eq. (3.10) becomes

$$Z_1 = b(b-1) + by^2, \tag{3.11}$$

which, by using Eq. (3.2), can be written as

$$Z_1(y) = b^2 y' = b^2 Z_0(y'). \tag{3.12}$$

In a similar way, Z_2, for $n = 2$, can be written as

$$Z_2 = b^5(b-1) + bZ_1^2, \tag{3.13}$$

and, by using the two-chain RG relation, Eq. (3.13) becomes

$$Z_2(y) = b^5 y' = b^4 Z_1(y'). \tag{3.14}$$

Thus by using the RG transformations of y and w, the recursion relations from Eqs. (3.6)-(3.8) can be reduced exactly to the forms

$$\begin{aligned} Z_n(y) &= b^{L_n} Z_{n-1}(y'), & (3.15)\\ Q_n(y,w) &= (b^{L_n})^{3/2} Q_{n-1}(y',w'), & (3.16)\end{aligned}$$

with y', w' given by Eqs. (3.2) and (3.3). These relations can be verified by direct substitution and, if necessary, by the method of induction as discussed above.

Since the zeros determine a polynomial completely, the two-chain partition functions can be written as

$$\begin{aligned} Z_n(y) &= b^{L_n-1}\prod_{l=1}^{L_n}(y-q_l), & (3.17)\\ \text{and}\quad Z_{n-1}(y) &= b^{L_{n-1}-1}\prod_{j=1}^{L_{n-1}}(y-\tilde{q}_j), & (3.18)\end{aligned}$$

where the q_l's and $\tilde{q}_j$'s are the zeros of the partition functions $Z_n(y)$ and $Z_{n-1}(y)$, respectively. These zeros appear in complex-conjugate pairs. With the substitution of Eqs. (3.17) and (3.18), Eq. (3.15) becomes

$$b^{L_n-1}\prod_{l=1}^{L_n}(y-q_l) = b^{L_n} b^{L_{n-1}-1}\prod_{j=1}^{L_{n-1}}(y'-\tilde{q}_j). \tag{3.19}$$

Then the use of Eq. (3.2), the relation between y' and y, gives two roots from each factor on the right hand side, so that the q_l's are the solutions of

$$\frac{(b-1)+y^2}{b} = \tilde{q}_j, \tag{3.20}$$

i. e.,

$$q = \pm\sqrt{b\tilde{q}_j - (b-1)}. \tag{3.21}$$

The subscript of q is omitted. This clearly shows that if we know the 2^{n-1} zeros $\tilde{q}_j$ of $Z_{n-1}(y)$, we will be able to know the 2^n zeros q_l of $Z_n(y)$. One may start with the roots of Z_1 and generate successively the roots of each generation, by just solving a quadratic equation.

Instead of generating all the roots, a random generation is more easily implementable. With an initial value y_0 chosen randomly from the two roots of Z_1, the new roots are determined by Eq. (3.21). If one of them is chosen at random and substituted as $\tilde{q}_j$, the roots for the next generation can be found. Thus, after the nth iteration, the set obtained is basically the zeros in the complex y-plane. These roots are nothing but the zeros of the partition function found from different sizes of the lattice, which in this problem would be equivalent to different lengths of polymers. The zeros quickly converge and as $n \to \infty$ we look for the limit point on the real axis. Apart from that, the distribution in the complex y-plane itself is of interest. This method has been generalized for the three-chain system.

3.3 Behavior of zeros: two- and three-chain systems

3.3.1 Two-chain system: $b = 4$

For different branching factors, fractal-like structures are obtained from the zeros of the partition functions of the two- and the three-chain systems. We considered only $b = 4$ as a representative of the range where there is no real fixed point along the two-chain critical line. For $b = 4$ the structure shown in Fig. 3.1(a) is obtained in the complex y plane from the exact recursion relation Eq. (3.15). Exact solutions are possible only up to the

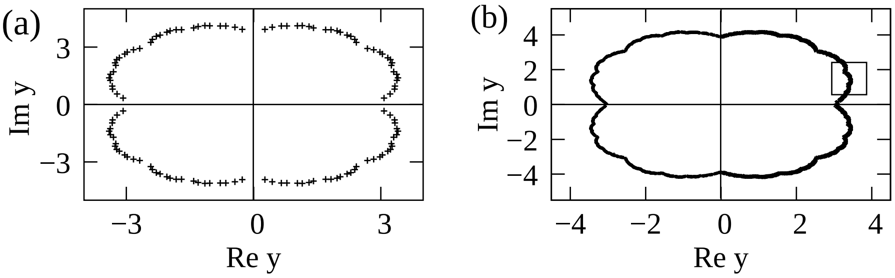

Figure 3.1: Plot of zeros of $Z_n(y)$ in the complex y-plane for $b = 4$ from (a) the exact recursion relation for $n = 6$, and (b) the RG relation. The closest point to the Re(y) axis approaches $y_c = 3$, the two-chain melting point in the limit $n \to \infty$, the unstable fixed point of Eq. (3.2). The selected region shown by a box is zoomed in Fig. 3.2(a).

$n = 6$ generation because of computational hardware limitations. This is insufficient, as the thermodynamic limit ($n \to \infty$) is needed to observe a phase transition. Finding zeros at random from the RG relations [Eqs. (3.2) and (3.3)] overcomes such difficulties and hence large lengths can be reached. The zeros obtained from Eq. (3.20) give the fractal-like structure shown in Fig. 3.1(b). The accessed zero nearest to the real axis approaches the two-chain transition point $y_c = 3$ for large n. Apart from the limit point, the distribution of the zeros in the complex y plane is also non-trivial.

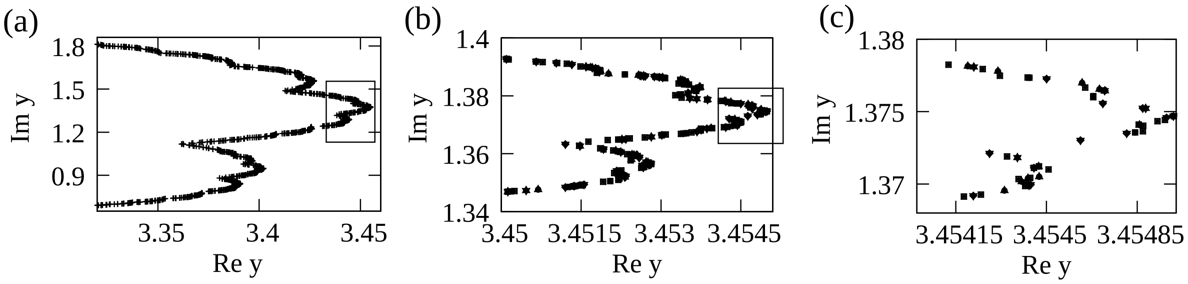

Figure 3.2: Zeros of $Z_n(y)$: The inner rectangular box is zoomed successively. A self-similar structure becomes apparent. Note that the zeros are known with high accuracy.

The first feature to note is that the zeros do not seem to lie on a smooth differentiable curve. A zoomed picture of a small cross section of the structure for the two-chain system [from Fig. 3.1(b)] is shown in Fig. 3.2(a). Further the selected regions have been zoomed successively and are shown in Figs. 3.2(b) and 3.2(c). The self-similarity of the structure is visible. This is an indication of the fractal nature of the distribution. Further analysis required for a quantitative description is not done here.

These fractal like structures obtained above are nothing but the separatrices of the set of RG flows in the complex plane to the appropriate stable fixed points. These separatrices for iterations of any function in the complex plane are known as the Julia set (see appendix A). The sets are obtained after an infinite number of iterations of a recursive formula by identifying the points that do not flow to the stable fixed points. Our method of finding the zeros by using the RG relations is in fact equivalent to an inverse iteration method, which is more efficient in producing such structures.

In Fig. 3.3(a) the RG flows are shown in the complex y plane for a two-chain system. The dotted line (red curve) shows the flow towards the stable fixed point $y = 1$, *i. e.*, the high temperature region, when we start with a value from the inner region of the fractal-like structure. On the other hand, a point from the outskirts of the line of zeros flows to the stable fixed point $y = \infty$, which is the bound state with zero temperature. The critical point, being an unstable fixed point, does not actually belong to the set but, as discussed, is a limit point — in a sense a boundary of the set.

The second feature to note is the 3-like shape near the real-axis limit point. It is not arbitrary. The angle at the limit point in the complex plane is related to the specific heat exponent by [98]

$$\tan(\phi\nu) = -\tan(\pi\alpha) + \frac{A_-}{A_+}\csc(\pi\alpha), \tag{3.22}$$

where ϕ is the angle between the tangent of zeros at the limit point, and the real axis of y, and $A_\pm$ are the amplitudes of the specific heat on the low and the high y side of the transition. Just like the exponents, A_-/A_+ is a universal number for a universality class of transition. For the two-chain problem, we know that $A_-/A_+ \to \infty$ as $A_+ = 0$. Therefore the angle ϕ is given by

$$\phi = \frac{\pi}{2\nu}. \tag{3.23}$$

The zeros obtained by the successive iterations of the one close to the real axis are shown in Fig. 3.3(b) by the triangles. They approach the real axis in a linear fashion with an angle ϕ, given by the straight line

$$\text{Im } z = (\text{Re } z - c)\tan\frac{\pi}{2\nu}, \tag{3.24}$$

in the generic complex z plane with ν from Eq. (3.4). Here c represents the limit point of the zeros on the real axis. The zeros occur in complex conjugate pairs. Therefore if we take the mirror image of the distribution of zeros about the real axis in Fig. 3.3(b), the beak of the 3-like shape can be obtained.

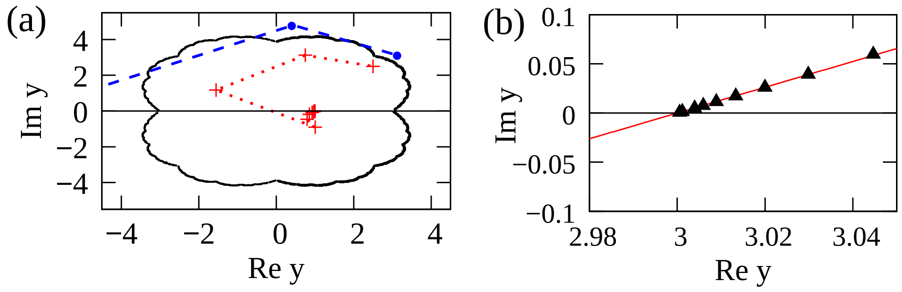

Figure 3.3: (a) Plot of zeros of $Z_n(y)$ in the complex y plane. Two types of RG flow are shown. The dotted red curve starts from a point of the inner region and flows to $y = 1$. The dashed blue curve starts from a point of the outer region and flows to ∞. (b) The triangles are the zeros and approach the limit point $y_c = 3$ at large n. The solid red line, given by Eq. (3.24), makes an angle ϕ with the real axis with ν of Eq. (3.4) and $c = y_c$.

3.3.2 Three-chain system: $b = 4$

We have calculated the zeros of $Q_n(1, w)$ for a three-chain system with a pure three-chain interaction. By considering $y = 1$ in Eq. (3.3), we get

$$w' = \frac{(b^2 - 1) + w^2}{b^2}. \tag{3.25}$$

The zeros come from the equation

$$q_l = \pm\sqrt{b^2 \tilde{q}_j - (b^2 - 1)},$$

where the q_l's and $\tilde{q}_j$'s are the zeros of $Q_n(1, w)$ and $Q_{n-1}(1, w)$, respectively. The distribution of zeros is the Julia set which has a fractal-like structure shown in Figs. 3.4(a), 3.4(c), and 3.4(d). By choosing the zero near to the limit point w_c, the nature of the distribution can be determined, as shown in Fig. 3.4(b) by the straight line given by Eq. (3.24) with ν of Eq. (3.29) and $c = w_c$.

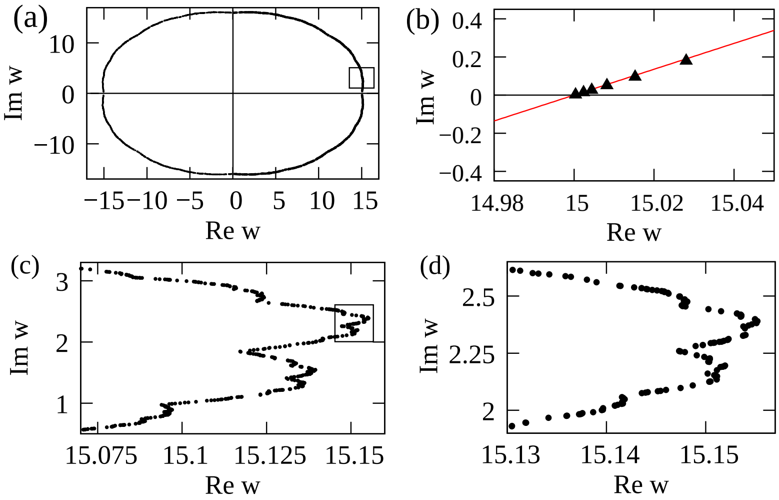

Figure 3.4: (a) Plot of the zeros of $Q_n(1, w)$ in the complex w-plane for $b = 4$. The closest point to the real axis approaches $w_c = 15$ for large n. There is self-similarity in the distribution of zeros. (b) The triangles are the zeros. The solid red line given by Eq. (3.24) passes through them with ν of Eq. (3.29) and $c = w_c$. (c), (d) The inner rectangular box [from (a)] is zoomed successively.

3.3.3 Efimov DNA: $b = 4$

The idea is to show the Efimov transition point of DNA by finding the limit point of zeros on the real y axis. Although we consider $w = 1$, the effective three-chain interaction gets generated by renormalization. As a result the zeros found from Eqs. (3.6)-(3.8) seem to pinch the Re(y) axis at a point where no pair of chains is bound. The exact solutions are shown in Fig. 3.5(a) for $n = 6$. On a finer scale the zeros are shown in Fig. 3.5(b). For such small lattices the limit point is not accessible, hence an extrapolation scheme may be used. The zeros nearest to the Re(y) axis, obtained in different generations ($n = 2, ..., 6$) are shown in Fig. 3.5(c) by black dots. A straight line nicely fits these zeros and is shown by the solid red curve.

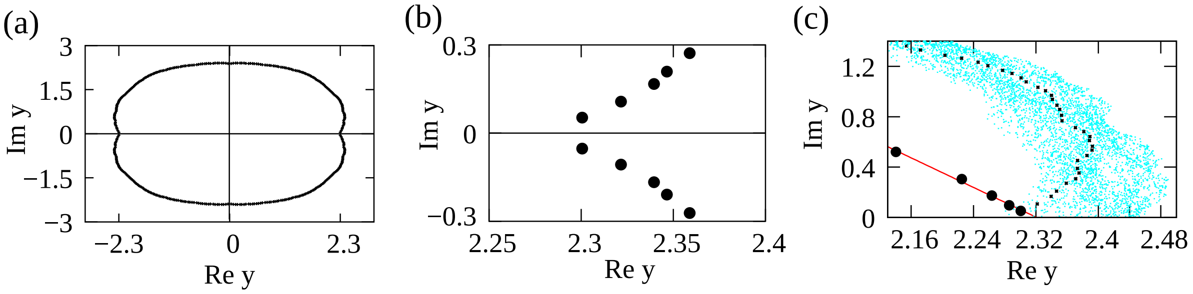

Figure 3.5: Plot of zeros in the complex y-plane for $b = 4$. (a) Zeros of $Q_n(y, 1)$, when $n = 6$, (b) a finer scale of (a) near the real axis, and (c) combined plot of zeros. The bigger black circles are the zeros closest to the real axis (*i. e.*, with smallest imaginary part) obtained from $Q_n(y, 1)$ for $n = 2, ..., 6$ and the solid (red) straight line is a fit to these. The “Milky Way"-like region shows the distribution of zeros from Eq. (3.26) on which we superpose the positive quadrant of (a) shown by the small black dots.

The straight line intersects the real axis at $y = 2.321$. This value is the large n extrapolation and can be taken as an estimate of the Efimov transition. We may compare this extrapolated value with the previous RG-based estimate of $y_E = 2.32402$. Finding the zeros for the two-chain system is easier than for the three-chain system. Since the three-chain equation holds both the variables y and w, finding zeros from the three-chain RG relation is tantamount to generating the full relation for Q_n. This is because one needs to keep w at all the intermediate values of n and then, at the the desired value of n, w is to be set to 1. One sees the difficulty of the Efimov physics even though $w = 1$. It is tempting to simplify the recursion relation at the cost of some approximation. We set $w = w' = 1$ to get a renormalized y' that describes the three-chain system. Such a relation follows from Eq. (3.3), as

$$y'^3 = \frac{(b-1)(b-2) + 3(b-1)y^2 + y^6}{b^2}. \tag{3.26}$$

The zeros obtained from Eq. (3.26) spread out in a “Milky Way” over a region in the complex plane of y. The spread makes it difficult to make an estimate of the real-axis limit point, but one may use the width to put a bound on the Efimov transition point [see Fig. 3.5(c)].

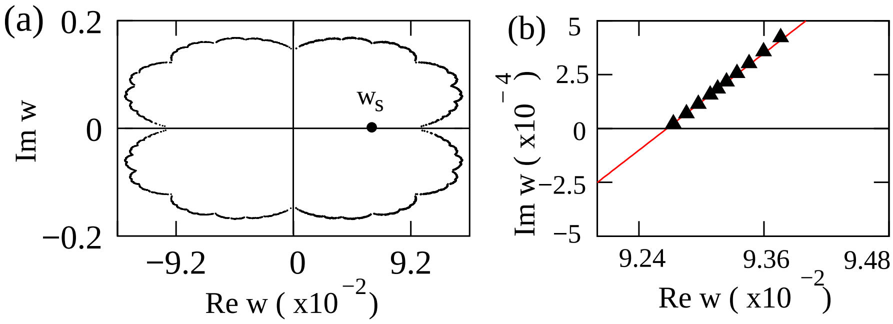

Figure 3.6: (a) Zeros of $Q_n(y_c, w)$ in the complex w plane for $b = 9$. The stable fixed point $w = w_s$ is shown by a black circle. (b) The solid red line is given by Eq. (3.24) and passes through the zeros shown by the triangles, with ν from Eq. (3.30) and $c = w_E$.

3.3.4 Efimov DNA at $y_c = b - 1$: $b = 9$

A study along the critical threshold of the two-chain melting is quite interesting. No real fixed point for w exists for Eq. (3.3) when b is in the range $2.303 \leq b \leq 8.596$ along the $y = y_c$ line. For $y = y_c$, the single parameter RG relation is

$$w' = \frac{(b-2) + 3(b-1)^2 + (b-1)^5 w^2}{b^2(b-1)^2}. \tag{3.27}$$

The two fixed points for this case are given by Eq. (2.11). For $b = 9$, these are

$$w = w_s = 0.0655347... \quad \text{(stable)}, \tag{3.28a}$$

$$w = w_E = 0.0926684... \quad \text{(unstable)}. \tag{3.28b}$$

The unstable fixed point, as the phase transition point, determines the limit point of the zeros of the partition function on the real axis. Hence it can be predicted that at the two-chain melting point, by tuning w, a transition occurs at $w = w_E$, from the Efimov DNA to the critical state of polymer pairs. Figure 3.6(a) shows the distribution of zeros of $Q_n(y_c, w)$ in the complex w plane. The set of these zeros is a Julia set, separating the flows to the stable fixed points. The stable fixed point in the inner region of the set is given by Eq. (3.28a). The zeros near the real axis approach $w = w_E$ linearly, following Eq. (3.24) with $c = w_E$ and ν of Eq. (3.30) as shown in Fig. 3.6(b). A detailed discussion is given in the next section.

3.4 Efimov DNA: RG flow and numerical evidence

To explore the robustness of the Efimov effect, we now include a three-chain repulsive interaction along with the pairwise attractive one. The three-chain interaction is attrac-

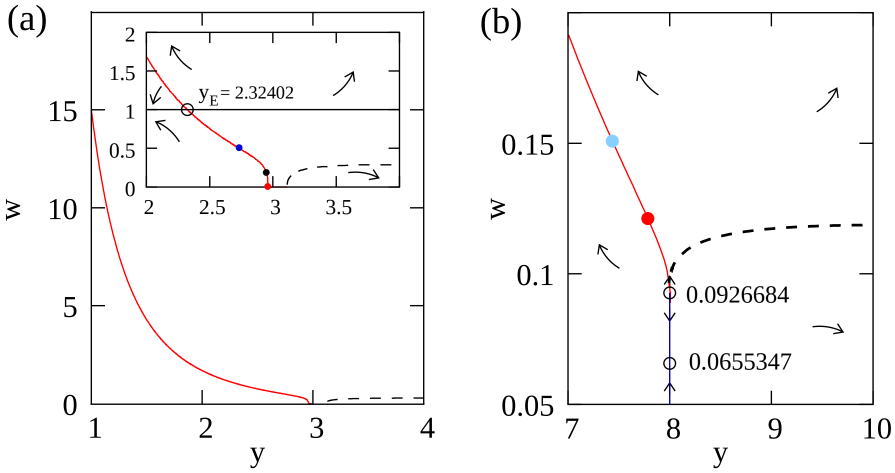

Figure 3.7: RG phase diagram in the y-w plane. The arrows are to show the flow of the renormalized parameter schematically. (a) For $b = 4$. The solid red curve and the dashed curve represent the separatrices, where w flows to two different fixed points on either side of the separatrix. The zoomed area near $y_c = 3$ is shown in the inset. For $w = 1$, $y_E = 2.32402$ is the Efimov DNA transition point. The filled circles are the Efimov transition points for $w = 0.5$, and $w = 0.2$, $w = 0$, respectively, obtained from Fig. 3.8(a). (b) For $b = 9$. Along $y_c = 8$, there are two real fixed points given by Eq. (3.28a). The solid (red) and dashed lines are the separatrices. The filled circles are the Efimov transition points for $w = 0.15$ and $w = 0.12$, respectively, obtained from Fig. 3.8(b).

tive when $w > 1$ and repulsive for $0 \leq w < 1$. For $w = 0$, representing the hard core three-chain repulsive interaction, three chains can never be on the same bond in this model.

A. $b = 4$

For $b = 4$ the RG phase diagram is shown in Fig. 3.7(a). The solid red line is the separatrix connecting the pure three-chain transition point $(1, w_c)$ to an Efimov transition point for $w = 0$. Each point on the solid line represents an Efimov transition point. In other words keeping w fixed, by changing y, we can see a melting of a loosely bound Efimov DNA with no pairwise binding. The region enclosed between this separatrix (solid red line) and the $y_c = 3$ line is the Efimov region and (y, w) flows to $(1, \infty)$. Below the solid red line is the high temperature zone of denatured DNA, where RG flows are to $(1, 1)$. The region to the right of the $y_c = 3$ line is the two-chain bound state. The area below the dashed curve, where the RG flow takes w to zero when two-chain pairs are strongly bound, represents a different state where one finds a three-chain bound state but with no three-chain contact. The dashed line is then a crossover line. It remains to be seen if under some conditions this crossover line becomes a true phase transition line.

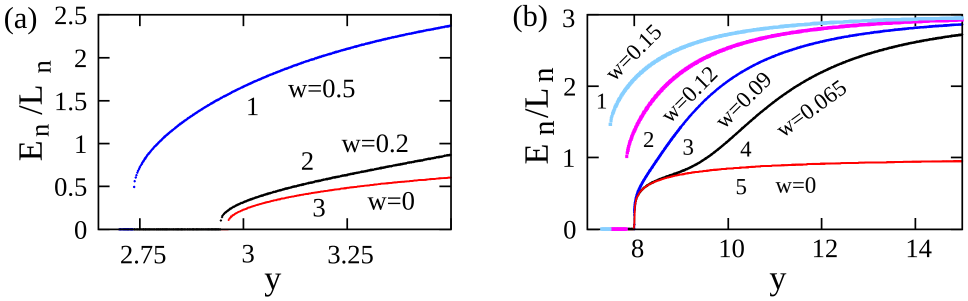

Figure 3.8: The three-chain average energy per monomer with y from direct computation. (a) For $b = 4$, the average energy curves (marked 1, 2, and 3) with the fixed values $w = 0.5$, $w = 0.2$, and $w = 0$ show first order transitions. (b) For $b = 9$, the average energy curves (marked 1 and 2) with the fixed values $w = 0.15$ and $w = 0.12$ show first-order transitions. Curves (marked 3, 4, and 5) with the constant values $w = 0.09$, $w = 0.065$, and $w = 0$ show a continuous transition at $y_c = 8$.

B. $b = 9$, $y_c = b - 1$

The RG phase diagram is shown in Fig. 3.7(b) for $b = 9$. In the diagram two separatrices (the solid red line and the dashed line) meet at an unstable fixed point. The two fixed points $w = w_s$ and $w = w_E$ are shown in Fig. 3.7(b). The presence of any unstable fixed point reflects a continuous transition along the two-chain critical line. Hence we can say that by tuning the three-chain repulsive interaction parameter or temperature in the repulsive zone a transition can be induced in the Efimov DNA at the critical threshold of duplex binding. The transition is from the Efimov state to the critical state of pairs dominated by the three-chain repulsion. The Efimov region is now restricted by a separatrix connecting the two unstable fixed points $(1, w_c)$ and (y_c, w_E) and the critical line $y_c = b - 1$.

On the critical line at both the fixed points $w = w_s$ and $w = w_E$, y is a relevant variable (unstable in the y direction). But y does not couple to w in the RG equation [Eq. (3.2)]. The melting for $w < w_E$ would be similar to the pure two-chain melting described by Eqs. (3.4) and (3.5). In the y-w plane, (y_c, w_E) is a multicritical point where the line of first-order transitions goes over to a line of critical points.

C. Data collapse

We now provide numerical evidence for the above RG-based inferences. Exact numerical calculations of the average energy and the specific heat are done by iterating the partition functions and their higher derivatives for lattices of various sizes for different fixed values of w. Figure 3.8(a) for $b = 4$ shows that at $w = 0.5$, $w = 0.2$, and $w = 0$, there are first-order transitions. The transition points estimated from the point of discontinuity are shown by the filled circles in Fig. 3.7(a). They are on the separatrix and are the

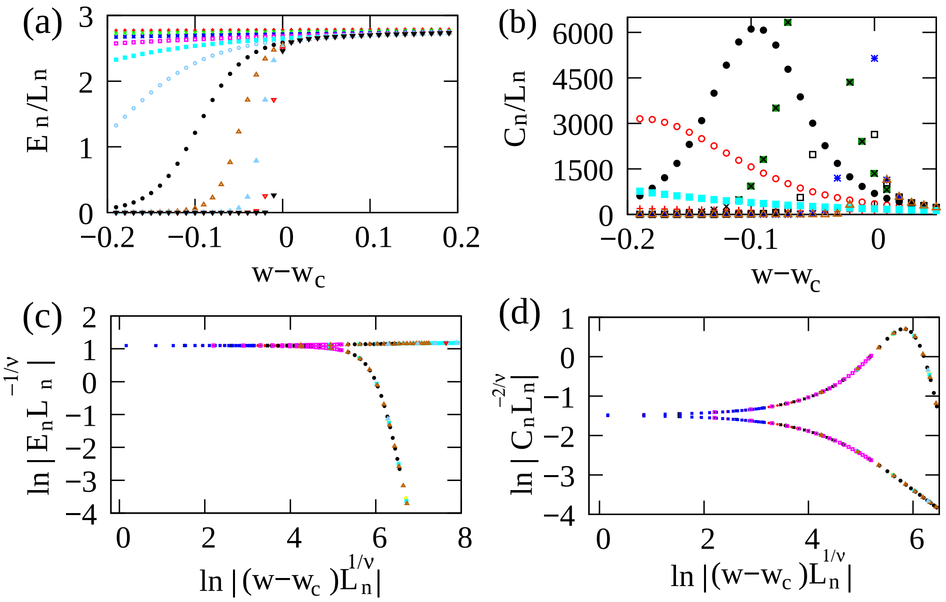

Figure 3.9: For $b = 4$. (a) The three-chain average energy per monomer versus the corresponding Boltzmann factor for chain length up to 2^{26} when $y = 1$. The average energy shows a continuous transition at $w = w_c$. (b) The three-chain specific heat ($\mathcal{C}_n$) per monomer with the corresponding Boltzmann factor. (c) Data collapse of energy. (d) Data collapse of specific heat.

Efimov transition points for the corresponding values of w.

The energy curves in Fig. 3.8(b) for $b = 9$ with $w = 0.15$ and $w = 0.12$, show first-order transitions. These transition points are shown by the filled circles in Fig. 3.7(b). In contrast, the energy curves (marked 3, 4, and 5) show continuous transitions for $w = 0.09$, $w = 0.065$, and $w = 0$, respectively at $y_c = 8$. This is consistent with the RG prediction of Fig. 3.7(b).

The energy and the specific heat curves are shown in Figs. 3.9(a) and 3.9(b) for $b = 9$, $y = 1$ and in Figs. 3.10(a) and 3.10(b) for $b = 9$, $y = y_c = b - 1$. Also the corresponding finite size scaling is shown in Figs. 3.9(c) and 3.9(d) for $b = 9$, $y = 1$ and in Figs. 3.10(c) and 3.10(d) for $b = 9$, $y = y_c = b - 1$. The finite size scaling behavior of different thermodynamic quantities is described by the length scale exponents. In analogy with Eq. (3.4), the exponents to describe the three-chain transition for $y = 1$ and $y = y_c$ at appropriate critical points are given by

$$\nu = \frac{\ln 2}{\ln \frac{2(b^2-1)}{b^2}}, \tag{3.29}$$

$$\nu = \frac{\ln 2}{\ln \left(\frac{\partial w'}{\partial w}\Big|_{\substack{y_c=b-1 \\ w\to w_E}} \right)}. \tag{3.30}$$

Around a critical point one should see a finite size scaling. Therefore the three-chain

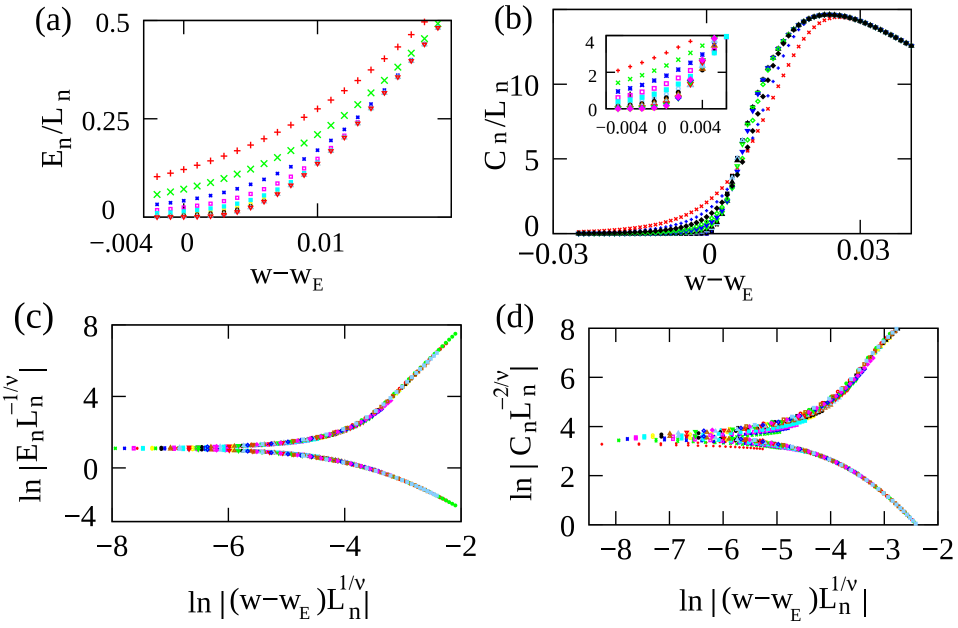

Figure 3.10: For $b = 9$. (a) The three-chain average energy per monomer versus the corresponding Boltzmann factor for chain length up to 2^{26} when $y_c = b - 1$. The average energy shows a continuous transition at $w = w_E$. (b) The three-chain specific heat ($\mathcal{C}_n$) per monomer with the corresponding Boltzmann factor. The length dependence is shown in the inset. (c) Data collapse of energy. (d) Data collapse of specific heat.

average energy and the specific heat obeying the finite size scaling can be written in the forms

$$E \sim L^{1/\nu} f(L^{1/\nu}|w - w^*|), \tag{3.31}$$

$$\mathcal{C} \sim L^{2/\nu} f(L^{1/\nu}|w - w^*|), \tag{3.32}$$

with appropriate ν and w^*. In Figs. 3.9(c) and 3.9(d) we see that the average energy and the specific heat scale as $E_n L_n^{-1/\nu}$ and $\mathcal{C}_n L_n^{-2/\nu}$, respectively, when plotted versus $|(w - w^*)|L_n^{1/\nu}$ with the ν of Eq. (3.29) and $w^* = w_c$ for $y = 1$, all the data collapse onto a single curve for different lengths of polymers, where $n = 6, 7, ..., 26$.

Figures 3.10(c) and 3.10(d) show similar plots for the critical line ($y_c = b - 1$) with ν of Eq. (3.30) and $w^* = w_E$. Since the specific heat diverges with increasing length, data collapse is good for the case $y = 1$. The data collapse for the case $y_c = b - 1$ is not so good due to a smoother behavior of the specific heat at the critical point. These establish the weak criticality at $w = w_E$.

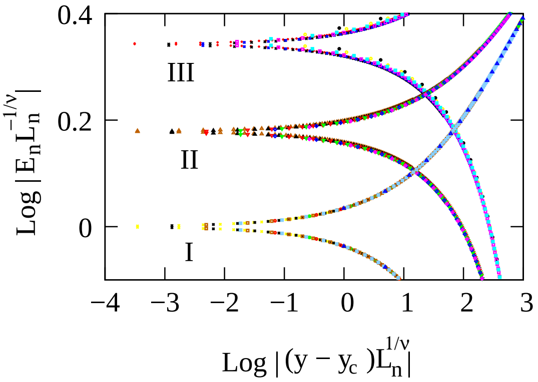

Figure 3.11: For b=9. Data collapse of the average energy of the two-chain system (set I) and the three-chain system (set II and III) with $w = 0.07$ and $w = w_E$, respectively.

D. Data collapse($w \leq w_E$)

The finite size scaling of the two- and the three-chain average energy are shown in Fig. 3.11 for $b = 9$. The average energy obeying the finite size scaling is of the form,

$$E \sim L^{1/\nu} f(L^{1/\nu}|y - y_c|), \tag{3.33}$$

with appropriate ν. The two- and the three-chain average energy scaled with $E_n {L_n}^{-1/\nu}$ are plotted with $|(y - y_c)|L_n^{1/\nu}$. All the data seem to give good datacollapse as shown in Fig. 3.11 by sets I, II and III for different lengths of polymers, where $n = 10, 11, ..., 16$. The set I is the datacollapse for the two-chain system [32] with the exponent of Eq. (3.4) and the set II shows the datacollapse for the three-chain system for $w = 0.07 < w_E$ with the same exponent like the two-chain case, given by Eq. (3.4). The set III shows the datacollapse for the three-chain system for $w = w_E$ with the two-chain length scale exponent of Eq. (3.4) with 1% error bar. Theses show that the three-chain melting for $w \leq w_E$ is similar to the pure two-chain melting. The differences between the two sets of collapse are due to corrections from the w term. The two-chain system does not have the three-chain interaction term. So for $w \leq w_E$, the transitions are controlled by the two-chain length scale exponent.

3.5 Conclusion

To summarize, the RG relations and exact recursion relations are used to study the three-chain system on a diamond hierarchical lattice. Our emphasis is on the Efimov-like state exhibited by the three-chain system at or beyond the two-chain melting, where no two chains are bound, and the nature of the transitions. Fractal-like structures are obtained for the zeros of the partition functions. These zeros, when they pinch the real axis, determine the phase transition points. We find that all the transition points obtained from RG flows, are in good agreement with the zeros of the partition function on the real axis. The Efimov transition point thus found strengthens the prediction of Efimov-like phenomena for the three-chain system. We have shown that the Efimov effect is exhibited by a three-chain system even if there is a repulsive three-chain interaction. A transition can be induced in higher dimensions from the Efimov state to the three-chain critical repulsive state at the melting of duplex DNA. The transition to this three-chain critical repulsive state is continuous and obeys a finite size scaling law with exponents obtained from the RG. In the (y, w) phase diagram, (y_c, w_E) is a multicritical point.

Although the model studied in this paper is simplistic, mainly to get exact results, still the denaturation transition induced by bubble formation accompanied by diverging length scales is the generic scenario for more realistic polymeric models. The qualitative picture is therefore expected to be valid for those models too. We await experimental evidence for the existence of the Efimov DNA or the Efimov transition. Again, the existence of such a state remains a challenge for molecular dynamics and Monte Carlo simulations.

4

Efimov effect: Polymers on the Sierpinski gasket

In the previous two chapters three polymers on a hierarchical lattice of dimension $d > 2$ have been studied and the Efimov-DNA was predicted. In this chapter we show that the Efimov effect occurs even in lower dimensions if some specific interactions are considered among the polymers. Here we study the melting of the three-stranded DNA on a Sierpinski Gasket and show that a transition can be induced if extra weight factors are given to the fork opening and closing. We study different models in detail and obtain a new state, to be called a mixed state.

This chapter is organized as follows. In Sec. 4.1, we define our model on a Sierpinski gasket. In Sec. 4.2 and Sec. 4.3 the polymers with the crossing and the non-crossing conditions are defined. The exact recursion relations of the partition functions are written and the methods of calculation are discussed. Three different models for the three-chain case are studied. A summary is given in a table in Sec. 4.5.

4.1 Model

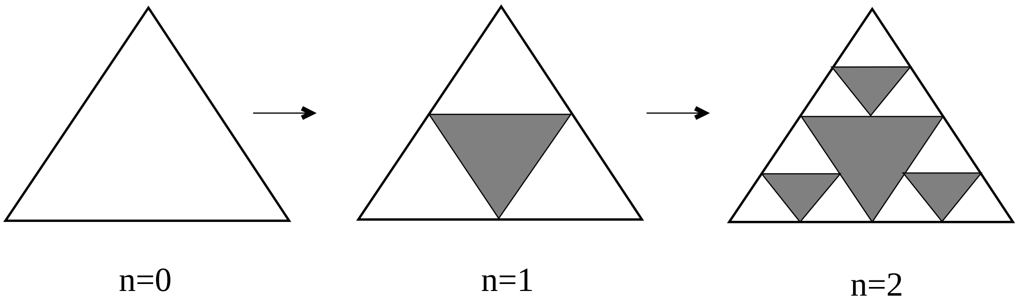

Figure 4.1: Recursive construction of the Sierpinski Gasket. Polymer walk is not allowed in the shaded triangles.

The Sierpinski gasket is a fractal lattice obtained after an infinite iteration from a single equilateral triangular lattice. This particular lattice is drawn in the two dimensional ($d = 2$) plane. Taking out the middle piece of a triangular shape yields three smaller triangles. Thus the fractal lattice is formed recursively after an infinite number of iteration. See Fig. 4.1. The dimension is calculated for an infinite lattice, and it is

$$d = \frac{\ln N_{n\to\infty}}{\ln L_{n\to\infty}} = \frac{\ln 3}{\ln 2} \approx 1.58, \tag{4.1}$$

where N_n is the the number of the surviving triangles and L_n is the length of unit step or the number of bonds of the lattice from bottom to top along the any one side of the lattice at the n^{th} generation.

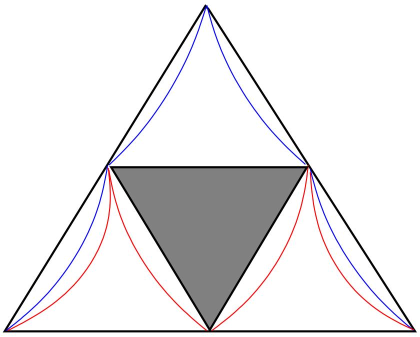

Figure 4.2: Two chains along the non horizontal bonds. Two possible walks are shown (b_n and g_n type from Fig. 4.3).

On the Sierpinski Gasket, polymers are restricted to occupy only the non-horizontal bonds as shown in Fig. 4.2. Following weights are assigned to the polymers:

- Fugacity z for each bond,
- Boltzmann factor $y_{ij} = e^{\beta\epsilon_{ij}}$, when a single bond is shared by the two polymers and $y_{ijk} = e^{\beta\epsilon_{ijk}}$ when a single bond is shared by the three polymers.
- σ_{ij} for the two-chain and σ_{ijk} for the three-chain bubble opening or closure.

The weight of a walk of a single chain of length N is z^N, where N is the number of bonds. The tradition is to consider z as an extra variable, but we will set it to 1, as is discussed below. Here $\sigma = 1$ implies no weight is given for bubble opening or closure, and $\sigma = 0$ implies no bubble formation, *i. e.*, a model without any bubble.

To study the melting of DNA on a fractal lattice, we need to define the partition functions for the two- and the three-chain systems as shown in Fig. 4.3. We choose $z = 1$ to be in the canonical ensemble. The standard way to study the polymers on a fractal lattice is to find out the fixed point of z by an RG procedure as proposed by D. Dhar [44]. This corresponds to the Grand canonical ensemble, where the fixed point of z gives the free energy. We know that the choice of ensemble does not matter, as long as we work with the large length of the polymer. In our approach we calculate the free energies, look for the most favorable one and obtain the phase diagram directly from the free energies. Since all the polymers are of same length ($\to \infty$) and traverse the whole lattice, we may set $z = 1$.

Different possible polymer configurations are shown in Fig. 4.3. The partition functions $a_n, b_n, c_n, d_n, e_n, f_n, g_n, h_n, i_n$ are defined at the n^{th} generation and the recursion relations are written for successive generations. If the n^{th} partition function is known, the $(n+1)^{\text{th}}$ generation partition function can be derived from the recursion relations. Based on the idea of the various phases, the total partition functions for the two- and the three-chain system in the fixed length ensemble are written as

$$\begin{aligned} Z_{\text{tot}} &= b_{n+1}^2 + d_{n+1}, \qquad (4.2)\\ Q_{\text{tot}} &= f_{n+1} + b_{n+1}^3 + n_c d_{n+1} b_{n+1}, \qquad (4.3) \end{aligned}$$

in terms of the subpartition functions b_{n+1}, d_{n+1} and f_{n+1}. Here n_c is the number of configuration of $d_{n+1}b_{n+1}$ state. It is 3 when chains can cross each other and 2 when they can not. Two chain bubble is given by b_{n+1}^2, d_{n+1} is the two-chain bound state. Similarly for the three-chain system, three-chain bubble is given by b_{n+1}^3, f_{n+1} is the three-chain bound state. The last term in Eq. (4.3) describes the mixed state a state when one is free with the other two forming a duplex. If the free chain has no entropy, the state would be defined by $d_{n+1}^{3/2}$, but as we argue below this is an unphysical state.

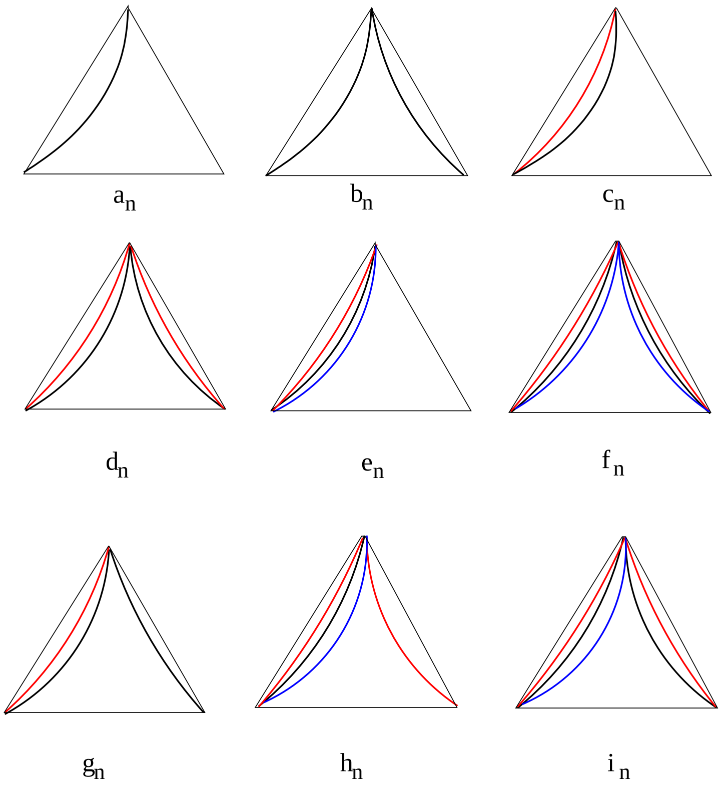

Figure 4.3: Generating functions for two and three strands.

4.2 Two strands DNA

4.2.1 With crossing

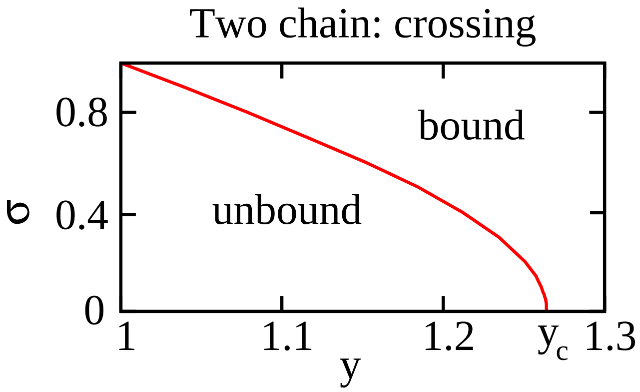

Figure 4.4: Two-chain phase diagram for σ *vs* y. Polymers can cross each other. The two-chain melting is at $y_c(0) = 1.264$ for $\sigma = 0$.

We consider the two-chain system. The walks can cross each other. Here y is the weight at the bond for sharing the same bond by the two polymers. The two-chain bubble opening or closure is associated with the weight σ at the vertex. The partition functions for the two-strand problem for the $(n+1)^{\text{th}}$ generation are given by,

$$a_{n+1} = a_n^2, \tag{4.4a}$$

$$b_{n+1} = b_n^2 + a_n^2 b_n, \tag{4.4b}$$

$$c_{n+1} = c_n^2, \tag{4.4c}$$

$$d_{n+1} = d_n^2 + 2g_n^2 b_n + c_n^2 d_n, \tag{4.4d}$$

$$g_{n+1} = a_n g_n (b_n + c_n). \tag{4.4e}$$

The initial conditions are taken as

$$a_0 = 1,\ b_0 = 1,\ c_0 = y,\ d_0 = y^2,\ g_0 = y\sigma. \tag{4.5}$$

We look at the divergence or convergence of the ratio

$$r_1 = \frac{d_{n+1}}{b_{n+1}^2} \tag{4.6}$$

for given σ and y. By this ratio r_1, the two-chain bound state free energy is compared with the free energy when the two strands are in the denatured state. By looking at the convergence and the divergence of r_1 we obtain the phase diagram in the y-σ plane as shown in Fig. 4.4. The transition is from the unbound to the bound state of the two-stranded DNA at $y = y_c(\sigma)$. The nature of the transition line near $\sigma = 0$ has been studied in small intervals of σ, but many points are omitted from the graph. For $\sigma = 0$, the two-chain melting is at $y_c(0) = 1.264$. The melting transition is first order where the two-chain average energy per bond shows a discontinuity. The issue of discontinuity is discussed in Sec. 4.4.

4.2.2 No crossing

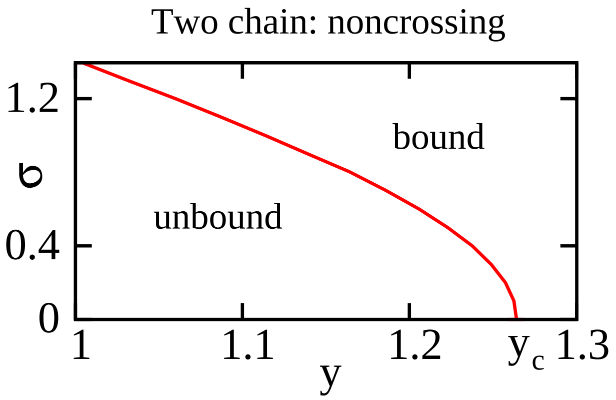

Figure 4.5: Two-chain phase diagram for σ *vs* y. Non-crossing walk. The two-chain melting is at $y_c(0) = 1.264$ for $\sigma = 0$.

If the crossing between the two strands DNA is not allowed, the recursion relations are same as the crossing case except for d_n, which in this case is

$$d_{n+1} = d_n^2 + g_n^2 b_n + c_n^2 d_n. \tag{4.7}$$

The initial conditions are still given by Eq. (4.5). A similar comparison method [Eq. (4.6)] is used here as in the two-chain crossing case. We obtain the phase diagram in the y-σ plane as shown in Fig. 4.5. For $\sigma = 0$ the two-chain melting is at $y_c(0) = 1.264$, which is the same as in the crossing case. There is a difference between the crossing and the non-crossing melting curve for $\sigma \neq 0$.

4.3 Three strands

When we consider the three-chain system, several cases are possible. With crossing and non-crossing conditions and interacting and non-interacting pairs we classify different models. There are many possible varieties but we will discuss only three of them, TS1, TS2 and TS3. With different considerations of interactions the models are the following:

1. Model TS1: This is the non-crossing case and favours two-chain bubble opening or closure. No contact energy between chains 1 and 3.

2. Model TS2: This is the crossing case with the three-chain repulsion and favours two-chain bubble opening or closure.

3. Model TS3: This is the crossing case with the three-chain repulsion and weight for the two- and the three-chain bubble opening or closure.

4.3.1 Model TS1: Non-crossing

In this case walks can not cross each other. We assign a weight Boltzmann factor y for each interaction between chains 1 and 2, and 2 and 3 *i. e.*, $y_{12} = y_{23} = y$, but no interaction between chains 1 and 3, *i. e.*, $y_{31} = 1$. The weight σ is assigned for each bubble opening between all pairs, *i. e.*, $\sigma_{12} = \sigma_{23} = \sigma_{31} = \sigma$. When all chains are together we consider a weight y^2 and such a situation can also be described if we take $y_{12} = y_{23} = y_{31} = y$ and $y_{ijk} = 1/y$. If $y > 1$, y_{ijk} is repulsive in nature.

The recursion relations for the partition functions for this model are given by

$$a_{n+1} = a_n^2, \tag{4.8a}$$
$$b_{n+1} = b_n^2 + a_n^2 b_n, \tag{4.8b}$$
$$c_{n+1} = c_n^2, \tag{4.8c}$$
$$d_{n+1} = d_n^2 + g_n^2 b_n + c_n^2 d_n, \tag{4.8d}$$
$$e_{n+1} = e_n^2, \tag{4.8e}$$
$$f_{n+1} = f_n^2 + e_n^2 f_n + h_n^2 d_n + i_n^2 b_n, \tag{4.8f}$$
$$g_{n+1} = a_n g_n (b_n + c_n), \tag{4.8g}$$
$$h_{n+1} = h_n (a_n e_n + b_n c_n), \tag{4.8h}$$
$$i_{n+1} = i_n (c_n e_n + d_n a_n) + g_n^2 h_n, \tag{4.8i}$$

and the initial conditions are

$$a_0 = 1,\ b_0 = 1,\ c_0 = y,\ d_0 = y^2,\ e_0 = y^2,\ f_0 = y^4,\ g_0 = y\sigma,\ h_0 = y^2\sigma^2,\ i_0 = y^3\sigma^2. \tag{4.9}$$

We look at the divergence or convergence of the ratios

$$r_2 = \frac{f_{n+1}}{b^3_{n+1}}, \tag{4.10}$$

$$r_3 = \frac{f_{n+1}}{b_{n+1}d_{n+1}}, \tag{4.11}$$

$$r_4 = \frac{f_{n+1}}{d^{3/2}_{n+1}} \tag{4.12}$$

for given σ and y. The idea behind choosing the above three ratios is to compare the three-chain free energy with the free energy when three chains are free [r_2 in Eq. (4.10)], when one chain remains free while the other two forming a duplex [r_3 in Eq. (4.11)] and when all are paired but no three-chain contact [r_4 in Eq. (4.12)]. By looking at the divergence or convergence of the ratios r_2, r_3, and r_4 for different y, σ and comparing these values with the two-chain melting curve, different phases are obtained. We make a comparison between r_3 and r_4. If we have a phase where the strands are pairwise bound but no three-chain contact, we can have two possibilities. This mixed phase could be described either by the free energy $\ln d^{3/2}_{n+1}$ or by the free energy $\ln b_{n+1}d_{n+1}$. If there are pair interactions among all chains and walks can cross each other then for each pair we get d_{n+1}. If the free chain has limited configurations, we can write the free energy contribution as $\ln{(d^3_{n+1})}^{1/2} = \ln d^{3/2}_{n+1}$ leaving aside other factors. Evenif 1 and 3 do not interact and walks do not cross each other, the possible phase has the free energy contribution $\ln(d^2_{n+1})^{3/4} = \ln d^{3/2}_{n+1}$. The other possibility is to have a situation where the strands are pairwise bound but no three-chain contact but the free chain has full entropy, then the free energy is $\ln b_{n+1}d_{n+1}$. Fig. 4.6(a), 4.6(b) are the configurations of the mixed phase for the crossing and the noncrossing cases.

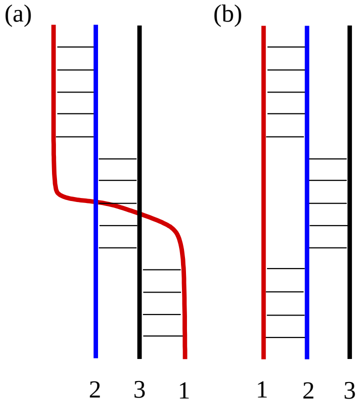

Figure 4.6: Schematic diagram of a mixed phase of three polymers of two possible configurations. At each monomer position, two are bound but the third monomer is free along the length of the chains. (a) Polymer chains can cross each other. (b) Polymer chains can not cross each other and no interaction between chains 1 and 3.

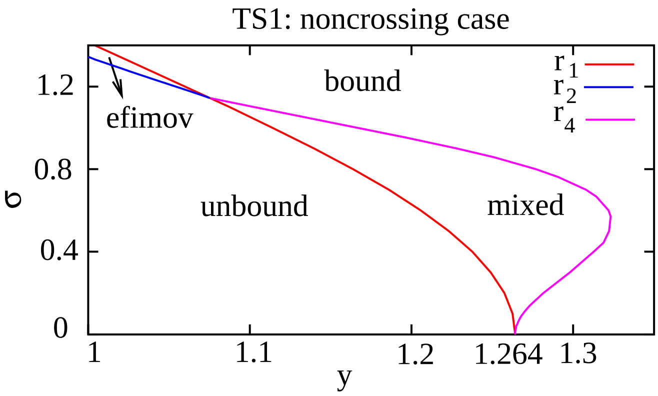

Figure 4.7: Three-chain phase diagram in the y-σ plane for the model TS1. The bound, unbound, the Efimov and the mixed states are shown. The red curve is the two-chain melting curve and is valid for the three-chain case in the region $y > 1.07526$ but not in the region $y < 1.07526$. The Efimov and the mixed both states appear in this case for appropriate σ and y.

Fig. 4.7 shows the phase diagram if $d_{n+1}^{3/2}$ describes the mixed phase while Fig. 4.8 would be phase diagram if the mixed phase is described by $\ln b_{n+1} d_{n+1}$. In both cases, we obtain two different phases, an Efimov phase and a mixed phase. However the Efimov phase is not a distinct phase. It is just an effect on three chains, where no two are bound but three are bound. On the other hand, in a mixed phase, the strands are pair-wise bound but no three-chain contact. In Fig. 4.7, within the range $y = 1$ to $y < 1.07526$ for $\sigma > 1.14458$ the Efimov region is obtained and the region is enclosed between the line for r_2 and the two-chain melting curve. The mixed phase is enclosed between the line

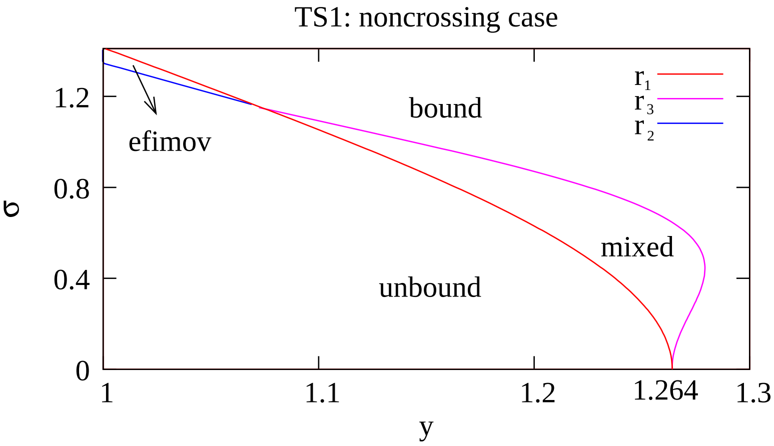

Figure 4.8: Three-chain phase diagram in the y-σ plane for the model TS1. This is the correct phase diagram. The bound, unbound, the Efimov and the mixed states are shown. The red curve is the two-chain melting curve and is valid for the three-chain case in the region $y > 1.07526$ but not in the region $y < 1.07526$. The Efimov and the mixed both states appear in this case for appropriate σ and y.

for r_4 and the two-chain melting curve for $y > 1.07526$ and $\sigma < 1.14458$. Based on the physical intuition we believe, Fig. 4.8 is the correct phase diagram.

4.3.2 Model TS2: With crossing

We now extend the study to a slightly different model with the following characteristics:

- Walks can cross each other.
- $y_{12} = y_{23} = y_{31} = y,\ y_{123} = \frac{1}{y}$.
- $\sigma_{12} = \sigma_{23} = \sigma_{31} = \sigma,\ \sigma_{123} = 1$.

In this model all chains are having equal pair interaction. There is a three-chain repulsive interaction. A weight is given for the two-chain bubble opening or closure. The recursion relations for the $(n+1)^{\text{th}}$ generation partition functions are given by

$$a_{n+1} = a_n^2, \tag{4.13a}$$
$$b_{n+1} = b_n^2 + a_n^2 b_n, \tag{4.13b}$$
$$c_{n+1} = c_n^2, \tag{4.13c}$$
$$d_{n+1} = d_n^2 + 2g_n^2 b_n + c_n^2 d_n, \tag{4.13d}$$
$$e_{n+1} = e_n^2 \tag{4.13e}$$
$$f_{n+1} = f_n^2 + e_n^2 f_n + 3h_n^2 d_n + 3i_n^2 b_n, \tag{4.13f}$$
$$g_{n+1} = a_n g_n (b_n + c_n), \tag{4.13g}$$
$$h_{n+1} = h_n (a_n e_n + b_n c_n), \tag{4.13h}$$
$$i_{n+1} = i_n (c_n e_n + d_n a_n) + 2g_n^2 h_n, \tag{4.13i}$$

with the initial conditions

$$a_0 = 1,\ b_0 = 1,\ c_0 = y,\ d_0 = y^2,\ e_0 = y^2,\ f_0 = y^4,\ g_0 = y\sigma,\ h_0 = y^2\sigma^2,\ i_0 = y^3\sigma^2. \tag{4.14}$$

Following the same procedure of comparison of free energies, the phase diagram is obtained in the y-σ plane, as shown in Figs. 4.9, and 4.10. Here also we believe Fig. 4.10 is the correct phase diagram.

With the given initial conditions this model exhibits the mixed phase. One sees two transitions: At low temperature we have a three-chain bound state that goes into the mixed state (blue line in Fig. 4.10) and the mixed state melts into free chains (red line in Fig. 4.10).

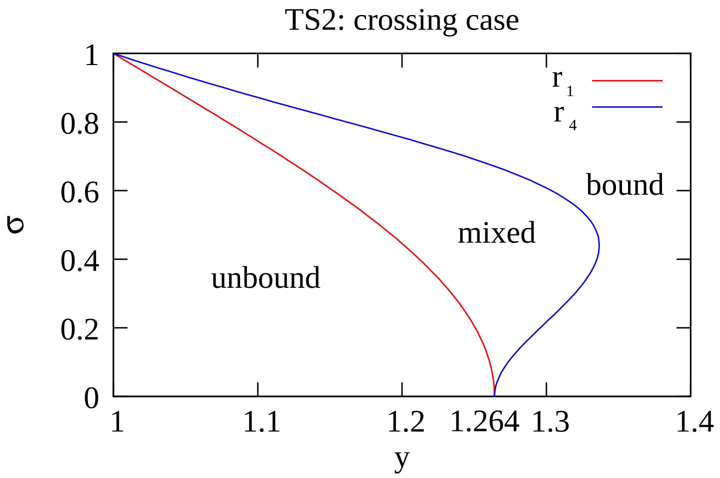

Figure 4.9: Three-chain phase diagram in the y-σ plane for model TS2. The unbound, the bound and the mixed phases are shown. The red curve is the two-chain melting curve which presents in the three-chain case also. There is no Efimov DNA here.

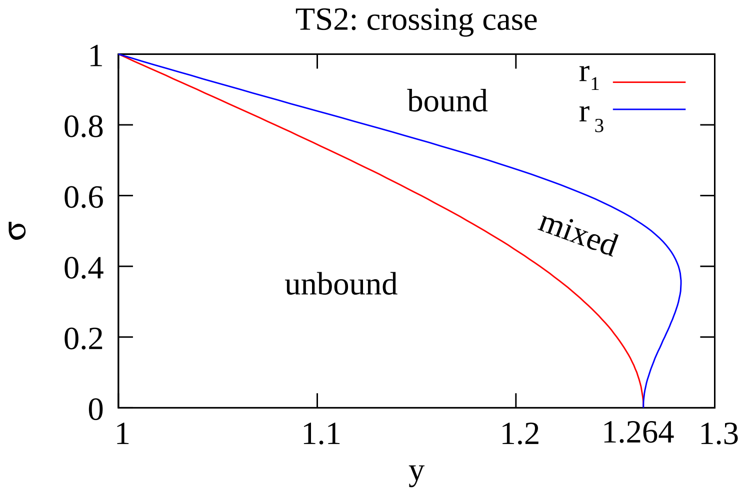

Figure 4.10: Three-chain phase diagram in the y-σ plane for model TS2. This is the correct phase diagram. The unbound, the bound and the mixed phases are shown. The red curve is the two-chain melting curve which presents in the three-chain case also. There is no Efimov DNA here.

4.3.3 Model TS3: With crossing

We consider a different generalization that favours three-chain bubbles

- Walks can cross each other.
- $y_{12} = y_{23} = y_{31} = y,\ y_{123} = \frac{1}{y}$.
- $\sigma_{12} = \sigma_{23} = \sigma_{31} = \sigma,\ \sigma_{123} = \frac{1}{\sigma}$.

Here $\sigma < 1$. Therefore $\sigma_{123} > 1$. Two-chain bubbles are suppresses by σ but σ_{123} favours three-chain bubbles. Here three chains have repulsive interaction. A weight is given for the two and the three chains bubble opening or closure. However the recursion relations are same as for TS2 given by Eqs. (4.13a)-(4.13i). The initial conditions are

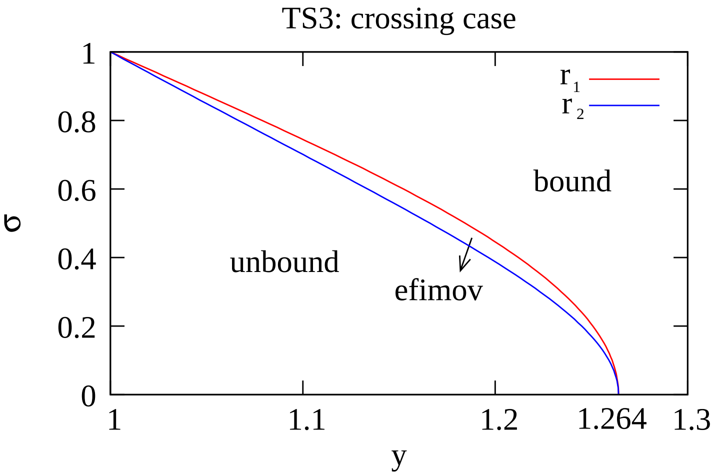

Figure 4.11: Three-chain phase diagram in the y-σ plane for model TS3. The unbound, the bound and the Efimov states are shown. The red curve is the two-chain melting curve, which is not present in the three-chain case.

$$a_0 = 1,\ b_0 = 1,\ c_0 = y,\ d_0 = y^2,\ e_0 = y^2,\ f_0 = y^4,\ g_0 = y\sigma,\ h_0 = y^2\sigma,\ i_0 = y^3\sigma. \quad (4.15)$$

The three-chain interaction is repulsive in this case. Following the same procedure of comparison of free energies, the Efimov state is obtained and is shown in Fig. 4.11.

4.4 Energy diagram

The exact numerical calculations of the total average energy are done by taking the derivatives of the total partition function. The total average energy of the two-chain system (E_{tot}) and the three-chain system ($\mathcal{E}_{\text{tot}}$) [using Eq. (4.2) and Eq. (4.3)] are given by [see Eq. (2.15)]

$$E_{\rm tot} = \frac{d_n E_{d_n}}{Z_{tot}}, \tag{4.16}$$

$$\mathcal{E}_{\rm tot} = \frac{f_n E_{f_n} + n_c b_n d_n E_{d_n}}{Q_{\rm tot}}. \tag{4.17}$$

The three-chain average energy per bond is shown for model TS1 in Fig. 4.12. For noncrossing TS1 model $n_c = 2$. Fig. 4.12(a) is for $\sigma = 1.25$. The three-chain average energy (marked as 1) is compared to the two-chain average energy (marked as 2). This shows the nonzero three-chain average energy, eventhough the duplex average energy is zero. This is the Efimov-DNA, observed in Chap. 2 for $d > 2$. Thus we conclude that, for appropriate values of y and σ, the Efimov effect is induced for $d < 2$.

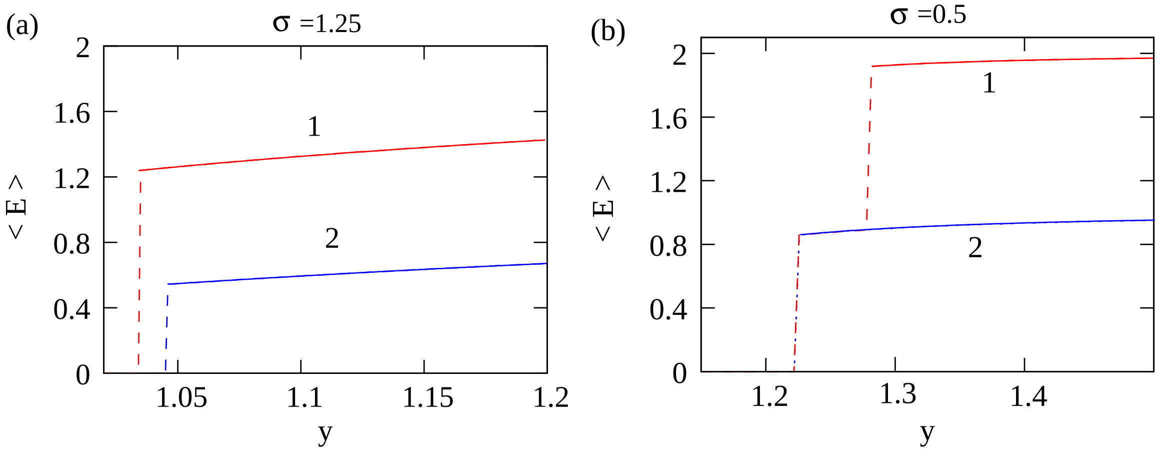

Figure 4.12: Model TS1. Plot of the average energy per bond with y. Dotted lines are to show the discontinuity in the energy curves. (a)For $\sigma = 1.25$. The three-chain average energy (marked as 1) is compared to the two-chain average energy (marked as 2). (b) For $\sigma = 0.5$. The three-chain average energy (marked as 1) is compared to two-chain average energy (marked as 2). For both cases the three- and the two-chain average energy approaches the magnitude 2 and 1 with y respectively.

Fig. 4.12(b) is for $\sigma = 0.5$. The three-chain average energy (marked as 1) is compared to the two-chain average energy (marked as 2). The transition from the unbound to the mixed state is at the same temperature as the two-chain case, *i. e.*, at $y_c(\sigma)$. The transition from the mixed state to the bound state occurs for $y > y_c(\sigma)$ (lower temperature).

The average energy curve in Fig. 4.12(a) marked as 1 shows only one jump, where as in Fig. 4.12(b) the average energy curve marked as 1 shows two jumps. In the later case the two transitions are from the unbound to the mixed state and from the mixed to the two-chain bound state. So it is predicted that the Efimov state is a crossover, not a separate phase. The transition from the unbound to the two-chain bound sate is first order. So is the transition from the mixed state (denoted by bd) to a three-chain bound state (described by f).

4.5 Remarks

All the models and results are given below for easy reference. Model TS2 shows the mixed state, model TS3 shows an Efimov like state. But for model TS1 we get both of the states though in different regimes of σ and y. If we compare models TS2 and TS3 where three-chain interaction is repulsive in nature ($y_{123} > 1$), there is a bias in TS3 for three chain bubble opening or closure. This biasing seems to favor the Efimov effect in TS3. For $\sigma = 0$ the models are like the Y-fork model, which show a first order transition. All the models come out to be same for $\sigma = 0$ and $y_c(0) = 1.264...$ denotes the melting for the two- and the three-chain systems.

Model: TS1 Non-crossing	Model: TS2 Crossing	Model: TS3 Crossing
$y_{12} = y_{23} = y,\ \sigma_{ij} = \sigma$ $y_{31} = 1,\ \sigma_{123} = 1$	$y_{ij} = y,\ \sigma_{ij} = \sigma$ $y_{123} = 1/y,\ \sigma_{123} = 1$	$y_{ij} = y,\ \sigma_{ij} = \sigma$ $y_{123} = 1/y,\ \sigma_{123} = 1/\sigma$
Efimov, Mixed	Mixed	Efimov

Table 4.1: The results obtained from the three-chain models with the initial conditions are shown. The new phases obtained are also flashed in this table.

4.6 Conclusion

In this chapter we have shown that, when an extra weight σ in the favour of the two- and the three-chain bubble opening and closure is introduced, the phase transition occurs even in $d < 2$. Here we have obtained the Efimov-DNA, a loosely three-chain bound state where no two are bound. This observation is same as discussed in the previous two chapters (Chap. 2 and Chap. 3). In addition we have obtained a new state, to be called a mixed state, where locally any two are bound keeping the third-strand always free but in a global view no one is completely free.

The limiting model for $\sigma = 0$ is the Y-fork type which shows a first order transition without any bubbles. No Efimov or mixed state are possible in this case. In fact the transitions for $\sigma > 0$ in these models are also first order and we have observed the intermediate phase (mixed phase) for $y > y_c(\sigma)$ and the Efimov state for $y < y_c(\sigma)$. The intermediate phase evolves as a separate phase but the Efimov state is a crossover.

5

Dynamic phase transition in the conversion of B-DNA to Z-DNA

In this chapter we study the conformational conversion of B-DNA to Z-DNA using wave-front propagation and obtain the dynamic phase diagram. The dynamic phase diagram is obtained for the stability of the front separating B and Z. The instability in this front results in two split fronts moving with different velocities. This shows that, depending on the system parameters a denatured state also may develop dynamically eventhough it is thermodynamically forbidden. This resolves the current controversies on the transition mechanism of the B-DNA to Z-DNA.

This chapter is organized as follows. The conformational transition of B-DNA to Z-DNA is studied using wave-front propagation. We discuss the wave front propagation in Sec. 5.1 with a suitable example. Our proposed thermodynamic model is introduced in Sec. 5.2. The dynamic phase diagram is discussed by numerical and perturbative approach in Sec. 5.3. Conclusions are drawn on the B-Z transition mechanism in Sec. 5.4.

The two main competing hypotheses for the B to Z transition mechanism are on the foyer to motivate us to study the B-Z transition mechanisms with a thermodynamic model. With the purpose of investigating the transition procedure, we consider a coarse-grained thermodynamic model and restrict the geometry to one-dimension only. We maintain the boundaries of the long chain in the two states so that the new structure develops from one side. In such a problem, the dynamics of the transition produces a steady state with uniformly moving front or fronts. An investigation of various types of fronts would clarify the dynamic generation of any thermodynamically forbidden state. With that ambition we study the transition from the B-DNA to the Z-DNA by using the theory of wave-front propagation. In the next section we review the wave front propagation method with an example of two coexisting states.

5.1 Wave front propagation

In this section the wave front propagation is discussed very briefly. Front propagation phenomena arises from the reaction diffusion equation [99, 100]. An interface develops between two distinct phases (one is stable and another is unstable). A driving force tends to favor the stable state among the different distinct phases. As a result the interface starts moving. The moving interface is actually characterized as the traveling wave front when one phase invades the other. Front propagation is widely used in the study of many biological events such as epidemic dynamics, population dynamics, pulse propagation in nerves or other growth dynamics. To study the helicase activity on DNA, a simple coarse grain model was proposed by Bhattacharjee [101]. By the study of wave front propagation he proposed that the Y-fork is an interface whose propagation is the basic step for the replication procedure and replication mechanism. We also encounter propagating front in spreading of flames, chemical reactions and in any dynamic system. If the dynamics is governed by a nonlinear diffusion equation the quantity of interest would be to measure the rate of convergence of velocity or relaxation of velocity and how the interface of a wavefront propagates into an unstable state. For a wide range of initial conditions the velocity of such a front approaches a marginal value. In asymptotic limit the velocity of the traveling wave is uniform and the shape of the wave front remains unchanged.

Let us consider the Landau free energy such that, its minimization describes two homogeneous states given by $\phi = 0$ and $\phi = 1$. The order parameter $\phi(z,t)$ is the diffusive field in one dimension with z (space) and t (time), two independent variables. The equation governing the propagation is of the form

$$\frac{\partial \phi}{\partial t} = D\frac{\partial^2 \phi}{\partial z^2} + f(\phi), \tag{5.1}$$

where D is the diffusion coefficient and $f(\phi)$ is the thermodynamic force, derived from the Ginzburg-Landau free energy

$$\mathcal{H}(\phi) = \int dz \left[\frac{D}{2}\left(\frac{\partial \phi}{\partial z}\right)^2 + F(\phi)\right], \tag{5.2}$$

where $F(\phi) = -\int f(\phi)d\phi$ is the Landau free energy, and $\phi(-\infty,\ t) = 1$, $\phi(\infty,\ t) = 0$ as the boundary conditions. The traveling wave solution satisfying Eq. (5.1) is given by

$$\phi(z,t) = U(\tau), \quad \text{where} \quad \tau = z - vt. \tag{5.3}$$

In Eq. (5.1), $f(\phi)$ acts as a “force” on the interface, as a result of which the induced interface between the two states suffers an instability. The traveling front moves with velocity v, which is to be determined.

In contrast to the non-linear diffusion equation the simple diffusion equation does not lead to any velocity and can be verified very easily. If we substitute Eq. (5.3) in Eq. (5.1) with $f(\phi) = 0$, the solution comes out to be

$$U(\tau) = A + B \exp^{\frac{-v}{D}\tau},$$

where A, B are the integration constants. Since U has to be bounded for all z, B must be zero as the exponential becomes unbound for $\tau \rightarrow -\infty$. Therefore $U(\tau) = A$, a constant can not be a wave solution. Hence simple diffusion can not have traveling wave solution. Dimensional analysis is a simpler way to justify the above argument. The velocity, determined by the dimensional analysis is $[v] = \frac{[z]}{[t]} \sim \sqrt{\frac{D}{t-t_i}}$. This shows that at any $t = t_i$, v is infinity. Therefore the diffusion equation does not have a well defined velocity.

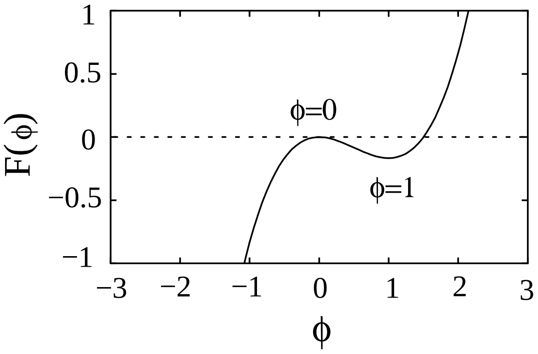

Figure 5.1: The Landau function $F(\phi)$ as a function ϕ. $\phi = 1$ is the stable state and $\phi = 0$ represents the unstable state.

Due to the time dependency, the diffusion equation can not be reduced to a thermodynamic problem. But the nonequilibrium process is driven by the underlying equilibrium Landau function. If the force term involves the stable phase at $\phi = 1$ and the unstable phase at $\phi = 0$, then

$$f(\phi) = k\phi(1 - \phi), \tag{5.4}$$

where k is a constant and the Landau free energy is

$$F(\phi) = -k(\frac{1}{2}\phi^2 - \frac{1}{3}\phi^3). \tag{5.5}$$

The nonlinear diffusion equation

$$\frac{\partial \phi}{\partial t} = k\phi(1 - \phi) + D\frac{\partial^2 \phi}{\partial z^2}, \tag{5.6}$$

with the boundary conditions

$$\phi(-\infty,\ t) = 1, \quad \phi(\infty,\ t) = 0, \ \text{ for all } \ t, \tag{5.7}$$

is known as the *Fisher-Kolmogorov* (F-K) equation [99]. Here $k > 0$ and $D > 0$. The positivity of D ensures the stability of the system. The nontrivial dynamics emerges from the competition between the diffusivity and the non-linearity of the force term. As a result, the stable state invades the unstable one.

Rescaling the F-K equation by $\tilde{t} = kt$ and $\tilde{z} = z\sqrt{\frac{k}{D}}$ we get

$$\frac{\partial \phi}{\partial \tilde{t}} = \phi(1-\phi) + \frac{\partial^2 \phi}{\partial \tilde{z}^2}. \tag{5.8}$$

For notational simplicity we avoid the tilde sign. Therefore Eq. (5.8) becomes

$$\frac{\partial \phi}{\partial t} = \phi(1-\phi) + \frac{\partial^2 \phi}{\partial z^2}. \tag{5.9}$$

In the spatially homogeneous situation the steady states are $\phi = 1$ and $\phi = 0$ which are respectively homogeneous stable and unstable states. We restrict ourselves in the region $0 \leq \phi \leq 1$. Note that Eq. (5.9) is invariant under reflection of x. With the uniformly translating front solution,

$$\phi(z,t) = U(\tau), \quad \text{where} \ \ \tau = z - vt, \tag{5.10}$$

Eq. (5.9) is written as

$$U'' + vU' + U(1-U) = 0, \tag{5.11}$$

where the prime denotes the derivative of U with respect to τ. The boundary conditions

$$U(\tau \to -\infty) = 1, \quad U(\tau \to \infty) = 0 \tag{5.12}$$

denote the stable and the unstable states respectively. To study Eq. (5.11) we split the second order differential equation into two first order differential equations in the (U, P) plane, called the phase plane as follows

$$\frac{dU}{d\tau} = g(U,P) \ = \ P, \tag{5.13}$$

$$\frac{dP}{d\tau} = h(U,P) \ = \ -vP - U(1-U). \tag{5.14}$$

In the phase space approach it is easy to handle higher order differential equations by mapping into first order differential equations and with the fixed points one can know the bulk behavior by extrapolating the behavior around the fixed points in the space. By equating Eqs. (5.13) and (5.14) to zero, one would get the fixed points ((U_s, P_s)) which are $(0,0)$ and $(1,0)$. Here s runs over $1,2$. The points in the phase plane correspond to the stable and the unstable states respectively. Since these fixed points control the whole dynamics, the aim would be to concentrate on the region around these points. The ratio of the above two differential equations,

$$\frac{dP}{dU} = \frac{-vP - U(1-U)}{P}, \tag{5.15}$$

justifies calling fixed points as singular points. Eq. (5.15) possesses a unique solution over the phase space except at the fixed points, *i.e.*, only one trajectory will pass through any point on the phase space. Here the region of interest can be studied by the linearized function $g(U,P)$ and $h(U,P)$ considering $(U-U_s)$ and $(P-P_s)$ to be small. The stability operator is obtained from Eqs. (5.13) and (5.14), by the Taylor expansion of $g(U,P)$ and $h(U,P)$ about the fixed points and by keeping the leading order terms. The velocity of the front is determined by the eigenvalue equation of the stability operator. Eqs. (5.13) and (5.14) describe the flow in the phase plane (U, U') corresponding to the stable fixed point $(0,0)$ and unstable fixed point $(1,0)$. Here τ plays the role of time. The uniformly translating front solutions of Eqs. (5.13) and (5.14) corresponding to the trajectories between the two fixed points are given by

$$\begin{pmatrix} U' - {U_s}' \\ U - U_s \end{pmatrix} = c_1 a_j e^{\lambda_- \tau} + c_2 b_j e^{\lambda_+ \tau}, \tag{5.16}$$

where c_1 and c_2 are arbitrary constants, a_j and b_j(for $j = 1,2$) are the eigen vectors of the stability matrix corresponding to the eigenvalues λ_j. The eigenvalues for the fixed points $(0,0)$ and $(1,0)$ respectively are given by,

$$\lambda_\pm = \frac{1}{2}[-v \pm \sqrt{v^2-4}] \Longrightarrow \begin{cases} \text{stable} \quad \text{node} \quad \text{for} \quad v^2 > 4 \\ \text{stable} \quad \text{spiral} \quad \text{for} \quad v^2 < 4 \end{cases} \tag{5.17}$$

and

$$\lambda_\pm = \frac{1}{2}[-v \pm \sqrt{v^2+4}] \Longrightarrow \text{saddlepoint}. \tag{5.18}$$

Eq. (5.17) puts a bound on the velocity. The critical velocity obtained is $v^* = 2$. With velocity $v \geq v^*$ we get the stable node whereas for $v < v^*$, U shows an oscillatory behavior, corresponding to the stable spiral node. But as per the boundary conditions, $v < v^*$ is forbidden. The threshold velocity v^* is called the marginal velocity. The linear stability analysis around the unstable fixed point gives the stable node for $(0,0)$ and saddle point for $(1,0)$. The trajectory connecting these two fixed points is shown in

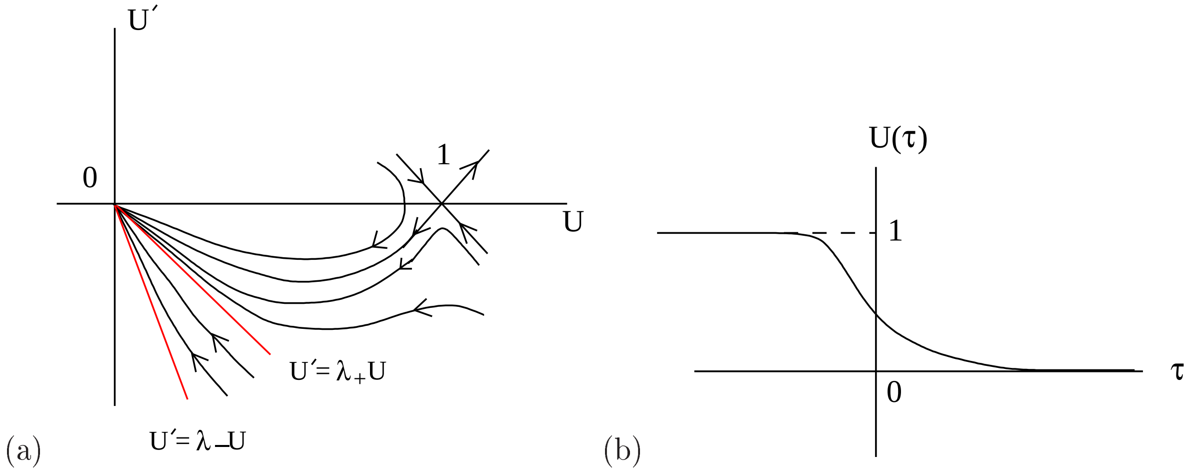

Figure 5.2: (a) Two fixed points $(0, 0)$ and $(1, 0)$ in the phase space are connected by a separatrix. Arrows represent the direction of flows. Each line represents a trajectory in the phase space. Red lines are the two eigen vectors with eigenvalues λ_-, λ_+. (b) This is the profile of the front moving along the positive τ direction. In (a), as one starts from $(1, 0)$, where $U = 1$, moves along the trajectory with $U' < 0$ everywhere, and reaches $(0, 0)$, where $U = 0$, one gets the separatrix connecting the two fixed points. The front profile follows from this particular trajectory.

Fig. 5.2(a). The front profile is obtained from the separatrix, connecting the two fixed points, when $U(\tau)$ is plotted with τ. The wave solution shown in Fig. 5.2(b) moves along the positive z direction with uniform velocity $v^* = 2$.

Therefore we see that the interface between the two homogeneous states propagates from an unstable state to a stable state with a well defined velocity. A linear stability analysis about the unstable position determines the linear marginal stability. In the asymptotic limit the front approaches the critical velocity v^* which shows that the front has the uniformly traveling wave solution. We exploit this methodology to study the dynamics of the B-Z interface.

5.2 Model

Our model consists of three states B, the denatured state, and Z, to be represented by the parameter $\phi = -1, 0, 1$, respectively. The space and time coordinates z and t are taken to be continuous. It is a one dimensional problem where $\phi(z, t)$ describes the state of the coarse-grained base-pair at index z along the DNA. For the B-Z transition, we take $\phi = -1$ (B state) to be unstable (or metastable) which is getting invaded by the stable state at $\phi = 1$ (Z state). We study this phenomenon through a Landau free energy $F(\phi)$ taken as a sixth order polynomial with the coefficients chosen to have extrema at

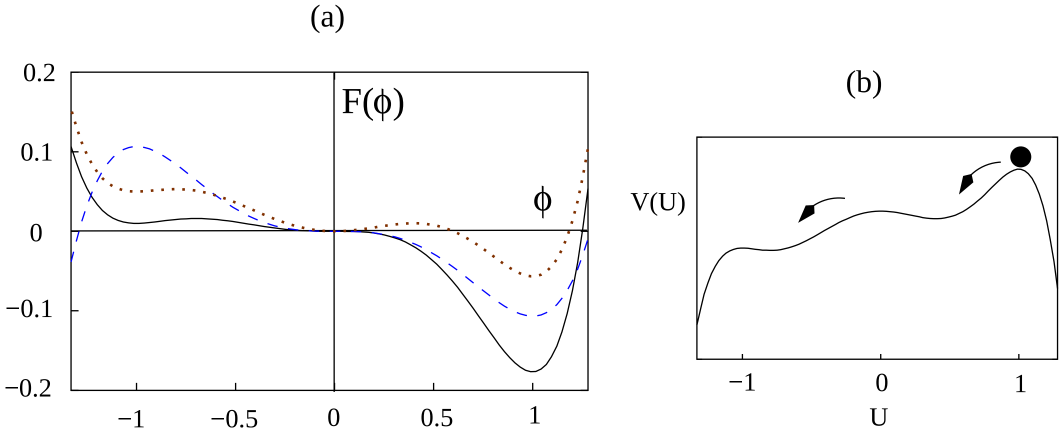

Figure 5.3: (a) The Landau function $F(\phi)$ as a function of ϕ. In all cases, $\phi = 1$ is the stable state, Z-DNA, $\phi = -1$ represents an unstable (dashed line) or metastable (solid and dotted lines) state, B-DNA while $\phi = 0$ is a quadratically unstable (solid and dashed lines) or metastable (dotted line) state, denatured state. The three cases I, II and III in the text correspond to dotted, solid and dashed lines. (b) Potential $V(U) = -F(U)$ for the particle-on-a-hill analogy.

$\phi = 0, \pm 1$. This is ensured by choosing the thermodynamic force $f(\phi)$ as

$$f(\phi) = -\frac{dF(\phi)}{d\phi} = \phi(\phi+\alpha)(\phi-\beta)(1-\phi)(1+\phi), \tag{5.19}$$

where $\alpha,\ \beta > 0$ are constants, whose values are system specific. Needless to say, the relative stability of the three phases can be adjusted by α, β. The Landau Ginzburg free energy is taken as

$$\mathcal{H}(\phi) = \int dz \left[\frac{D}{2}\left(\frac{\partial\phi}{\partial z}\right)^2 + F(\phi)\right], \tag{5.20}$$

where $D > 0$ is the elastic constant. D-term allows inhomogeneity, e.g., at the interface between two phases. The three homogeneous phases are given by the minima of the Landau free energy $F(\phi)$. The dynamics is governed by the non linear diffusion equation

$$\frac{\partial\phi}{\partial t} = -\frac{\partial\mathcal{H}}{\partial\phi} = D\frac{\partial^2\phi}{\partial z^2} + f(\phi), \tag{5.21}$$

derived from Eq. (5.20) in the overdamped limit. The geometry to be considered is such that the B state is on one side and the Z state on the other with the front moving towards the unstable state. For the B-Z case, this is ensured by the boundary conditions

$$\phi(z \to -\infty,\ t) = 1, \quad \phi(z \to \infty,\ t) = -1$$

for Eq. (5.21) for all time. A few other boundary conditions are considered too. The three generic cases obtained by fixing α and β are the following (see Fig. 5.3(a))

- Case I : while quenching to the stable state, Z, state B remains in a metastable state while the denatured state $\phi = 0$ is also metastable. Since the barriers are somewhere in between $\phi = -1$ and $\phi = 1$, we have $0 \leq \alpha, \beta < 1$.
- Case II : the metastable state (B-DNA) sees a barrier somewhere inbetween -1 to 0, while the denatured state is quadratically unstable state. This case is for $0 < \alpha < 1$, and $\beta = 0$.
- Case III : unstable B state quenched into stable Z while the denatured state remains in a quadratically unstable state (i.e., without facing any barrier). This happens when $\alpha > 1$ and $\beta = 0$.

To be noted that cases I and II are similar to the free energy landscape obtained in Ref. [102] as the potential of the mean force obtained from molecular dynamics.

The diffusive term in Eq. (5.21) coming from the elastic part of Eq. (5.20) tends to smoothen out any inhomogeneity while the driving force $f(\phi)$ tends to favour the stable state whenever there is any inhomogeneity. The combined effect of the diffusion like spreading and the selection of one phase by the drive leads to a steady state where the interface shows a uniform motion and takes a shape which is not necessarily the equilibrium shape [99]. Based on the Fisher-Kolmogorov (F-K) idea, the traveling wave solution $\phi(z, t) = U(z - vt)$ can be used to rewrite Eq. (5.21) as

$$\frac{d^2U}{d\tau^2} + v\frac{dU}{d\tau} + f(U) = 0, \quad (\tau = z - vt), \tag{5.22}$$

where v the velocity of the front is to be determined. The interface which we are studying is between $\phi = +1$ and $\phi = -1$ states. Eq. (5.22) can be interpreted as the motion of a particle moving in a potential $V = -F(U)$ (Fig. 5.3(b)) starting at the hill at $U = +1$ at time $\tau = -\infty$ just reaching the other hill at $U = -1$ at time $\tau = +\infty$ losing energy due to "friction" v. For a given potential, such a motion is possible only for particular values of v and that velocity is the selected velocity of the front. However, it is also possible that the particle spends an infinite amount of time in the intermediate state so that the descent from $U = +1$ to $U = 0$ and the descent from $U = 0$ to $U = -1$ are independent requiring two different friction coefficients. The physical picture that emerges is that the stable state moves towards the unstable state, and the propagating front will have a time independent shape and a constant velocity v. However in some situations, the initial big front separating the two phases $\phi = \pm 1$ splits into two, one front between $\phi = -1$ and $\phi = 0$, while the other one between $\phi = 0$ and $\phi = 1$. The two smaller fronts move

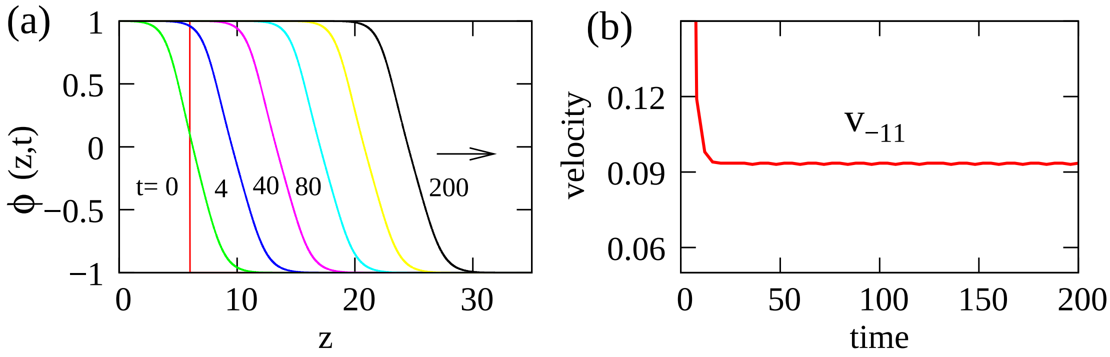

Figure 5.4: For $\alpha = 0.4$ and $\beta = 0.2$. (a) The time evolution of the profile is shown. The plot ϕ *vs* z for different time t as marked. Arrow shows the direction of velocity. The stable state Z invades B. (b) Velocity as a function of time. With time, the velocity approaches a uniform value.

with different shapes and speeds v_{-10}, v_{01}. The $\phi = 0$ state may then get dynamically generated. Consequently one may see the development of the denatured state. The less preferable state will eventually be devoured by the stable state completing the transition from B- to Z-DNA.

5.3 Dynamic phase diagram

5.3.1 Numerical approach

The velocity of the front has been determined by numerical analysis for different boundary conditions like (a) $\phi(-\infty,t) = 1$, $\phi(\infty,t) = -1$ for the B-Z front, (b) $\phi(-\infty,t) = 1$, $\phi(\infty,t) = 0$ for a front between Z and the denatured state, (c) $\phi(-\infty,t) = 0$, $\phi(\infty,t) = -1$ for a front between B and the denatured state. The initial ($t = 0$) interface of width w is located at $z = z_0$ where z_0 chosen away from the boundary and a Crank Nicolson method is used to evolve the nonlinear diffusion equation. For numerical solution we choose discrete lattice spacing and time of the order 10^{-2} and the diffusion constant D of the order 1. The interface evolves to its steady state starting from any arbitrary initial profile as shown in Fig. 5.4(a) for $\alpha = 0.4$ and $\beta = 0.6$ (Case I). The initial profile at $t = 0$ is taken very sharp and seems to evolve with time as shown in the diagram. Once a steady state is reached, the velocity is determined by locating the positions at which $\phi = \pm.5$, and $\phi = 0$ as appropriate. The velocity corresponding to the profile in Fig. 5.4(a) approaches a uniform velocity with time and is shown in Fig. 5.4(b). Since the F-K analysis is based on the linear stability analysis around the unstable fixed point, in the case of the split front, only the velocity v_{01} can be obtained by the F-K analysis, but not in general.

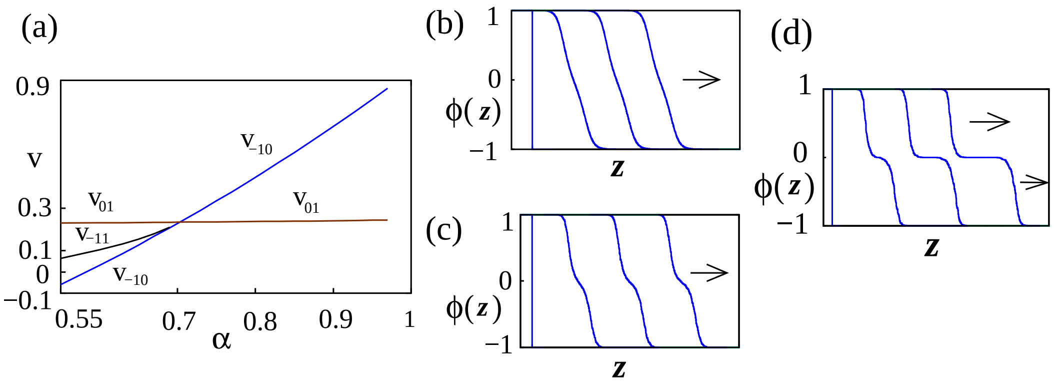

Figure 5.5: (a) Plot of velocity *vs* α for a fixed value of $\beta = 0.45$. Three velocities meet at a common point at $\alpha_c(\beta)$. The remaining three figures (ϕ *vs* z) represent the time evolution of the front (or fronts). (b) A single front for $\alpha = 0.6 < \alpha_c(\beta)$. (c) A single front for $\alpha = 0.7$ near $\alpha_c(\beta)$ with a signature of the width widening but no "0" phase. (d) For $\alpha = 0.72 > \alpha_c(\beta)$ single front splits into two fronts.

The dependence of the velocities on α for a fixed β is shown in Fig. 5.5(a). We see that three fronts move with different velocities for $\alpha < \alpha_c(\beta)$ with $v_{01} > v_{-11} > v_{-10}$. All these velocities are same at $\alpha = \alpha_c(\beta)$. For $\alpha > \alpha_c(\beta)$, the B-Z front splits into two fronts and the denatured state grows with time as $(v_{-10} - v_{01})\,t$. It is straightforward to see that no stable front between ± 1 can exist if $v_{-10} < v_{01}$. Also the v_{-11} curve ends at $\alpha_c(\beta)$ and has no continuation for $\alpha > \alpha_c(\beta)$. This indicates that $\alpha_c(\beta)$ is a singular point.

The numerically determined $\alpha_c(\beta)$ *vs* β line is shown in Fig. 5.6. This is the *phase diagram for dynamics* with the phase boundary as the limit of stability of the BZ front (from below). The intersection of the critical and $\alpha = \beta$ lines, turns out to be an equilibrium point. The phase diagram can be confirmed by considering a few special cases. For $\alpha = \beta$, the free energies of B and Z are same (see dotted curve in Fig. 5.7(b)) and the BZ front should have zero velocity. The point $\alpha = \beta = \frac{1}{\sqrt{3}}$ corresponds to the equilibrium situation with equal free energies of all the states (see dashed curve in Fig. 5.7(b)), for which all the three fronts are static, and therefore the condition to be on the phase boundary is trivially satisfied. This point is denoted by q in Fig. 5.6. Along the $\alpha = \beta$ line for $\alpha < \alpha_c(\beta)$, $v_{01}, v_{-10} \neq 0$ with state $+1$ or -1 invading 0. In contrast in region 2, along the same $\alpha = \beta$ line, "0" is the stable state and it invades both ± 1 states. In region 2 above the dotted line, obtained by equating $F(1) = F(0)$ [Eq. (5.19)], the "0" state grows with the two fronts moving away from each other as shown in Fig. 5.8(a) for $\alpha = 0.7$ and $\beta = 0.6$ and corresponding velocities in Fig. 5.8(b), but below that dotted line in region 1 the Z state grows though the fronts move in the same direction (towards right). The Z ↔ B symmetry in our choice of the free energy mandates a symmetric

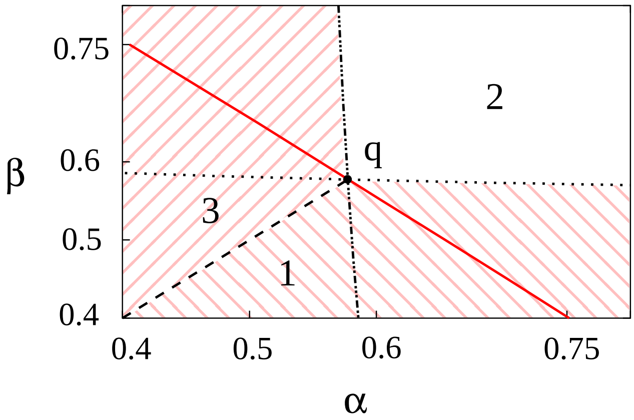

Figure 5.6: Dynamic phases in a plot of α *vs* β, the boundary (solid red line) being given by $\alpha = \alpha_c(\beta)$. In the region below the boundary line, a single front between -1 to 1 (big front) propagates without splitting. In the region above the boundary line the front between -1 to $+1$ splits into two (small) fronts. Z, "0" and B are the stable states in regions 1, 2 and 3, respectively. The dotted line corresponds to $v_{01} = 0$, while the dash-dotted line to $v_{-10} = 0$ and the corresponding free energies are shown in Fig. 5.7(a). The split fronts move away from each other in region 2 (corresponding free energy curve is shown in Fig. 5.7(b) by a dotted line), both towards right in 1 and both towards left in 3, as per the chosen boundary conditions. The big front has zero velocity on the $\alpha = \beta$ line and the corresponding free energy curve is shown in Fig. 5.7(b) by a solid curve. The diagram is symmetric around the $\alpha = \beta$ line. Point q represents the equilibrium point, where three states have the same free energy as shown in Fig. 5.7(b) by a dashed curve.

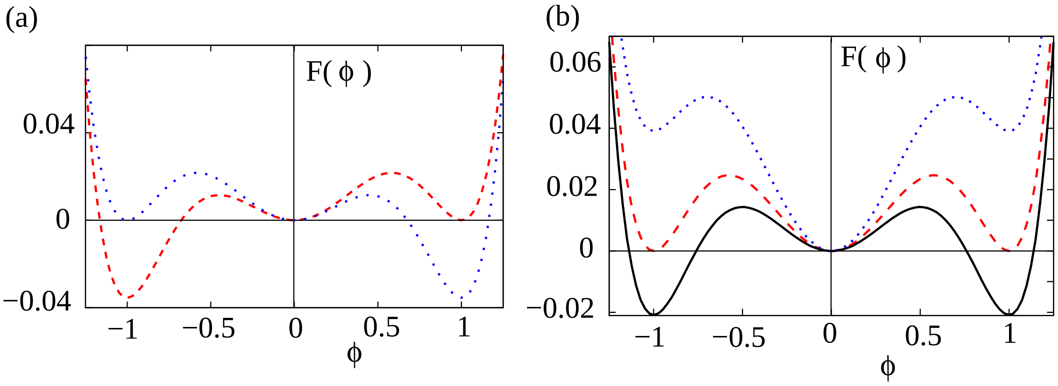

Figure 5.7: Plot of $F(\phi)$ as a function ϕ. (a) Dotted curve with $\alpha = 0.583$, $\beta = 0.45$ corresponds to $v_{-10} = 0$, and dashed curve with $\alpha = 0.45$, $\beta = 0.583$ corresponds to $v_{01} = 0$. (b) The Landau function $F(\phi)$ as a function ϕ. Dotted curve is for $\alpha = \beta = 0.7$, dashed curve is for $\alpha = \beta = \frac{1}{\sqrt{3}}$ and solid curve is for $\alpha = \beta = 0.5$.

phase diagram across the $\alpha = \beta$ line with the fronts moving towards left in region 3.

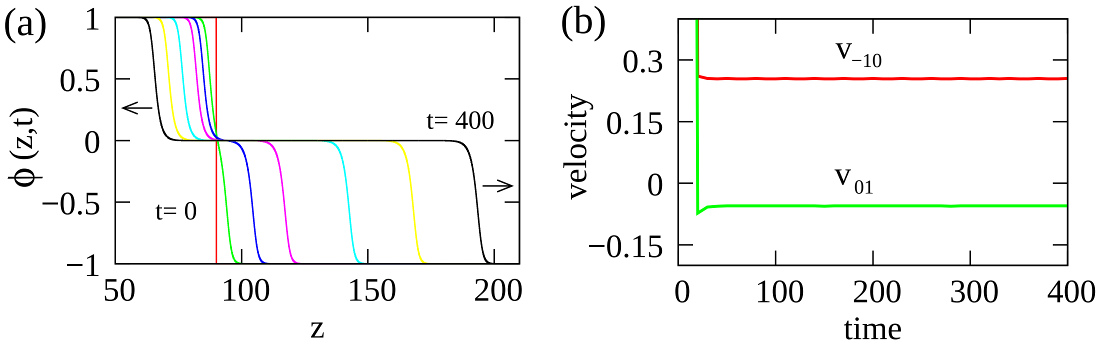

Figure 5.8: For $\alpha = 0.7$ and $\beta = 0.6$. (a) The time evolution of profile is shown to split into two parts. The plot ϕ *vs* z is for different time t as marked. Arrows show the direction of velocity. The split fronts move opposite to each other. The denatured state invades both B and Z. (b) Velocity as a function of time. With the time, the velocity of the lower and the upper fronts v_{-10} and v_{01} approach the uniform velocities. The negative velocity represents the front propagation towards $-z$ direction.

5.3.2 Perturbative approach

If a small change causes a small effect, then a perturbation theory is applicable. So a perturbative analysis around the point of equilibrium can be done provided the free energy difference between the two states is small enough, to deduce the dynamical properties from the static or the unperturbed case. Here for α, β close to the equilibrium point $\alpha = \beta = \frac{1}{\sqrt{3}}$, a perturbative analysis [103] is done to determine the velocity, which is now a small parameter. With a small perturbation, the front solution is

$$\phi(z,t) \approx \phi_0(z) + \phi_1(z,t), \tag{5.23}$$

for the force

$$f(\phi_0 + \phi_1) \approx f(\phi) + \delta f(\phi) = f(\phi_0) + \phi_1 f'(\phi_0) + \delta f(\phi_0), \tag{5.24}$$

where $\phi_0(z)$, $f(\phi_0)$ are respectively the profile solution, and force term for the equilibrium interface. The equilibrium profile is static. Here the perturbation series is in the small parameter ϵ. With the substitution of the perturbative expressions Eqs. (5.23) and (5.24) in Eq. (5.19) and by keeping the leading order terms in the series we get,

$$\begin{aligned} \phi_0^{''}(z) &= -f(\phi_0), & (5.25)\\ \hat{H}_0\phi_1 &= \delta f(\phi_0), & (5.26) \end{aligned}$$

where

$$\hat{H}_0 = \frac{\partial}{\partial t} - \frac{\partial^2}{\partial z^2} - f_0^{'}(\phi_0(z)),$$

and prime on ϕ and f denotes the derivatives with respect to z, and $\phi(z)$, respectively. The static solution satisfies Eq. (5.25), where $\phi_0^{'}(z)$ is an eigen function with an eigenvalue $E_0 = 0$. Therefore for the rest of the nonzero eigenvalues, with eigen function $\tilde{\phi}_n(z)$, the time independent part can be written as

$$\left[\frac{\partial^2}{\partial z^2} + f^{'}(\phi_0)\right]\tilde{\phi}_n(z) = E_n\,\tilde{\phi}_n(z). \tag{5.27}$$

Let us assume Green's function of the form

$$G(z,\ z_1; t,\ t_1) = \sum_n \tilde{\phi}_n(z)\tilde{\phi}_n(z_1)e^{-E_n(t-t_1)}. \tag{5.28}$$

Therefore the solution of ϕ_1 comes out to be

$$\phi_1(z,\ t) = \int_0^t dt_1 \int_{-\infty}^{\infty} dz_1\, G(z,\ z_1; t,\ t_1)\delta f(\phi_0). \tag{5.29}$$

With the known eigenvalue corresponding to the eigen function $\phi_0^{'}$ we are able to to find ϕ_1, which is

$$\phi_1 = t\frac{\phi_0^{'}(z)\int d\phi_0\,\delta f(\phi_0)}{\int dz|\phi_0^{'}(z)|^2}. \tag{5.30}$$

Because of the existence of the traveling wave solution, by writing, to first order in the velocity v, the front solution for a small change around the equilibrium position will be

$$\phi(z,\ t) \approx \phi_0(z) - v\, t\, \phi_0^{'}(z). \tag{5.31}$$

So by comparing Eqs. (5.30) and (5.31), v can be written with the eigen function renormalization factors as

$$v = \frac{\Delta F}{\int_{\infty}^{\infty} dz |\phi_0^{\prime}(z)|^2}, \tag{5.32}$$

where,

$$\Delta F = - \int d\phi_0\, \delta f(\phi_0). \tag{5.33}$$

Thus we see that v can be determined to first order in free energy difference if ϕ_0 is known. In the equilibrium situation, there is a Goldstone like zero-energy mode [103], because, the interface can be placed anywhere or shifted along z without any cost of energy. We therefore take $\phi_0(z)$ as centered around an arbitrarily chosen origin. The static solution for the free energy $F(\phi)$ [from Eq. (5.19)] satisfies,

$$\frac{1}{2}(\phi_0^{'}(z))^2 = F(\phi_0) = \frac{1}{6}\phi_0^2(\phi_0^2 - 1)^2. \tag{5.34}$$

With a first order correction, the velocities of the interfaces are

$$v_{ij} = \frac{\epsilon_{ij}}{\int_{-\infty}^{\infty} dz [\phi_0^{\prime}(z)]^2}, \tag{5.35}$$

where $i, j = 0, \pm 1$, and the free energy differences ϵ_{ij} are

$$\epsilon_{01} = -\frac{1}{12} - 2\frac{(\alpha-\beta)}{15} + \frac{\alpha\beta}{4}, \tag{5.36}$$

$$\epsilon_{-10} = \frac{1}{12} - 2\frac{(\alpha-\beta)}{15} - \frac{\alpha\beta}{4}, \tag{5.37}$$

$$\epsilon_{-11} = -4\frac{(\alpha-\beta)}{15}. \tag{5.38}$$

At the point of equilibrium $\alpha = \beta = \frac{1}{\sqrt{3}}$, all these front velocities are zero implying the static fronts. At the perturbative regime, by equating the velocities, we find the slope of the critical line around $(\frac{1}{\sqrt{3}}, \frac{1}{\sqrt{3}})$. The slope can be obtained from

$$\epsilon_{01} = \epsilon_{-10} \quad \text{or} \quad \epsilon_{01} = \epsilon_{-11}/2. \tag{5.39}$$

For the small fluctuations on α and β *i. e.*, for $\alpha \rightarrow \frac{1}{\sqrt{3}} + \delta\alpha$ and $\beta \rightarrow \frac{1}{\sqrt{3}} + \delta\beta$, from

Eq. (5.39) we get

$$\delta\alpha = -\delta\beta. \tag{5.40}$$

Thus we see that around the point of equilibrium the straight line is with the slope -1, which is consistent with the numerically determined phase boundary shown in Fig. 5.6. Moreover we also find the phase boundary to deviate very slightly from a straight line over the range shown there. There is a deviation from linearity beyond that but the numerical error becomes larger.

We next study the behavior of the width of the interface and of the appropriate timescale for the dynamics. For the special case of $\beta = 0.5$ as $\alpha \to \alpha_c(\beta)$ the divergence of the width has been noted in Ref. [104]. At $\alpha = \beta = \frac{1}{\sqrt{3}}$, any length of "0" domain can be inserted and therefore the width of the BZ interface at the limit of stability is infinity. On the split-front side (Fig. 5.5(d)), the width increases linearly with time as $W = (v_{01} - v_{-10})t$ [Fig. 5.9(a) for $\alpha = 0.75205$]. While, on the other side of the phase boundary the single front (Fig. 5.5(b)) has a finite width (Fig. 5.9(a) for $\alpha = 0.745$). Close to the phase boundary though a deformation of the moving front is visible around $\phi = 0$ (Fig. 5.5(c)), but width saturates at large time (Fig. 5.9(a) for $\alpha = 0.75175$) without any appearance of the denatured phase. Hence scaling forms are expected as

$$W \sim |\,\alpha - \alpha_c(\beta)\,|^{-\mu}, \quad \tau \sim W^{\mathsf{z}}.$$

Fig. 5.9(a) shows the time evolution of the width of an interface for various α at a fixed β, where the instantaneous width W of the interface at time t is obtained as

$$\begin{aligned} W^2 &= <z^2> - <z>^2, \text{ where} && (5.41)\\ <z^n> &= \frac{\int z^n \left(\frac{d\phi(z,t)}{dz}\right)^2 dz}{\int \left(\frac{d\phi(z,t)}{dz}\right)^2 dz}. && (5.42) \end{aligned}$$

Another way to characterize the width would be to look at the slope of the profile *i. e.*, $\left.\frac{d\phi(z)}{dz}\right|_{\phi=0}$, which is related to the inverse of W and also shows the scaling with characteristic dynamic exponent. We started with an interface that has an insertion of the "0" state and the width monitors the decay or the growth of the "0" state. The width saturates exponentially for $\alpha < \alpha_c(\beta)$ albeit slowly near $\alpha \to \alpha_c-$, while a linear growth is observed for $\alpha > \alpha_c(\beta)$. Time here refers to the discretized time in the Crank-Nicolson approach. By fitting an exponential to the time evolution of W, the characteristic time scale was determined, for $\alpha < \alpha_c(\beta)$. The exponent μ is found to be rather small, not inconsistent with the logarithmic growth observed in Ref. [104]. Fig. 5.9(b) shows the log-log plot of τ *vs* W indicating a value of z within 3.0 to 4.0. However for better accuracy one requires a large system and long time observation as well. The divergences of W and τ with scaling establish the critical nature of the $\alpha = \alpha_c(\beta)$ line.

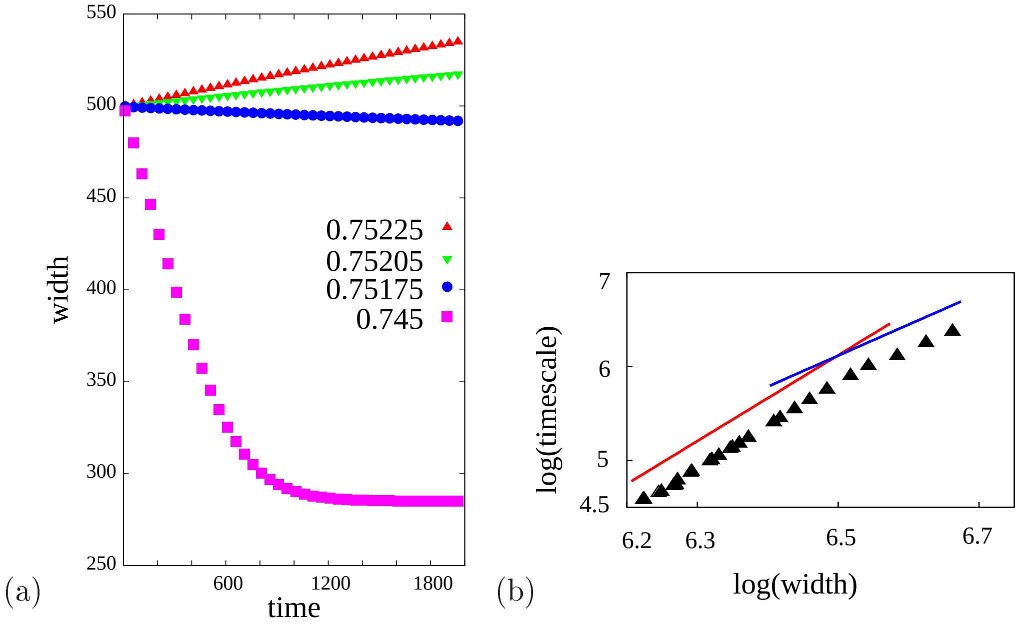

Figure 5.9: (a) Time evolutions of the width (in arbitrary units) of the front are shown for different values of α keeping $\beta = 0.4$ fixed. The initial front had a stretch of "0" phase which decays for $\alpha < \alpha_c(\beta)$ but grows linearly for $\alpha > \alpha_c(\beta)$. The timescale to reach saturation increases as $\alpha \to \alpha_c(\beta)-$. For this case $\alpha_c(\beta) \approx 0.752$. (b) Log-Log plot of width versus time scale for $\alpha < \alpha_c(\beta)$. Two solid line slopes are shown far from and near $\alpha_c(\beta)$.

Despite the immense success in probing the various phases of DNA by single molecular manipulation techniques, interfaces have not been explored thoroughly. We hope our results will motivate direct studies of interfaces of DNA, especially their stability. Even on the theoretical front, it remains to be seen if all atom molecular dynamics simulations that have been successful [102, 105, 106] in seeing various phases, can be used to monitor the dynamics of interfaces, B-Z in particular, under given boundary conditions.

5.4 Conclusion

In this chapter we have studied the conformational transition from B-DNA to Z-DNA. We have considered the Landau free energy to describe the B-Z interface and have formulated the propagating front equation. With the wave front propagation approach and the numerical calculations we have obtained the dynamic phase diagram. The dynamic phase diagram for the steady state is obtained in the α-β plane, where α, β characterize the relative stability of the phases, by the critical value α_c for different values of β. We have obtained an equilibrium point, the Goldstone like free energy mode. The phase boundary in the α-β plane has been determined and corroborated by a perturbation analysis. The dynamic transition is associated with diverging length and time scales and has its own dynamic exponent. On one side of the phase boundary the dynamics involves propagation of one B-Z interface with a uniform speed, while on the other phase such an interface is unstable leading to the formation of the thermodynamically forbidden denatured state. This in turn, suggests that there is no unique mechanism for the B-Z dynamics and it is possible to switch from one type to other by tuning the parameters. A resolution of the controversy in experiments is that the two cases, namely nanotube and magnetic tweezers are on the two sides of the phase boundary.

6

Summary

In this thesis we have studied the melting of a triple-stranded DNA and the conformational transitions of a double-stranded DNA from the B from to the Z form of DNA. To address the problems we have adopted real-space RG, exact iteration, wave front propagation and perturbation methodologies.

In the introductory section we reviewed on the following topics:

- We introduced the double and the triple helix DNA. Following the direct analogy between DNA and quantum mechanics we discussed the quantum Efimov effect exhibited by a three-particle system.

- Directed polymer on hierarchical lattices and on fractal lattices like the Sierpinski Gasket are introduced. We reviewed some exact results of the directed polymer chains solved on such pseudo lattices.

- We gave a brief introduction to the real-space RG. The zeros of the partition function associated with the phase transition are discussed. Thereafter the Julia sets in connection with the zeros of partition function are discussed.

- Various thermodynamical studies including melting, unzipping and other thermodynamic properties of the double-stranded and the triple-stranded DNA have been reviewed.

- The conformational transition of B- to Z-DNA has been introduced. This includes the introduction to the B and the Z form of DNA, the B-Z transition mechanism, the role of the BZ interface and the existing contradictory hypotheses on this transition.

We modeled the three-chain system as three directed walks on a diamond hierarchical lattice of dimension $d > 2$, and used the real-space RG method. We studied both the cases of symmetric and asymmetric pair interactions. By looking at the RG flows of the two- and the three-chain Boltzmann factors we predicted the existence of an effective three-strand bound state in conditions where duplex would be in the denatured state. Such a loosely bound state is called the Efimov-DNA. Further exact numerical calculations are used to validate the prediction of such a polymeric Efimov effect. We found the nonzero three-chain average energy in the unbound region of the duplex DNA. The Efimov transition point was found to be discontinuous. The Efimov DNA was found thermodynamically more stable than the duplex DNA. In addition we showed different Efimov transition points for different dimensions.

The prediction of the Efimov-analog three-chain bound state was corroborated by the zeros of the partition function. These zeros produce fractal-like structures, and they pinch the real axis in the thermodynamic limit with an angle determined by the exponents characterizing the phase transition. We found that all the transition points obtained from RG flows, are consistent with the zeros of the partition function. We showed that the Efimov effect occurs even if the three-chain interaction is repulsive in nature. We found that a transition can be induced in higher dimensions ($d > 4.1$) from the Efimov state to the three-chain critical repulsive state, when chains are critically paired. We emphasized on the nature of the transitions and found that the transition to this three-chain critical repulsive state is continuous obeying a finite size scaling law with exponents obtained from the RG. In addition we found a new state, where three chains are bound with no three chain contact.

The existence of an Efimov DNA was further verified on a Sierpinski Gasket lattice of dimension $d < 2$ by applying some extra weight factors to the polymer chains. A new state to be called a mixed state is found, where in closer view any two chains are always bound keeping the third free, but in global view no one is free. The mixed phase was found to be a separate phase, where as the Efimov state appeared as a crossover. We suggested that the triplex DNA might provide a unique, amenable biological testing ground for the Efimov effect.

We gave a theoretical explanation to the B-Z transition mechanism. We modeled a Landau free energy and applied the wave front propagation approach to find the steady state velocity of the B-Z interface. By varying the system parameters determining stability and instability of the homogeneous states, we obtained a dynamic phase diagram, which was further corroborated by a perturbation analysis. We found that, on one side of the phase boundary no intermediate state is formed but on the other side of the phase boundary "0" state is preferred. As a result the denatured state develops dynamically eventhough it is thermodynamically forbidden. We showed that the dynamic transition is associated with a diverging length scale with its own dynamic exponent. Such a theoretical analysis resolves the current controversies on the transition mechanism of the B-DNA to Z-DNA.

A

Julia set

Earlier we discussed the Julia set in Chap. 1 and Chap. 3. We give an example of a quadratic equation [Eq. (1.12)] to describe the Julia set. In the same spirit, the two-chain RG relation [Eq. (3.2)] is written in a quadratic form as

$$z_n = \frac{z_{n-1}^2}{b} + c', \tag{A.1}$$

where $c' = \frac{b-1}{b}$. At the critical threshold of two-chain melting (*i. e.*, $y = y_c$), the three-chain RG relation [Eq. (3.3)] can be written as

$$z_n = \frac{(b-1)^3}{b^2} z_{n-1}^2 + c'', \tag{A.2}$$

where $c'' = \frac{b-2}{b^2(b-1)^2} + \frac{3}{b^2}$. Here c', c'' are not arbitrary and are determined by b. In our model c', c'' come out to be real. We obtained fractal-like structures, as discussed in Chap. 3.

B

Limit cycle

The connection between the quantum Efimov effect and RG limit cycles is discussed in Ref. [21]. The emergence of an infinite number of bound states at the critical two-body zero-energy state is linked to the limit cycle behaviour. A limit cycle is an isolated closed loop with certain periodicity, which appears due to the complex fixed points obtained from the RG flow equation, and where the running parameter *e. g.*, coupling constant retraces the path of that closed loop forever with a certain periodicity.

For two successive generations Eq. (3.3) will be

$$w_n - w_{n+1} = f(w_{n+1}) - w_{n+1}. \tag{B.1}$$

But if the continuum limit is taken, Eq. (B.1) can be written as

$$l\frac{dw}{dl} = -(w - w_+)(w - w_-), \tag{B.2}$$

at the critical line $y_c = b - 1$, where $l = \ln L$ and $L = 2^n$. For complex $w_\pm = \alpha \pm i\beta$, the solution of Eq. (B.2) is then

$$w = \alpha - \beta \tan \beta(\ln l + \theta), \tag{B.3}$$

where θ is the integration constant. The above equation reflects the periodicity of w in $\ln l$ with the property

$$w(l) = w(l\lambda), \text{ where } \ln \lambda = \frac{\pi}{\beta}. \tag{B.4}$$

Here as l increases w approaches $\pm\infty$. This behavior can be mapped into a limit cycle in the complex plane with a phase factor defined by the equation

$$e^{i\phi} = \frac{w - w_+}{w - w_-}. \tag{B.5}$$

With the help of Eq. (B.2) and its derivative, ϕ will be

$$\phi = \frac{\beta}{\alpha} \ln l + \phi_0, \tag{B.6}$$

where ϕ_0 is the integration constant.

Our model on the hierarchical lattice is a discrete model. Certainly a limit cycle is obtainable from the RG relations in the continuum limit, but it is not straight forward to do so in the discrete case.

Bibliography

[1] J. D. Watson and F. H. Crick, Nature **171**, 737 (1953).

[2] Richard R. Sinden, *DNA Structure and Function* (Academic press, Sandiego, 1994).

[3] Chris R. Callandine *et al.*, Understanding DNA, Third Edition: The Molecule and How it Works (Academic press, UK, 2004).

[4] G. Felsenfeld, D. R. Davies and A. Rich, J. Am. Chem. Soc. **79**, 2023 (1957).

[5] H. E. Moser and P. B. Dervan, Science **238**, 645 (1987).

[6] T. Le Doan *et al.*, Nucleic Acids Res. **15**, 7749 (1987).

[7] K. Hoogsteen, Acta Cryst. **12**, 822 (1959).

[8] R. W. Roberts and D. M. Crothers, Science **258**, 1463 (1992).

[9] P. E. Nielsen, Ann. Rev. Biophys. Biomol. Struct. **24**, 167 (1995).

[10] L. Betts *et al.*, Science **270**, 1838 (1995).

[11] A. Jain *et al.*, Biocheimie **90**, 1117 (2008).

[12] M. D. Frank-Kamenetskii and S. M. Mirkin, Ann. Rev. Biochem. **64**, 65 (1995).

[13] V. Soifer and V. N. Potaman, *Triple-helical nucleic acids*, (Springer, New York, 1996).

[14] P. P. Chan and P. M. Glazer, J. Mol. Med. **75**, 267 (1997), and references therein.

[15] C. Giovannangeli, N. T. Thuong, and C. Helene, Proc. Natl. Acad. Sci. USA **90**, 10013 (1993).

[16] E. R. Kandimalla and S. Agrawal, Gene **149**, 115 (1994).

[17] V. Efimov, Phys. Letts. **B 33**, 563 (1970).

[18] V. Efimov, Yad. Fiz. **12**, 1080 (1970) (Sov. J. Nucl. Phys. **12**, 589 (1971)).

[19] V. Efimov, Sov. J. Nucl. Phys. **29**, 546 (1979).

[20] A. C. Fonseca, E. F. Redish, and P. E. Shanley, Nuc. Phys. **A320**, 273 (1979).

[21] E. Braaten and H. W. Hammer, Phys. Rept. **428**, 259 (2006).

[22] M. Zaccanti *et al.*, Nature Physics **5**, 586 (2009).

[23] T. Kraemer *et al.*, Nature **440**, 315 (2006).

[24] D. V. Fedorov, A. S. Jensen, and K. Riisager, Phys. Rev. Lett. **73**, 2817 (1994).

[25] S. Mukherji and S. M. Bhattacharjee, Phys. Rev. **E 63**, 051103 (2001), and references therein.

[26] J. Maji, S. M. Bhattacharjee, F. Seno, and A. Trovato, New J. Phys. **12** 083057 (2010).

[27] C. Vanderzande, *Lattice Models of Polymers* ((Cambridge Lecture Notes in Physics) Cambridge University Press, Cambridge, 1998).

[28] P. G. de Gennes, *Scaling Concepts in Polymer Physics* (Cornell University Press, Ithaca, N. Y., 1979).

[29] M. Doi and S. F. Edwards, The theory of Polymer dynamics (Oxford University Press, New York, 1986).

[30] R. Kapri, Ph. D. Thesis (Homi Bhaba National Institute, 2007), and references therein.

[31] M. Kaufman and R. B. Griffiths, Phys. Rev. **B 24**, 496 (1981).

[32] S. Mukherji and S. M. Bhattacharjee, Phys. Rev. **E 52**, 1930 (1995).

[33] D. Marenduzzo, A. Maritan, and F. Seno, J. Phys. A: Math. Gen. **35**, L233 (2002).

[34] T. A. S. Haddad and S. R. Salinas, Physica **A 306**, 98 (2002).
T. A. S. Haddad, R. F. S. Andrade, and S. R. Salinas, J. Phys. **A**: Math. Gen. **37** 1499 (2004).

[35] M. Hinczewski and A. N. Berker, Phys. Rev. **E 73**, 066126 (2006).

[36] M. S. Cao, J. Stat. Phys. **71**, 51 (1993).

[37] B. Derrida, R. B. Griffiths, Europhys. Lett. **8**, 111 (1989).

[38] A. N. Berker and S. Ostlund, J. Phys. **C 12**, 4961 (1979).

[39] R. G. Palmer, D. L. Stein, E. Abrahams, and P. W. Anderson, Phys. Rev. Lett. **53**, 958 (1984).

[40] S. R. McKay and A. N. Berker, Phys. Rev. **B 29**, 1315 (1984).

[41] L. de Arcangelis, A. Coniglio, and S. Redner, Phys. Rev. **B 36**, 5631 (1987).

[42] A. Coniglio, L. de Arcangelis, and H. J. Herrmann, Physica **A 157**, 21 (1989).

[43] A. Chakrabarti and B. Bhattacharyya, Phys. Rev. **B 54**, R12625 (1996).
A. Chakrabarti, J. Phys.: Condens. Matter **8**, L99 (1996).

[44] D. Dhar, J. Math. Phys. **19**, 1 (1978).

[45] M. Di Stasi, F. Seno, and A. L. Stella, J. Phys. A: Math. Gen. **25**, 3891 (1992).

[46] S. Kumar and Y. Singh, J. Stat. Phys. **89**, 981 (1997).

[47] Y. Gefen, B. B. Mandelbrot, and A. Aharony, Phys. Rev. Lett. **45**, 855 (1980).

[48] P. M. Chaikin and T. C. Lubensky, Principles of condensed matter physics (Cambridge University Press, Cambridge, 1995).

[49] *Real-Space Renormalization*, edited by T. W. Burkhardt and J. M. J. van Leeuwen, Topics in Current. Physics, Vol. **30**, (Springer-Verlag, Berlin, 1982).

[50] C. N. Yang and T. D. Lee, Phys. Rev. **87**, 404 (1952).

[51] T. D. Lee and C. N. Yang, Phys. Rev. **87**, 410 (1952).

[52] M. E. Fisher, in *Lectures in Theoritical Physics*, Vol. **7**, (University of Colorado, Boulder, 1965).

[53] G. Julia, J. Math. Pures Appl. **4**, 47 (1918).

[54] B. Derrida, L. De Seze, and C. Itzykson, J. Stat. Phys. **33**, 3 (1983).

[55] M. S. Causo, B. Coluzzi, and P. Grassberger, Phys. Rev. **E 62**, 3958 (2000).

[56] D. Marenduzzo, S. M. Bhattacharjee, A. Maritan, E. Orlandini, and F. Seno, Phys. Rev. Lett. **88**, 028102 (2002).

[57] R. Kapri and S. M. Bhattacharjee, Phys. Rev. **E 72**, 051803 (2005).

[58] S. M. Bhattacharjee, J. Phys. **A 33**, L423 (2000).

[59] S. Kumar and M. S. Li, Phys. Rep. **486**, 1 (2012), and references therein.

[60] D. Poland and H. Scheraga, J. Chem. Phys. **45**, 1456 (1966).

[61] M. E. Fisher, J. Chem. Phys. **45**, 1469 (1966).

[62] Y. Kafri, D. Mukamel, and L. Peliti, Phys. Rev. Lett. **85**, 4988 (2000).

[63] R. M. Wartell and A. S. Benight, Phys. Rep. **126**, 67 (1985).

[64] J. Cook and B. Derrida, J. Stat. Phys. **57**, 89 (1989).

[65] E. Medina, M. Kardar, J. Stat. Phys. **71**, 967 (1993).

[66] K. L. Sebastian, Phys. Rev. **E 62**, 1128 (2000).

[67] D. Marenduzzo, A. Trovato, and A. Maritan, Phys. Rev. **E 64**, 031901 (2001).

[68] R. Kapri, S. M. Bhattacharjee, and F. Seno, Phys. Rev. Lett. **93**, 248102 (2004).

[69] S. Kumar and D. Giri, Phys. Rev. Lett. **98**, 048101 (2007).

[70] P. Sadhukhan, J. Maji, and S. M. Bhattacharjee, EuroPhys. Letts. **92**, 58004 (2010).

[71] M. Duca *et al.*, Nucleic Acids Res. **36**, 5123 (2008), and references therein.

[72] C. Giancola *et al.*, Themochimica Acta **372**, 129 (2001).

[73] M. D. Frank-Kamenetskii and S. M. Mirkin, Annu. Rev. Biochem. **64**, 65 (1995).

[74] E. Uhlmann, Biol. Chem. **379**, 1045 (1998).

[75] A. Delvolvé *et al.*, J. Mass Spectrum. **41**, 1498 (2006).

[76] G. E. Plum and K. J. Breslauer, J. Mol. Biol. **248**, 679 (1995).

[77] G. E. Plum, Biopolymers **44**, 241 (1997).

[78] Richard A. J. Darby *et al.*, Nucleic Acids Res. **30**, 9 e39 (2002).

[79] J. Kypr and M. Vorlickova, Gen. Physiol. Biophys., **4**, 471 (1978).

[80] A. H. Wang *et al.*, Nature London **282**, 680 (1979).

[81] M. A. Fuertes *et al.*, Chem. Rev. **106**, 2045 (2006).

[82] A. Herbert and A. Rich, J. Biological Chem. **271**, 11595 (1996).

[83] F. M. Pohl and T. M. Jovin, J. Mol. Biol. **67**, 375 (1972).

[84] J. C. Gil Montoro and J. L. F. Abascal, J. Chem. Phys. **106**, 19 (1997).

[85] A. Rich and S. Zhang, Nature Rev. Genet. **4**, 566 (2003).
C. E. Gagna and W. C. Lambert, Med. Hypothesis **60**, 418 (2003).

[86] S. Anitha *et al.*, Neuromol. Med. **2**, 289 (2002).

[87] S. C. Harvey, Nucleic Acids Res. **11**, 4867 (1983).

[88] W. Lim and Y. P. Feng, Biophys. J **88**, 1593 (2005).

[89] M. Kastenholz, T. U. Schwartz, and P. H. Hüenberger, Biophys. **J 91**, 2976 (2006).

[90] V. I. Ivanov, D. Iu. Krylov, and E. E. Miniat, Mol. Biol. (Mosk) **19**, 390 (1985).

[91] S. C. Ha *et al.*, Nature **437**, 1183 (2005).

[92] H. Urata *et al.*, Biochem. Biophys. Res. Comm. **309**, 79 (2003).

[93] S. Vichier-Guerre *et al.*, Tetrahedron Letters **38**, 93 (1997).

[94] D. A. Heller *et al.*, Science **311**, 508 (2006).

[95] M. Lee, S. Ho Kim, and Hong Seok-Cheol, Proc. Natl. Acad. Sci. **107**, 4985 (2010).

[96] M. E. Fisher, J. Stat. Phys. **34**, 385 (1983).

[97] O. Gothoh, Adv. Biophys. **16**, 1 (1983).

[98] C. Itzykson, R. B. Pearson, and J. B. Zuber, Nuclear Phys. **B 220**, 415 (1983).

[99] J. D. Murray, *Mathematical Biology: An Introduction* 3rd edn (Springer, New York, 2002).

[100] W. van Saarloos, Phys. Rev. **A 37**, 211 (1988).

[101] S. M. Bhattacharjee, Europhys. Lett. **65**, 574 (2004).

[102] J. Lee *et al.*, J. Phys. Chem. **B 114**, 9872 (2010).

[103] S. M. Bhattacharjee, J. Phys. Condens. Matter **22**, 155102 (2010).

[104] J. Bechhoefer, H. Löwen, and L. S. Tuckerman, Phys. Rev. Lett. **67**, 10 (1991).

[105] J. Wereszczynski and I. Andricioaei, PNAS **103**(44), 16200 (2006).

[106] B. Luan and A. Aksimentiev, Phys. Rev. Lett. **101**, 118101 (2008).